Architecture of the BBSome and its role in ciliary protein trafficking

2018

Shohei Nozaki

TABLE OF CONTENTS

GENERAL INTRODUCTION

Cilia are organelles that project from the surfaces of various eukaryotic cells, and are supported by the axoneme, which is a microtubule-based scaffold. Cilia function as cellular antennae by mechanosensing extracellular stimuli, such as light and fluid flow, and chemosensing morphogenetic signals, such as Hedgehog (Hh) (Briscoe and Thérond, 2013; Mukhopadhyay and Rohatgi, 2014). Owing to their crucial roles, defects in cilia lead to a variety of congenital disorders, such as Bardet-Biedl syndrome (BBS), Joubert syndrome, nephronophthisis, Meckel syndrome, and short-rib thoracic dystrophy. These disorders are collectively referred to as the ciliopathies, which accompany a wide spectrum of clinical manifestations, including retinal degeneration, polycystic kidney, morbid obesity, and skeletal and brain malformations (Braun and Hildebrandt, 2017; Madhivanan and Aguilar, 2014). Although the ciliary membrane is continuous with the plasma membrane, the protein and lipid composition of the ciliary membrane differs greatly from that of the plasma membrane, due to the presence of the transition zone (TZ), which serves as a permeability/diffusion barrier at the base of cilia (Verhey and Yang, 2016; Wei *et al.*, 2015).

In addition to structural components of the axonemal microtubules, such as the αβ-tubulin dimer, various soluble and membrane proteins, including G protein–coupled receptors (GPCRs), are specifically present within cilia and on the ciliary membrane. Therefore, ciliary assembly and the maintenance of ciliary functions strictly rely on the proper trafficking of these proteins, which is mediated by the intraflagellar transport (IFT) machinery, often referred to as IFT trains or IFT particles (Ishikawa and Marshall, 2011; Rosenbaum and Witman, 2002; Sung and Leroux, 2013). The IFT machinery contains the IFT-A and IFT-B complexes. It has been believed that the IFT-B complex mediates anterograde protein trafficking from the ciliary base to the tip powered by kinesin-2 motor proteins, whereas the IFT-A complex mediates retrograde trafficking with the aid of the dynein-2 complex (Ishikawa and Marshall, 2011; Nakayama and Katoh, 2018; Sung and Leroux, 2013; Taschner and Lorentzen, 2016). In addition to the IFT-A and IFT-B complexes, the BBSome complex moves along the axonemal microtubules in association with IFT particles (Lechtreck *et al.*, 2009; Williams *et al.*, 2014) and has been implicated in the trafficking of ciliary membrane proteins (Fig. 0-1). In addition to the BBSome subunits, the Arf-like small GTPase ARL6/BBS3 was proposed to regulate the membrane recruitment and assembly of the BBSome via an interaction with the BBS1 subunit (Jin *et al.*, 2010; Liew *et al.*, 2014; Zhang *et al.*, 2011).

The BBSome and the IFT-A and IFT-B complexes are composed of eight, six, and 16 subunits, respectively (Fig. 0-2). Loss-of-function analyses of these subunits in *Chlamydomonas reinhardtii* and other ciliated organisms have revealed the role of each complex in the ciliary protein trafficking. However, the molecular mechanism in which the three complexes cooperate to regulate the trafficking of ciliary proteins is poorly understood, due to lack of information on interactions between and in the complexes. The interaction analysis has been left behind because of the number and size of the subunits of these complexes.

In the present study, I focused on the BBSome and aimed to reveal the architecture of the BBSome, the mode of its interaction with the IFT machinery, and its role in the trafficking of ciliary proteins. I first participated in development of a novel protein–protein interaction assay, named the visible immunoprecipitation (VIP) assay, in which not only binary, but also one-to-many and many-to-may protein interactions can be visually detected. By utilizing the VIP assay, I revealed the overall architecture of the BBSome. In addition, I showed that the BBSome is required for the export of GPCRs from cilia (Chapter 1). Next, I investigated the interaction between the BBSome and the IFT machinery, and found that the BBS1–BBS9 dimer interacts with the IFT38 subunit of the IFT-B complex. Furthermore, I demonstrated that this interaction is required for the BBSome-mediated export of GPCRs from cilia (Chapter 2).

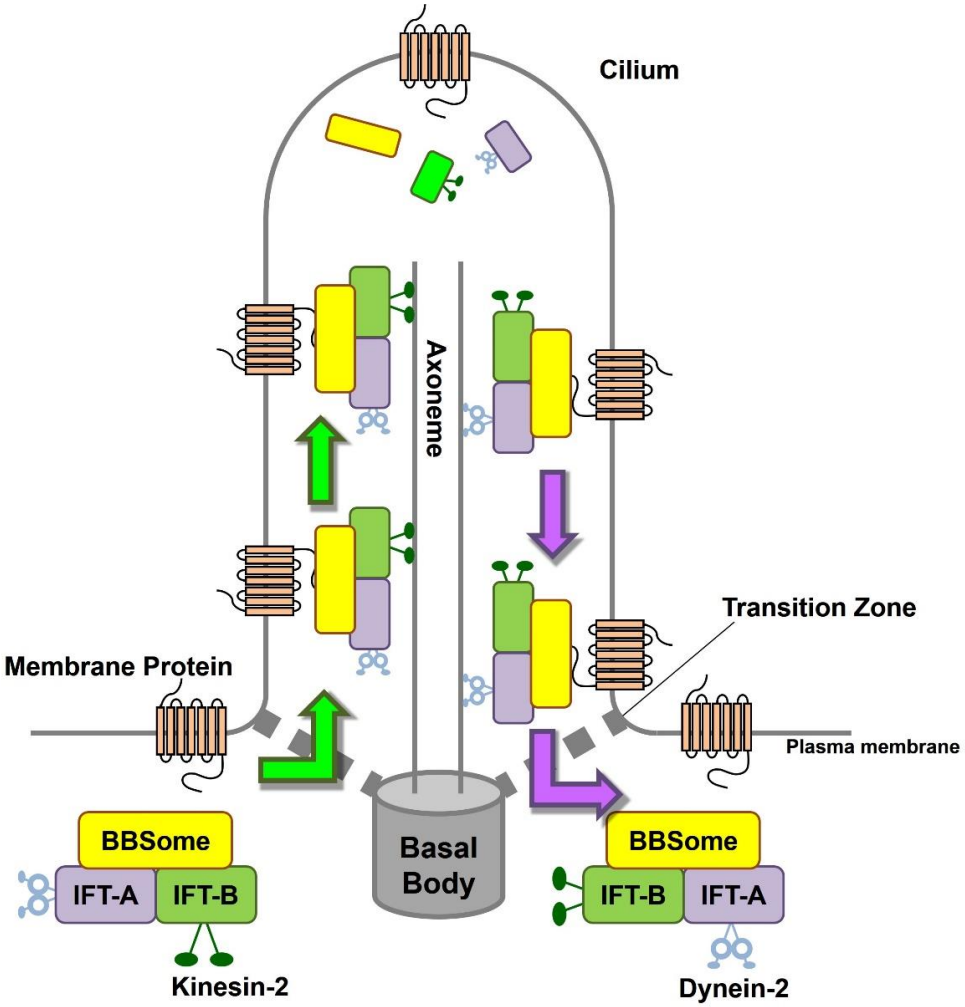

Fig. 0-1. Schematic illustration of ciliary protein trafficking mediated by the IFT machinery and the BBSome

Cilia are the microtubule-based structures projecting from the surface of most eukaryotic cells. Bidirectional trafficking of ciliary proteins along the axonemal microtubules is mediated by IFT particles, which contain the IFT-A and IFT-B complexes. The IFT particles are assembled around the basal body, enter the cilium across the TZ, and undergo processive anterograde trafficking along the axoneme powered by kinesin-2. At the ciliary tip, the IFT particles are thought to once disassemble to release cargo proteins. The IFT particles are then reassembled and cargos are loaded, and the assembled particles undergo retrograde trafficking powered by dynein-2. The particles exit the cilium across the TZ. The BBSome undergoes movement along the axoneme in association with the IFT particles, and is thought to regulate the trafficking of ciliary membrane proteins by connecting cargo proteins and the IFT particles, although there is no evidence of the physical interaction between the IFT particles and the BBSome.

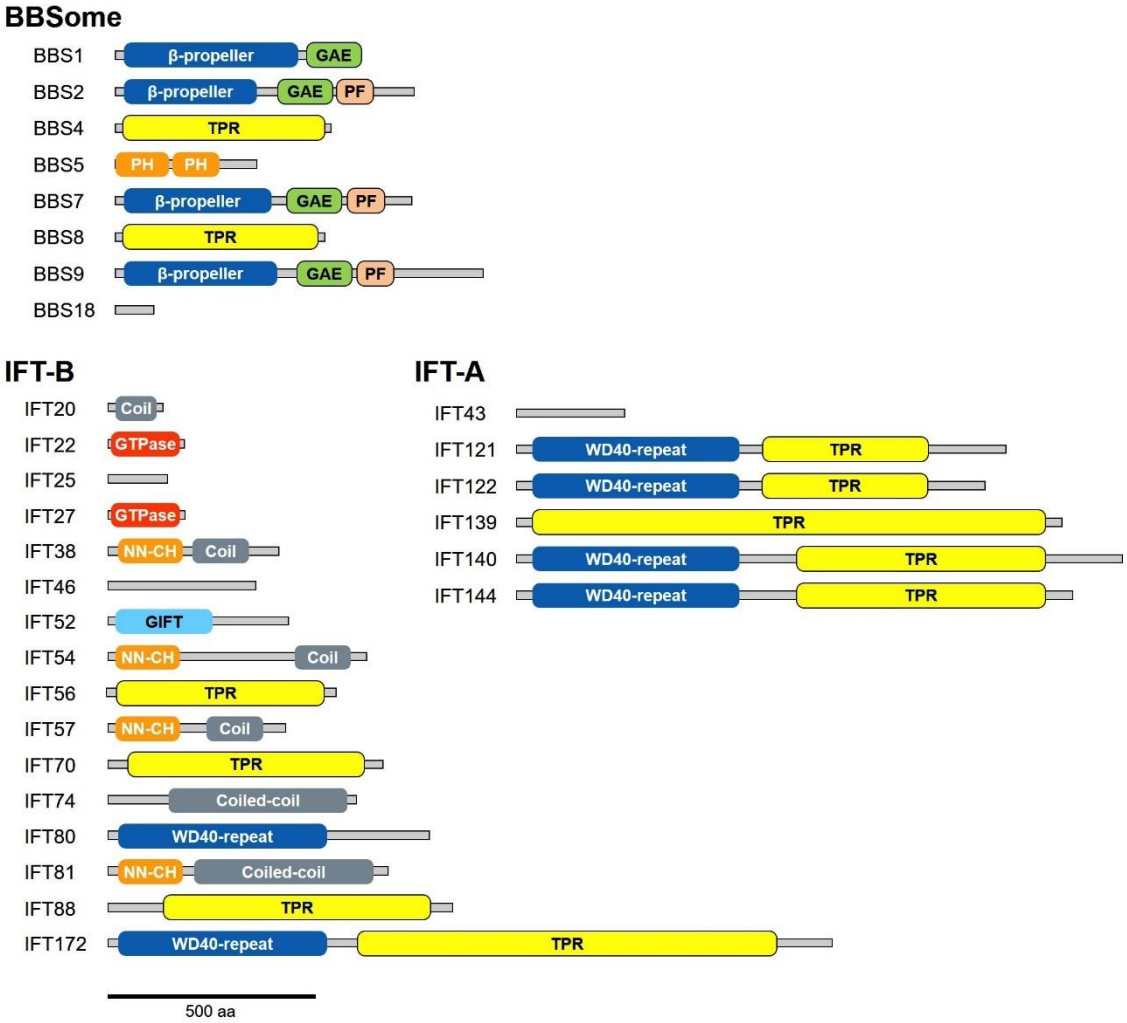

Fig. 0-2. Schematic representation of the domain organizations of all subunits of the BBSome, IFT-A, and IFT-B complexes

BBSome, IFT-A, and IFT-B are multisubunit complexes composed of eight, six, and 16 subunits, respectively. β-propeller, β-propeller (BP) fold; GAE, γ-adaptin ear-homology-like domain; PF, α/β-platform domain; PH, Pleckstrin homology domain; Coil, coiled-coil (CC) region; GTPase, GTPase domain; NN-CH, divergent calponin homology domain; GIFT, GldG/IFT domain; TPR, tetratricopeptide repeat domain. Scale bar, 500 amino acid residues.

ABBREVIATIONS

Ac-α-Tubulin	acetylated α-tubulin
ANOVA	analysis of variance
AP-1	adaptor protein complex 1
Arf	ADP ribosylation factor
ARL	Arf-like
BBS	Bardet-Biedl syndrome
BP	β-propeller
Cas	CRISPR-associated protein
CC	coiled-coil
cDNA	complementary DNA
COP	coat protein complex
CRISPR	clustered regularly interspaced short palindromic repeat
CT	C-terminal
DNA	deoxyribonucleic acid
DTT	dithiothreitol
E. Coli	Escherichia coli
EDTA	ethylenediaminetetraacetic acid
EGFP	enhanced green fluorescent protein
FBS	fetal bovine serum
FOP	FGFR1 oncogene partner
GAE	γ-adaptin ear-homology-like
GFP	green fluorescent protein
GGA	Golgi-localized, gamma adaptin ear-containing, Arf-binding
GIFT	GldG/IFT
GPCR	G protein–coupled receptor
GST	glutathione S-transferase
GTP	guanosine triphosphate
HEK	human embryonic kidney
HEPES	4-(2-hydroxyethyl)-1-piperazineethanesulfonic acid
Hh	Hedgehog
hTERT	human telomerase reverse transcriptase
IFT	intraflagellar transport
IPTG	Isopropyl β-D-1-thiogalactopyranoside
iRFP	infrared RFP

KO	knockout
LZTFL1	leucine zipper transcription factor like 1
mChe	mCherry
Nb	Nanobody
Neo	neomycin
NN-CH	divergent calponin homology domain
PAM	proto-spacer adaptor motif
PCR	polymerase chain reaction
PH	Pleckstrin homology
PF	α/β-platform
RFP	red fluorescent protein
RNA	ribonucleic acid
RPE	retinal pigment epithelial
SAG	Smoothened Agonist
SD	standard deviation
SDS-PAGE	sodium dodecyl sulfate-polyacrylamide gel electrophoresis
sgRNA	single guide RNA
SMO	Smoothened
SSTR	somatostatin receptor
tBFP	TagBFP
TPR	tetratricopeptide repeat
tRFP	TagRFP
TULP	Tubby-like protein
TZ	transition zone
VIP	visible immunoprecipitation
WT	wild type

Chapter 1: Analysis of the BBSome function on the basis of its architecture

ABSTRACT

Protein trafficking within cilia is mediated by the IFT machinery composed of large protein complexes. The BBSome consists of eight subunits encoded by causative genes of BBS, and has been implicated in the trafficking of ciliary GPCRs by connecting the IFT machinery to cargo GPCRs. Membrane recruitment of the BBSome to promote cargo trafficking has been proposed to be regulated by the Arf-like small GTPase ARL6/BBS3, through its interaction with the BBS1 subunit of the BBSome. To gain insights into the trafficking of ciliary membrane proteins by the BBSome, I first investigated how the BBSome assembles and interacts with ARL6. As a first step to reveal the role of the BBSome, I applied the "visible" immunoprecipitation (VIP) assay, which we developed as a flexible strategy for protein–protein interactions. By applying the VIP assay, I determined the overall architecture of the BBSome and the interaction mode of the core subcomplex composed of BBS1, BBS2, BBS7, and BBS9. Moreover, I found that the ARL6–BBS1 interaction is reinforced by BBS9. I next established *BBS1*-KO cells to reveal the role of the BBSome. *BBS1*-KO cells showed defects in the ciliary entry of other BBSome subunits and ARL6, and in ciliary retrograde trafficking and the export of the GPCRs, Smoothened (SMO) and GPR161. The trafficking defect of these GPCRs was rescued by the exogenous expression of wild-type BBS1, but not by its mutant lacking BBS9-binding ability. These data thus indicate that the intact BBSome is required for retrograde trafficking of GPCRs out of cilia.

INTRODUCTION

Cilia are specialized cell surface projections that function as cellular antennae by perceiving extracellular stimuli and by receiving and transducing developmental signals. Defects in ciliary assembly and functions cause the ciliopathies, including BBS, with a broad spectrum of symptoms. The composition of proteins and lipids in cilia are greatly different from those of the cell body, because the TZ at the base of cilia serve as a permeability/diffusion barrier. Therefore, there are specific soluble and membrane proteins inside cilia and on the ciliary membrane.

Protein trafficking to and/or within cilia is mediated by multisubunit complexes, including the BBSome, IFT-A, and IFT-B complexes. The IFT-B complex mediates anterograde protein trafficking with the aid of kinesin-2 motors, whereas the IFT-A complex mediates retrograde trafficking powered by the dynein-2 complex (Ishikawa and Marshall, 2011; Nakayama and Katoh, 2018; Rosenbaum and Witman, 2002; Sung and Leroux, 2013; Taschner and Lorentzen, 2016). The BBSome is composed of eight subunits (BBS1, BBS2, BBS4, BBS5, BBS7, BBS8, BBS9, and BBS18) and has been implicated in protein trafficking to and/or within the cilia (Jin and Nachury, 2009; Loktev *et al.*, 2008; Sung and Leroux, 2013). In addition to these BBSome subunits, the Arf-like small GTPase ARL6/BBS3 was proposed to regulate the membrane recruitment and coat-like assembly of the BBSome via an interaction with BBS1 (Jin *et al.*, 2010; Liew *et al.*, 2014; Zhang *et al.*, 2011). Another BBSome-interacting protein, LZTFL1/BBS17, was also proposed to regulate BBSome function (Eguether *et al.*, 2014; Seo *et al.*, 2010). All the BBSome subunits, ARL6/BBS3 and LZTFL1/BBS17 were identified by mutations of their respective genes in BBS patients.

Nachury and colleagues proposed that the BBSome functions similarly to coat protein complexes involved in membrane trafficking, on the basis of the following reasons (Jin *et al.*, 2010): (i) All the core subunits of the BBSome have structural domains that are found in the subunits of coat protein complexes, including COPI, COPII, and clathrin-adaptor complexes. These domains include the β-propeller (BP) fold, γ-adaptin ear-homology-like (GAE) domain, and α/β-platform (PF) domain; (ii) similarly to the membrane recruitment of COPI, COPII, and clathrin-adaptor coats that is triggered by Arf/Sar1 GTPases, the BBSome is recruited onto synthetic liposomes through an interaction between BBS1 and GTP-bound ARL6; and (iii) the ciliary targeting sequence of SSTR3, which is a GPCR found on the ciliary membrane, is directly recognized by the BBSome.

In order to obtain insights into the trafficking of ciliary membrane proteins by

the BBSome, our group attempted to map detailed interactions among BBSome subunits. However, the subunit interaction data obtained using the yeast two-hybrid system were unreliable, and BBS proteins expressed in *E. coli* were largely insoluble. By contrast, BBSome subunits expressed as fluorescent fusion proteins in HEK293T cells were soluble. Hence, I analyzed binary interactions between BBSome subunits expressed as fluorescent fusion proteins in HEK293T cells. During the course of these analyses, I sought to establish a novel, versatile assay to visualize protein–protein interactions based on coimmunoprecipitation, without requiring immunoblotting. Using this versatile assay system, which we named the VIP assay, I mapped the detailed interactions of the BBSome subunits. Furthermore, I investigated the roles of BBS1 in the BBSome complex by establishing *BBS1*-knockout (KO) cell lines, followed by rescue experiments using wild-type (WT) and mutant BBS1.

RESULTS

Unreliable BBSome subunit interaction data obtained using the yeast two-hybrid system

Our initial attempts to reveal interactions between BBSome subunits using GST pulldown assay were unsuccessful, because none of the examined BBSome subunits fused to GST were soluble in *E. coli*. Our next attempts using the yeast two-hybrid system also failed to obtain reliable interaction data: (i) an interaction between BBS8 and BBS9, which were reported to form a stoichiometric complex in a coimmunoprecipitation assay (Nachury *et al.*, 2007), was detected when they were expressed as fusion proteins with the Gal4 DNA-binding domain and activation domain, respectively, but not when the two proteins were expressed in a reverse bait–prey configuration; (ii) the interaction between BBS2 and BBS7, which were also reported to form a stoichiometric complex (Nachury *et al.*, 2007), was not detected in either of the bait–prey configurations; and (iii) BBS5 elicited self-activation when expressed as a fusion with the DNA-binding domain.

Outline of a novel method for visualizing protein–protein interactions

An outline of a novel method to determine protein–protein interactions without performing immunoblotting is summarized in Fig. 1-1. Expression vectors for two proteins (protein X and protein Y) fused to EGFP and tagRFP (tRFP), respectively, were transfected into cultured cells (usually HEK293T cells). Expression of these fusion proteins can be confirmed in living cells by observing the transfectants under a fluorescence microscope (Fig. 1-2A). At this step and/or the following immunoprecipitation step with anti-GFP Nanobody (Nb) (see Fig. 1-2B), considerable variability in the expression levels of fluorescent fusion proteins can be reproducibly observed. In such cases, changing the promoter of the expression vector to a stronger one (e.g., the CAG promoter) often improves the protein expression level. However, in my experience, the expression level of one protein sometimes varies when coexpressed protein is different.

Lysates prepared from the transfected cells were then processed for immunoprecipitation. As an alternative to conventional anti-GFP antibodies, I exploited anti-GFP Nb, which is a GFP-binding protein derived from a llama single–heavy chain antibody, and whose primary and three-dimensional structures are open (Kubala *et al.*, 2010; Saerens *et al.*, 2005); I expressed and purified anti-GFP Nb fused to GST in *E. coli* (see Materials and Methods). Cell lysates containing EGFP- and tRFP-fusion

proteins were pulled down with GST–anti-GFP Nb pre-bound to glutathione–Sepharose 4B beads. Instead of performing SDS–PAGE and subsequent immunoblotting (Fig. 1-1C), I directly observed beads bearing immunoprecipitates under a fluorescence microscope (Fig. 1-1A; for example, see Fig. 1-2B) or a confocal laser-scanning microscope (for example, see Fig. 1-4). If protein X interacts with protein Y, not only the EGFP signal but also the tRFP signal is detectable on the surface/perimeter of the beads. On the other hand, if protein X does not interact with protein Y, only the EGFP signal is detected. The relative intensities of the interactions can be roughly estimated by quantitating the fluorescence signals in the acquired bead images (Fig. 1-2C) or by subjecting the beads to measurement of fluorescence intensities with a microplate reader (Fig. 1-1B; Fig. 1-2D).

Application of the VIP assay to determine binary interactions of BBSome subunits

I first verified the effectiveness and reproducibility of the VIP assay by examining interactions of BBS9 with other BBSome subunits. An earlier study characterizing the BBSome suggested that BBS9 is the central organizing subunit of the BBSome (Nachury *et al.*, 2007). Expression vectors for BBS9 N-terminally tagged with tRFP and each of the eight BBSome subunits N-terminally tagged with EGFP were cotransfected into HEK293T cells. After protein expression was confirmed in living cells by fluorescence microscopy (Fig. 1-2A), lysates prepared from the transfected cells were subjected to immunoprecipitation using GST–anti-GFP Nb pre-bound to glutathione–Sepharose beads. Images of beads bearing immunoprecipitates were then acquired using the same microscope and exposure times. As shown in Fig. 1-2B, tRFP-BBS9 signal on the precipitated beads was detectable at varying intensities when tRFP–BBS9 was coexpressed with EGFP-tagged BBS1, BBS2, BBS5, and BBS8. The rank order of the intensities of the BBS9 interactions, roughly determined by quantitation of red signal intensities of the acquired images, was BBS2 > BBS8 > BBS1 ≥ BBS5 (Fig. 1-2C). When beads bearing immunoprecipitates were subjected to direct measurement of the fluorescence intensities with a microplate reader, a parallel rank order was obtained (Fig. 1-2D).

I then confirmed the tRFP-BBS9 interactions with other BBSome subunits tagged with EGFP by coimmunoprecipitation followed by conventional immunoblotting. As shown in Fig. 1-2E, the tRFP-BBS9 band was detected when lysates of cells coexpressing EGFP-BBS1, -BBS2, -BBS5, or -BBS8 were subjected to immunoprecipitation with GST–anti-GFP Nb (top panel). Although relative expression levels (Fig. 1-2E, bottom panel) and amounts in the precipitates (second panel) of the

EGFP-BBS proteins varied from protein to protein, the rank order of the relative band intensities (Fig. 1-2F) was roughly parallel with that determined by the VIP assay (Fig. 1-2C and D). Together, these results support the idea that the VIP assay is a convenient, reproducible, and qualitative/semi-quantitative alternative to conventional coimmunoprecipitation followed by immunoblotting. Because the most important point is that this assay is handy and convenient, I did not further investigate whether there is a linear relationship between the strength of the interactions (the affinity of the proteins) and the fluorescence intensity of the precipitated beads. More quantitative methods, such as surface plasmon resonance and/or isothermal titration calorimetry, will be needed to measure precise affinity, stoichiometry, and kinetics of the interactions between bait and prey proteins.

To obtain insight into the detailed architecture of the BBSome, I examined 8 × 8 = 64 possible combinations of BBSome subunits using the VIP assay (Fig. 1-3A and B). In contrast to the results obtained using the yeast two-hybrid system, all of the detectable binary interactions between EGFP- and tRFP-tagged BBSome subunits were also detected using reverse combinations of the fluorescent protein tags (Fig. 1-3B). Except for a weak interaction between EGFP-BBS7 and tRFP-BBS7, none of the BBSome subunits exhibited a homophilic interaction. Because the expression levels of fluorescent fusion proteins sometimes vary depending on coexpressed proteins, I routinely qualify binary interactions as “positive” when red fluorescent signals are visible on the perimeter of precipitated beads in reciprocal combinations of bait and prey fusion proteins under fixed conditions (see Materials and Methods, and the legend for Fig. 1-2B). Therefore, interactions that are not qualified as positive do not always mean that the two proteins do not interact with each other.

A model of the BBSome architecture predicted from the interaction data is schematically shown in Fig. 1-3C. The following features are evident: (i) BBS9 is the hub subunit of the BBSome, as suggested by the initial BBSome study (Nachury *et al.*, 2007); (ii) the core subcomplex consists of BBS1, BBS2, BBS7, and BBS9, all of which share some structural features with subunits of the clathrin adaptor complexes and the COPI coat complex (Jin *et al.*, 2010); (iii) BBS18 and BBS8 serve as connectors between BBS4 and BBS9; and (iv) BBS5, which has a phosphoinositide-binding PH domain (Nachury *et al.*, 2007), is located at the periphery of the core subcomplex.

Application of VIP assay to determine ternary and quaternary interactions of BBSome subunits

One notable feature of the BBSome model delineated above is that BBS18 is a

component of the BBSome that serves as a linker between BBS4 and BBS8, both of which are almost entirely composed of tetratricopeptide repeats. BBS18, which was originally referred to as BBIP10 (for BBSome-interacting protein of 10 kDa), was missed in the initial BBSome isolation (Nachury *et al.*, 2007) and was later found to be mutated in BBS patients (Scheidecker *et al.*, 2014); it was identified as a component of the BBSome in a subsequent study (Loktev *et al.*, 2008). However, the same study reported that BBIP10/BBS18 associates with the BBSome inside the cilium, but not at centriolar satellites (Loktev *et al.*, 2008).

To confirm that BBS18 is an integral component of the BBSome, I then applied the VIP assay to predicted ternary interactions of BBS4, BBS18, and BBS8. To this end, I coexpressed these proteins as EGFP, tagBFP (tBFP), and tRFP fusions in HEK293T cells, and subjected the cell lysates to precipitation with GST–anti-GFP Nb. As shown in Fig. 1-4A, tRFP-BBS8 was coprecipitated with EGFP-BBS4 when tBFP-BBS18 was coexpressed (upper panels). In striking contrast, tRFP-BBS8 was not precipitated at all when coexpressed with tBFP in place of tBFP-BBS18 (lower panels). Thus, these results unequivocally show that BBS18 is essential for connecting BBS4 and BBS8.

I then applied the VIP assay to the quaternary interactions of BBSome subunits in order to delineate the BBSome architecture. To this end, each of four BBSome subunits was fused to EGFP, tBFP, infrared-RFP (iRFP), or tRFP/mCherry (mChe). I first examined the predicted linear interactions of BBS4, BBS18, BBS8, and BBS9. As shown in Fig. 1-4B, mChe-BBS9 was coprecipitated with EGFP-BBS4 in the presence of coexpressed tBFP-BBS18 and iRFP-BBS8 (top panels). In marked contrast, mChe-BBS9 was not coprecipitated at all in the absence of either tBFP-BBS18 (second row panels) or iRFP-BBS8 (third row panels), or both (bottom panels). Thus, these results confirm the linear interactions, BBS4–BBS18–BBS8–BBS9, predicted from the binary interaction data.

I next examined the predicted circular interactions of BBS9, BBS2, BBS7, and BBS1. As shown in Fig. 1-4C, tRFP-BBS1 coprecipitated with EGFP-BBS2 in the presence of coexpressed tBFP-BBS7 and iRFP-BBS9 (top panels). Unlike the case of the linear interactions shown in Fig. 1-4B, tRFP-BBS1 was coprecipitated with EGFP-BBS2 in the absence of either iRFP-BBS9 (second row panels) or tBFP-BBS7 (third row panels). However, tRFP-BBS1 was not coprecipitated in the absence of both iRFP-BBS9 and tBFP-BBS7 (bottom panels). These results confirm the predicted circular interactions: BBS1 can interact indirectly with BBS2 in two ways, namely, through BBS7 and BBS9.

Thus, the VIP assay is a powerful tool, not only for revealing binary protein–

protein interactions but also for determining the order/hierarchy of those interactions. The assays using three or four distinct fluorescent fusion proteins can thereby be referred to as visible “three-hybrid” or “four-hybrid” assays, respectively.

Modes of interactions involving BBSome core subunits and ARL6

As shown in Figs. 1-3 and 1-4C, I found that the BBSome core subcomplex is assembled by the circular interactions involving BBS1, BBS2, BBS7, and BBS9. These four core subunits share common domain organizations reminiscent of those of coat protein complexes (Jin *et al.*, 2010). All four subunits are predicted to have a BP fold in their N-terminal half (Fig. 1-5A); for BBS1 and BBS9, their seven-bladed BP structures were confirmed by X-ray crystallography (Knockenhauer and Schwartz, 2015; Mourão *et al.*, 2014). In their C-terminal half, these four subunits are predicted to have a GAE domain, which is followed by a PF domain (except for BBS1). Because BP folds are found in subunits of the COPI coat protein complex, which are subunits responsible for cargo recognition (Ma and Goldberg, 2013; Jackson *et al.*, 2012), and because GAE domains are found in clathrin adaptor proteins, the AP-1 γ-subunit, and GGA proteins (Nakayama and Wakatsuki, 2003), Nachury and colleagues proposed that the BBSome functions like a coat protein complex (Jin *et al.*, 2010).

To delineate the interaction modes among the core subunits, I divided the wild-type BBS1, BBS2, BBS7, and BBS9 proteins into their N-terminal BP domain and their C-terminal (CT) region containing the GAE and PF domains (schematically shown in Fig. 1-5A) coexpressed them as EGFP- and tRFP/mChe-fusions in HEK293T cells, and subjected them to the VIP assay. As shown in Fig. 1-5B, the BBS9 CT region fused to EGFP interacted with the tRFP-fused CT regions of BBS1 and BBS2 (row 3 and 6, respectively). On the other hand, the BP domain of BBS9 interacted with BBS5 and BBS8 (Fig. 1-5B, row 7 and 8, respectively). The BBS2–BBS7 interaction was mediated by their CT regions (Fig. 1-5C, bottom row).

The VIP assay suggested that the BP domain of BBS1 interacted mainly with the BBS7 CT region (Fig. 1-5D, bottom row), although the BBS1 BP domain also exhibited an interaction with the BBS7 BP region (row 3). I also performed conventional immunoblotting analysis to confirm the VIP data, because a recent study using the yeast two-hybrid system did not detect the BBS1–BBS7 interaction (Woodsmith *et al.*, 2017). As shown in Fig. 1-5E, the CT region of BBS7 made a major contribution to its interaction with the BBS1 BP domain (lane 11), although the BBS7 BP region also exhibited an interaction with the BBS1 BP domain (lane 8).

I confirmed that ARL6ΔN15(Q73L) interacted only with BBS1 (Fig. 1-5F) as

previously reported (Jin *et al.*, 2010). In agreement with a previous crystallographic study (Mourão *et al.*, 2014), ARL6ΔN15(Q73L) was coprecipitated with the BP domain, but not the CT region, of BBS1 (Fig. 1-5G); I here used an ARL6ΔN15 (residues 1–15 deleted) construct, like in previous studies (Jin *et al.*, 2010; Mourão *et al.*, 2014), as the presence of an N-terminal amphipathic helix generally hampers interactions of the ARF/ARL family GTPases with their effectors, at least in vitro.

Based on the data shown in Fig. 1-5, B–G, I predicted the interaction model shown in Fig. 1-5H. The BBS7–BBS2, BBS2–BBS9, and BBS9–BBS1 interactions are mediated by their CT regions, whereas the interaction between BBS1 and BBS7 is mediated mainly by their BP domain and CT region, respectively. The BBS1 BP domain also participates in its interaction with ARL6.

The CT region of BBS1 contains an α-helix region followed by a GAE domain. A BBS1 construct lacking the α-helix region (Δα; Fig. 1-6A) retained the ability to interact with BBS9 (Fig. 1-6B, column 2). By contrast, another BBS1 construct lacking the C-terminal 18-amino acids of the GAE domain (BBS1(1–575); Fig. 1-6A) did not interact with BBS9 (Fig. 1-6B, column 3). Thus, at least a part of the GAE domain of BBS1 participates in its interaction with BBS9.

Lorentzen and colleagues previously reported the crystal structure of *Chlamydomonas* ARL6ΔN15 in complex with *Chlamydomonas* BBS1(1–425) (Mourão *et al.*, 2014). They constructed some mutants of the human BBS1 BP domain on the basis of the crystal structure and found that an I399E or R404A mutation in human BBS1 abolished its interaction with ARL6; Ile399 and Arg404 are located within the bipartite blade 1 of the BBS1 BP domain (Mourão *et al.*, 2014). By the VIP assay and conventional immunoblotting analysis, I confirmed their data; the I399E or R404A mutant of BBS1 could not interact with ARL6ΔN15(Q73L) (Fig. 1-6, C and D, lanes 3 and 4). Somewhat unexpectedly, BBS1(1-575) demonstrated an attenuated interaction with ARL6ΔN15(Q73L) compared with BBS1(WT) (Fig. 1-6, C and D, compare lane 5 with lane 2); this will be discussed later (see below). By contrast, both BBS1 point mutants retained their ability to interact with BBS7 (Fig. 1-6, E and F, lanes 2 and 3). Thus, it is likely that the BBS1 BP domain interacts with ARL6 and BBS7, at least in part via distinct interfaces.

Impaired retrograde trafficking of ciliary GPCRs in *BBS1*-KO cells

SMO and GPR161 are seven-pass transmembrane GPCRs involved in Hh signaling (Briscoe and Thérond, 2013; Mukhopadhyay and Rohatgi, 2014). Under basal conditions, SMO is absent from cilia, whereas GPR161 on the ciliary membrane

negatively regulates Hh signaling. When the Hh pathway is stimulated, for example, by treating ciliated cells with a small molecule activator, Smoothened Agonist (SAG), SMO enters cilia and GPR161 exit cilia; consequently, the negative regulation of the Hh signaling is canceled.

Sheffield and colleagues previously reported that, in cells derived from *Arl6*-KO mice, SMO is significantly accumulated within cilia even under basal conditions (Zhang *et al.*, 2011). On the other hand, Nachury and colleagues reported that GPR161 was retained in the cilia of *Arl6*-KO IMCD3 cells even when the cells were treated with SAG (Liew *et al.*, 2014). These observations taken together suggested that retrograde trafficking and/or export of these ciliary GPCRs are impaired in the absence of ARL6.

I here established *BBS1*-KO hTERT-RPE1 cell lines using a CRISPR/Cas9 system modified in our laboratory (the version 2 method; see Katoh *et al.*, 2017; briefly summarized in Fig. 1-7) and compared their phenotypes with those of control RPE1 cells, as ARL6 directly interacts with BBS1 and regulates BBSome function. Two *BBS1*-KO cell lines (#B1-1-23 and #B1-2-21) established using distinct target sequences were analyzed (see Materials and Methods and Fig. 1-8). Regarding localization of markers of the ciliary membrane (ARL13B) or the axoneme (acetylated α-tubulin; Ac-α-tubulin), no substantial differences were observed between control RPE1 cells and the *BBS1*-KO cell lines (Fig. 1-9, A–C, and A′–C′). In addition, the frequency of ciliogenesis (Fig. 1-9S) or ciliary length (Fig. 1-9T) was not significantly different between control RPE1 cells and the two *BBS1*-KO cell lines.

ARL6 (Fig. 1-9D), BBS5 (Fig. 1-9G), and BBS9 (Fig. 1-9J) were uniformly distributed within cilia in 10%–20% of control RPE1 cells (also see Fig. 1-10, U–W). In marked contrast, localization of these BBS proteins was substantially altered in the *BBS1*-KO cell lines: ARL6 was no longer found inside cilia, but its localization at the ciliary base was, at least partially, retained (Fig. 1-9, E and F; also see Fig. 1-9U); BBS5 localization within cilia and at the ciliary base was abolished (Fig. 1-9, H and I, also see Fig. 1-9V); ciliary localization of BBS9 was also abolished, and BBS9-positive aggregates were often observed around the base (Fig. 1-9, K and L, also see Fig. 1-9W). Although the identity of these aggregates is unclear, Sheffield and colleagues also reported the presence of BBS9-positive and BBS8-positive aggregates around the ciliary base in RPE1 cells treated with BBS1 siRNA (Seo *et al.*, 2011). Overall, it is thus likely that the BBSome and ARL6 cannot enter cilia in the absence of BBS1.

As the BBSome is believed to move within cilia in association with IFT particles containing the IFT-A and IFT-B complexes (Williams *et al.*, 2014), I also

analyzed the localization of IFT-A and IFT-B subunits in the *BBS1*-KO cell lines. However, the localization of IFT88 (an IFT-B subunit) or IFT140 (an IFT-A subunit) was not apparently altered in the absence of BBS1 compared with control RPE1 cells; IFT88 was mainly localized at the ciliary base with a minor proportion found along cilia (Fig. 1-9, M–O), whereas the majority of IFT140 is found at the base (Fig. 1-9, P–R). It is likely that intraciliary movement of the IFT-A or IFT-B complex is not dependent on the BBSome, although the BBSome moves in association with IFT particles.

I then compared the localization of SMO and GPR161 under basal (–SAG) and SAG-treated (+SAG) conditions. Under basal conditions, the ciliary localization of SMO was not detected in control RPE1 cells (Fig. 1-10A) but was substantially increased in the *BBS1*-KO cell lines (Fig. 1-10, B and C, also see Fig. 1-10M). Upon stimulation with SAG, SMO entered cilia in control RPE1 cells (Fig. 1-10D, also see Fig. 1-10M), and its ciliary localization was further enhanced in the *BBS1*-KO cells (Fig. 1-10, E and F, also see Fig. 1-10M). These observations suggest two possibilities: one is that the BBSome suppresses ciliary entry of SMO; and the other is that, even under basal conditions, SMO undergoes constitutive cycling between the ciliary and plasma membranes to keep its ciliary level low, and that a block in its retrograde trafficking and/or exit from cilia in the absence of BBS1 might result in significant retention of SMO on the ciliary membrane. In view of the GPR161 data (see below), I favor the latter possibility.

On the other hand, in control cells, GPR161 was found within most cilia under basal conditions (Fig. 1-10G), and its localization to cilia was significantly decreased under SAG-stimulated conditions (Fig. 1-10J). Under basal conditions, localization of GPR161 within cilia in the *BBS1*-KO cell lines (Fig. 1-10, H and I; also see Fig. 1-10N) was significantly higher than that in control cells (Fig. 1-10G). Furthermore, unlike in control cells, GPR161 was retained within cilia even when the *BBS1*-KO cells were treated with SAG (Fig. 1-10, K and L; also see Fig. 1-10N). The altered localization of SMO and GPR161 in the *BBS1*-KO cells under basal and SAG-stimulated conditions is reminiscent of a previous study in our group on cells lacking IFT139, which is a subunit of the IFT-A complex (Hirano *et al.*, 2017); in *IFT139*-KO cells, retrograde trafficking and/or export of ciliary GPCRs, including SMO and GPR161, was severely impaired. These observations together indicate that, in the absence of BBS1, retrograde trafficking and/or ciliary exit of the GPCRs involved in Hh signaling is impaired.

BBS1 mediates retrograde trafficking of GPCRs in the context of the BBSome via its interaction with BBS9

To exclude the potential off-target effects of the CRISPR/Cas9 system, I then performed rescue experiments. *BBS1*-KO cells were infected with a lentiviral vector for the stable expression of mChe-tagged BBS1(WT) or its mutant. In contrast to the *BBS1*-KO (#B1-1-23) cell line without exogenous BBS1 expression (Fig. 1-10, B, E, H, and K), SMO was excluded from and GPR161 was localized within cilia (Fig. 1-11, A and I; also see Fig. 1-11, Q and R) in the #B1-1-23 cell line expressing mChe-BBS1(WT) under basal conditions, as observed in control cells (Fig. 1-10, A and G). Upon stimulation with SAG, SMO entered and GPR161 exited cilia (Fig. 1-11, E and M; also see Fig. 1-11, Q and R) in the mChe-BBS1(WT)–expressing *BBS1*-KO cell line, similarly to in control cells (Fig. 1-10, D and J). Thus, the impaired localization of SMO and GPR161 in the *BBS1*-KO cell line under both basal and SAG-stimulated conditions was rescued by the exogenous expression of BBS1(WT).

In striking contrast, the exogenous expression of mChe-tagged BBS1(1-575), which cannot interact with BBS9, did not restore the normal localization of SMO or GPR161 in the *BBS1*-KO cell line; a substantial, although low, level of SMO was found within cilia under basal conditions (Fig. 1-11D; also see Fig. 1-11Q), and an increased level of GPR161 within cilia was found under basal conditions, and the level was maintained even when the KO cells were stimulated with SAG (Fig. 1-11P; also see Fig. 1-11R). These data indicate that the interaction of BBS1 with BBS9, in other words, the integrity of the BBSome core subcomplex, is essential for BBSome function to mediate retrograde trafficking of ciliary GPCRs and/or their exit from cilia.

ARL6 interacts with the BBSome via BBS1 with the aid of BBS9

In contrast to the failed recovery of GPCR retrograde trafficking by the expression of BBS1(1-575), in *BBS1*-KO cells exogenously expressing a BBS1 mutant defective in ARL6 binding substantially rescued the abnormal localization of SMO and GPR161. Namely, in the *BBS1*-KO cell line expressing mChe-BBS1(I399E) or mChe-BBS1(R404A), SMO was excluded from cilia under basal conditions (Fig. 1-11, B and C; also see Fig. 1-11Q). Ciliary exit of GPR161 upon SAG treatment was promoted in *BBS1*-KO cells expressing mChe-BBS1(I399E) or mChe-BBS1(R404A) (Fig. 1-11, N and O), compared with those expressing mChe-BBS1(1–575) (Fig. 1-11P; also see Fig. 1-11R). Thus, these BBS1 point mutants appeared to be functional, at least partly, with regard to GPCR trafficking, even though they are defective in ARL6 binding (Fig. 1-6, C and D). Given that ARL6 demonstrates a binary interaction only

with BBS1 among the BBSome subunits (Fig. 1-5F), the results of these rescue experiments were intriguing.

In an attempt to address the apparent contradiction of the data obtained by the rescue experiments of the *BBS1*-KO cells (Fig. 1-11) with the biochemical interaction data (Fig. 1-6, C and D), I took advantage of the VIP assay to analyze whether the ARL6–BBS1 interaction can be enhanced in the presence of other BBSome subunit(s). For this purpose, tRFP-fused ARL6ΔN15(Q73L) and either EGFP-fused BBS1(WT), BBS1(I399E), or BBS1(R404A) were coexpressed with tBFP fusions of all the other BBSome subunits, other core subunits (BBS2, BBS7, and BBS9), or linker subunits (BBS4, BBS8, and BBS18) in HEK293T cells. As shown in Fig. 1-12A, the interaction of EGFP-BBS1(WT) with tRFP-ARL6 appeared to be promoted in the presence of tBFP-fused all the other BBSome subunits (BBS2/4/5/7/8/9/18; Fig. 1-12A, column 1) or other core subunits (BBS2/7/9; column 4) compared with that in the presence of tBFP-fused linker subunits (BBS4/8/18) (column 7), the latter which does not demonstrate a direct interaction with BBS1. Importantly, substantial interaction of BBS1(I399E) or BBS1(R404A) with ARL6 was detectable in the presence of all other BBSome subunits or all other core subunits, but not in the presence of linker subunits (compare columns 1–6 with 7–9).

I then investigated which core subunit(s) can enhance the ARL6–BBS1 interaction. As shown in Fig. 1-12B, the interaction between EGFP-BBS1(WT) and tRFP-ARL6 was substantially enhanced in the presence of tBFP-BBS9 (column 7), but not in the presence of tBFP-BBS2 (column 1) or tBFP-BBS7 (column 4). Furthermore, tBFP-BBS9 made the interaction between tRFP-ARL6 and EGFP-BBS1(I399E) or EGFP-BBS1(R404A) (column 8 and 9) detectable. The VIP data were confirmed by conventional immunoblotting. tBFP-BBS9 substantially increased the amount of tRFP-ARL6 coimmunoprecipitated with EGFP-BBS1(WT), as compared with tBFP-BBS2 and tBFP-BBS7 (Fig. 1-12C, top panel; compare lane 7 with lanes 1 and 4). Furthermore, tBFP-BBS9 also led to an increase in the amount of tRFP-ARL6 coprecipitated with EGFP-BBS1(I399E) or EGFP-BBS1(R404A) (middle panel; compare lanes 8 and 9 with lanes 2 and 5, and lanes 3 and 6, respectively).

The data shown in Fig. 1-5B indicate that the BBS9 CT region interacts with the BBS1 CT region. I then examined whether the BBS9 CT region is sufficient for promoting the BBS1 interaction with ARL6. As shown in Fig. 1-12, D and E, not only the WT construct (lane 2) but also the CT region (lane 4) of BBS9 considerably enhanced the interaction of BBS1(WT) with ARL6. The enhancement of the BBS1–ARL6 interaction by BBS9 was confirmed to be mediated by the interaction of BBS9

with BBS1, since the BBS9 CT region did not promote the interaction of BBS1(1-575) with ARL6 (compare lane 6 with lane 4).

These VIP and immunoblotting data suggest that BBS9 can reinforce the interaction of ARL6 with BBS1, although it does not directly interact with ARL6 (see Discussion). Furthermore, these data can explain why BBS1(I399E) and BBS1(R404A) can rescue, at least partially, the *BBS1*-KO phenotype (Fig. 1-11), although neither of the BBS1 mutants forms a binary interaction with ARL6 (Fig. 1-6, C and D; and Fig. 1-12, B and C, lanes 2 and 3, and lanes 4 and 5) (see Discussion).

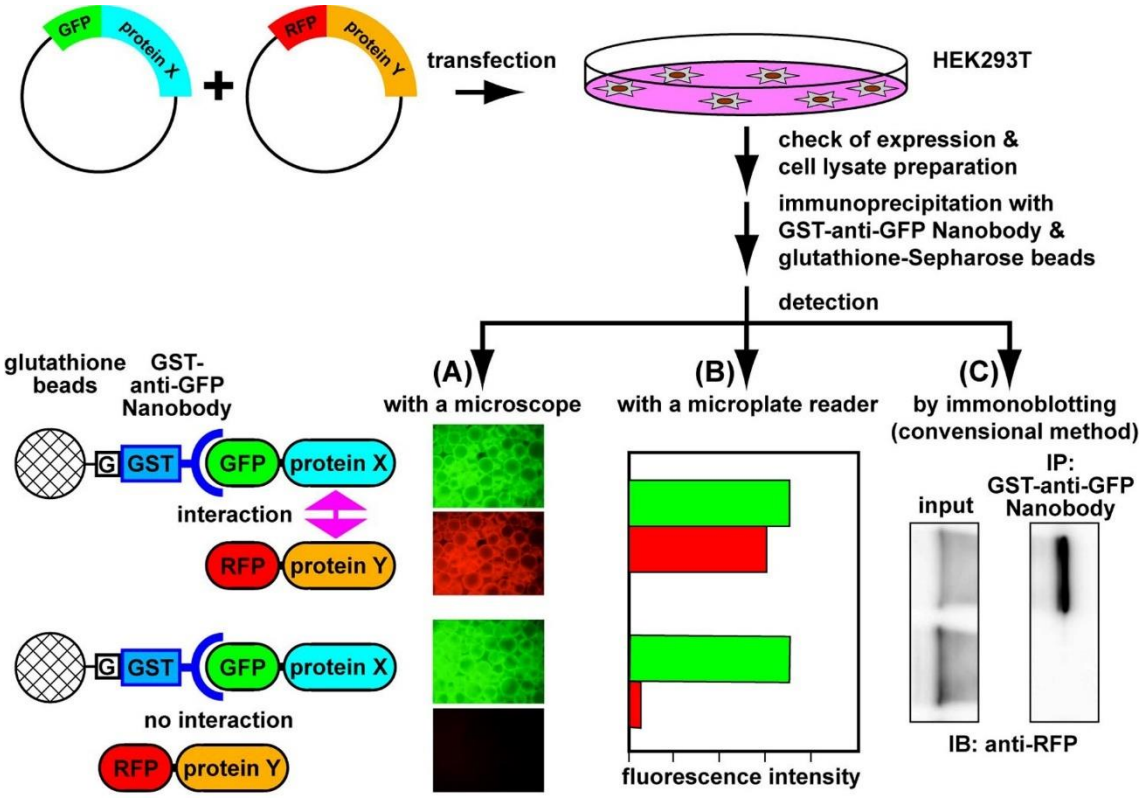

Fig. 1-1. Outline of the "visible" immunoprecipitation assay

HEK293T cells were transfected with expression vectors for proteins X and Y, fused to GFP and RFP, respectively. After expression of the fluorescent fusion proteins was confirmed under a fluorescence microscope, cell lysates were prepared and processed for immunoprecipitation with GST–anti-GFP Nb pre-bound to glutathione–Sepharose 4B beads. (A) Beads bearing immunoprecipitates were directly observed with a fluorescent microscope. If protein X interacted with protein Y, both the green and red signals were detected on the surface/perimeter of the beads. If protein X did not interact with protein Y, only the green signal was detected. (B) Beads bearing immunoprecipitates were placed in a 96-well plate, and the fluorescence intensity in each well was measured using a fluorescence microplate reader. (C) Proteins bound to the precipitated beads were processed for conventional immunoblotting: SDS-PAGE, electroblotting onto a membrane, and detection with anti-RFP antibody

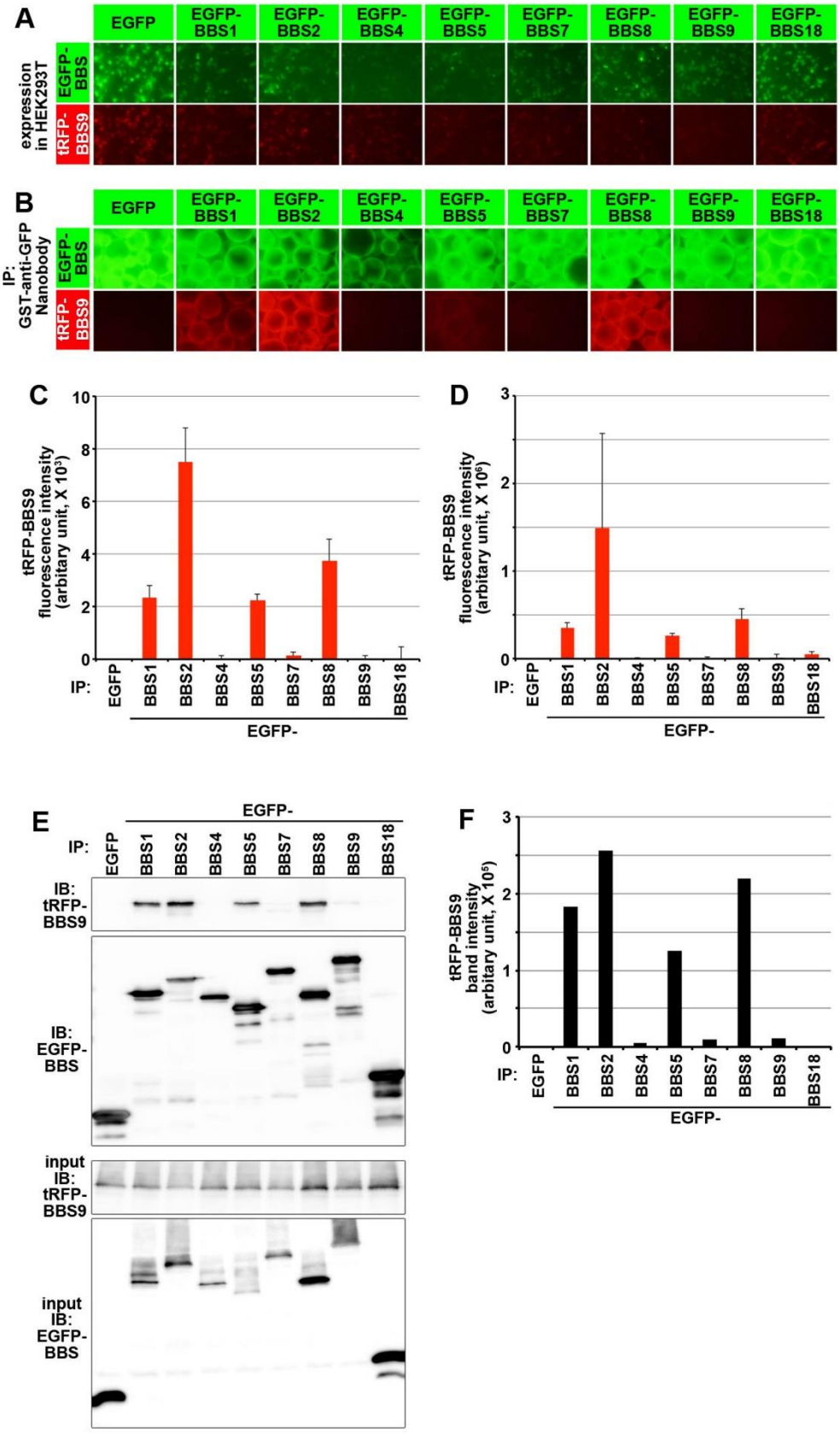
A
EGFP
EGFP-BBS1
EGFP-BBS2
EGFP-BBS4
EGFP-BBS5
EGFP-BBS7
EGFP-BBS8
EGFP-BBS9
EGFP-BBS18
expression in HEK293T
EGFP-BBS
tRFP-BBS9
B
IP: GST-anti-GFP Nanobody
C
tRFP-BBS9 fluorescence intensity (arbitary unit, X 10³)
IP:
EGFP-
D
tRFP-BBS9 fluorescence intensity (arbitary unit, X 10⁶)
E
IB: tRFP-BBS9
IB: EGFP-BBS
input IB: tRFP-BBS9
input IB: EGFP-BBS
F
tRFP-BBS9 band intensity (arbitary unit, X 10⁵)

Fig. 1-2. Interactions of BBS9 with other BBSome subunits revealed by the VIP assay

HEK293T cells cultured in 6-well plates were transfected with expression vectors for tRFP-BBS9 and either EGFP or each BBSome subunit fused to EGFP, as indicated. (A) 24 h after transfection, expression of the green and red fluorescent fusion proteins was confirmed using a BZ-8000 all-in-one–type fluorescence microscope. Lysates prepared from the transfected cells were precipitated with GST–anti-GFP Nb pre-bound to glutathione–Sepharose 4B beads. (B) Beads bearing immunoprecipitates were observed, and the beads images were acquired, using a BZ-8000 microscope under fixed conditions (for green fluorescence, sensitivity ISO 400, exposure 1/30 sec; and for red fluorescence, sensitivity ISO 800, exposure 1/10 sec). (C) Red fluorescence intensities in the acquired images were measured using ImageJ and expressed as bar graphs. From each value, the value of fluorescence intensity obtained from cells expressing EGFP and tRFP-BBS9 was subtracted as background. (D) Fluorescence intensities on the precipitate beads were measured directly, using a microplate reader. The values were expressed as bar graphs as in (C). In (C) and (D), the values are means ± SD of three independent experiments. (E) Proteins bound to the precipitated beads (upper two panels) or input proteins (10%; lower two panels) were processed for immunoblotting with antibodies to tRFP (top and third panels) or GFP (second and bottom panels). (F) The band intensities in the top panel in (E) were quantitated using ImageJ and expressed as bar graphs.

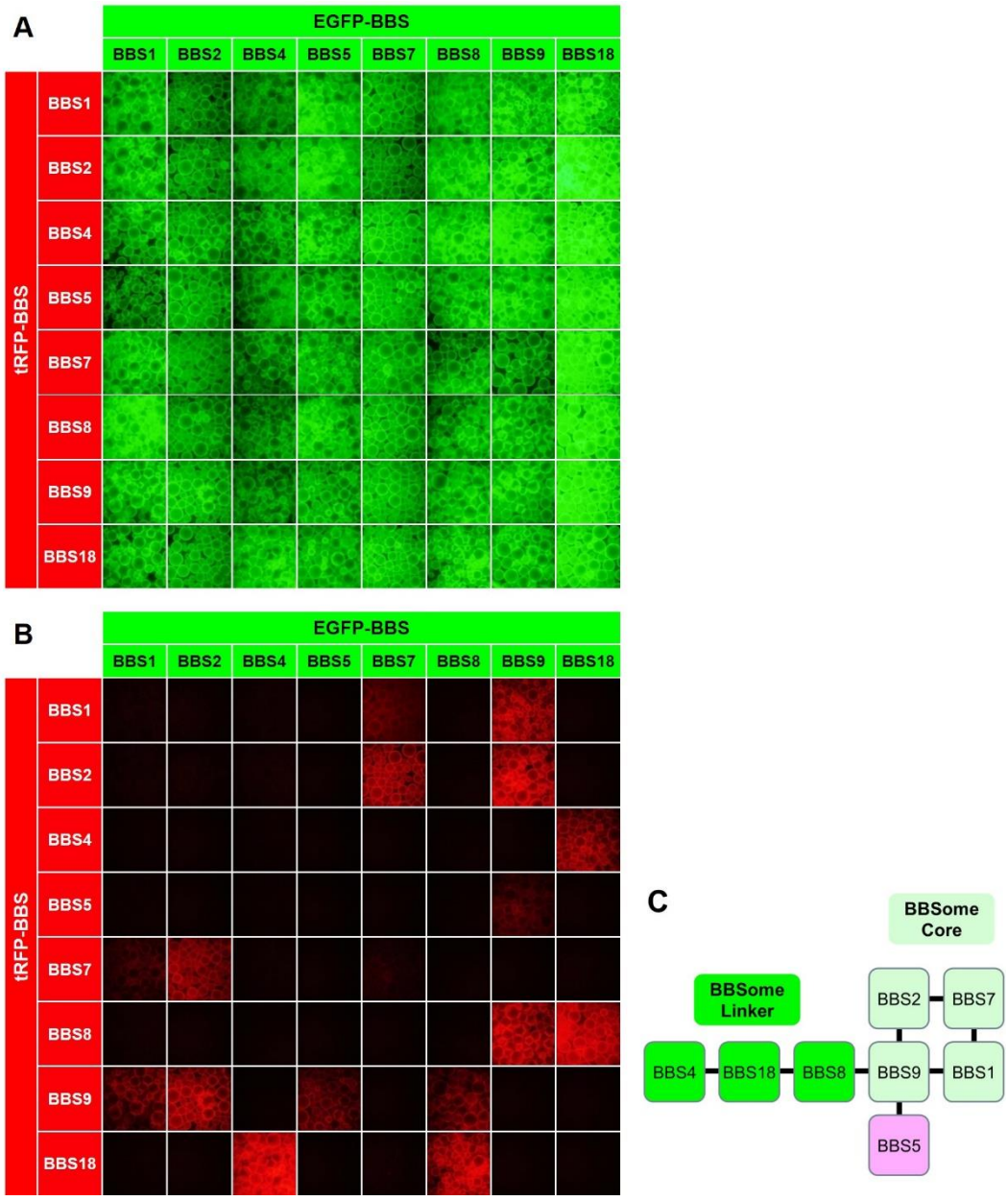

Fig. 1-3. All-by-all VIP assays of BBSome subunits

HEK293T cells cultured in 6-well plates were transfected with expression vectors for tRFP- and EGFP-fused BBSome subunits, as indicated. After expression of the green and red fluorescent fusion proteins was confirmed, lysates were prepared from the transfected cells and precipitated with GST–anti-GFP Nb pre-bound to glutathione–Sepharose beads. The green (A) and red (B) fluorescence signals on the precipitated beads were observed, and the bead images were acquired, using a BZ-8000 microscope. The experiments were repeated twice, and essentially the same results were obtained. (C) The BBSome subunit interaction map predicted from the data shown in (B). The linker subunits and the core subunits are shown in green and light green, respectively.

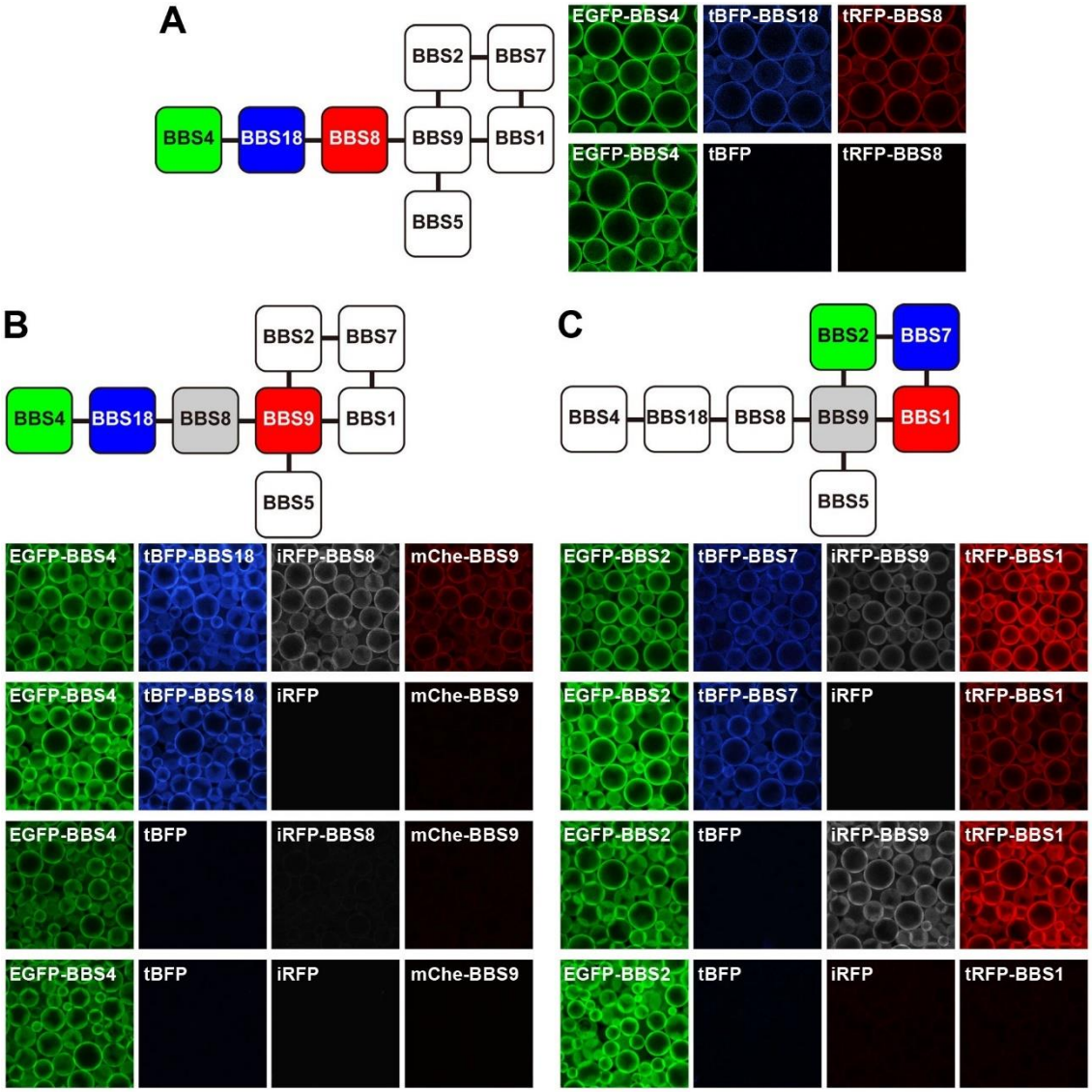
A
BBS4
BBS18
BBS8
BBS2
BBS7
BBS9
BBS1
BBS5
EGFP-BBS4
tBFP-BBS18
tRFP-BBS8
EGFP-BBS4
tBFP
tRFP-BBS8
B
BBS4
BBS18
BBS8
BBS2
BBS7
BBS9
BBS1
BBS5
EGFP-BBS4
tBFP-BBS18
iRFP-BBS8
mChe-BBS9
EGFP-BBS4
tBFP-BBS18
iRFP
mChe-BBS9
EGFP-BBS4
tBFP
iRFP-BBS8
mChe-BBS9
EGFP-BBS4
tBFP
iRFP
mChe-BBS9
C
BBS4
BBS18
BBS8
BBS2
BBS7
BBS9
BBS1
BBS5
EGFP-BBS2
tBFP-BBS7
iRFP-BBS9
tRFP-BBS1
EGFP-BBS2
tBFP-BBS7
iRFP
tRFP-BBS1
EGFP-BBS2
tBFP
iRFP-BBS9
tRFP-BBS1
EGFP-BBS2
tBFP
iRFP
tRFP-BBS1

Fig. 1-4. Visible three- and four-hybrid assays of BBSome subunits

(A) HEK293T cells grown on 6-cm dishes were transfected with expression vectors for EGFP-BBS4, tRFP-BBS8, and either tBFP-BBS18 (upper panels) or tBFP (lower panels). After expression of the green and red fluorescent fusion proteins was confirmed, lysates were prepared from the transfected cells and precipitated with GST–anti-GFP Nb pre-bound to glutathione–Sepharose beads. The green (left), blue (middle), and red (right) fluorescence signals on the precipitated beads were observed, and the bead images were acquired using an A1R-MP confocal laser-scanning microscope (Nikon). (B) HEK293T cells grown in 6-cm dishes were transfected with expression vectors for EGFP-BBS4, mChe-BBS9, either tBFP-BBS18 or tBFP, and either iRFP-BBS8 or iRFP, as indicated, and then processed as described in (A). The signals for EGFP (left panels), tBFP (second column panels), iRFP (third column panels), and mChe (right panels) on the precipitated beads were acquired using a confocal microscope. (C) HEK293T cells grown in 6-cm dishes were transfected with expression vectors for EGFP-BBS2, tRFP-BBS1, either tBFP-BBS7 or tBFP, and either iRFP-BBS9 or iRFP, as indicated, and then processed as described in (A). The signals for EGFP (left), tBFP (second column), iRFP (third column), and tRFP (right) on the precipitated beads were acquired using a confocal microscope. These experiments were repeated twice, and essentially the same results were obtained.

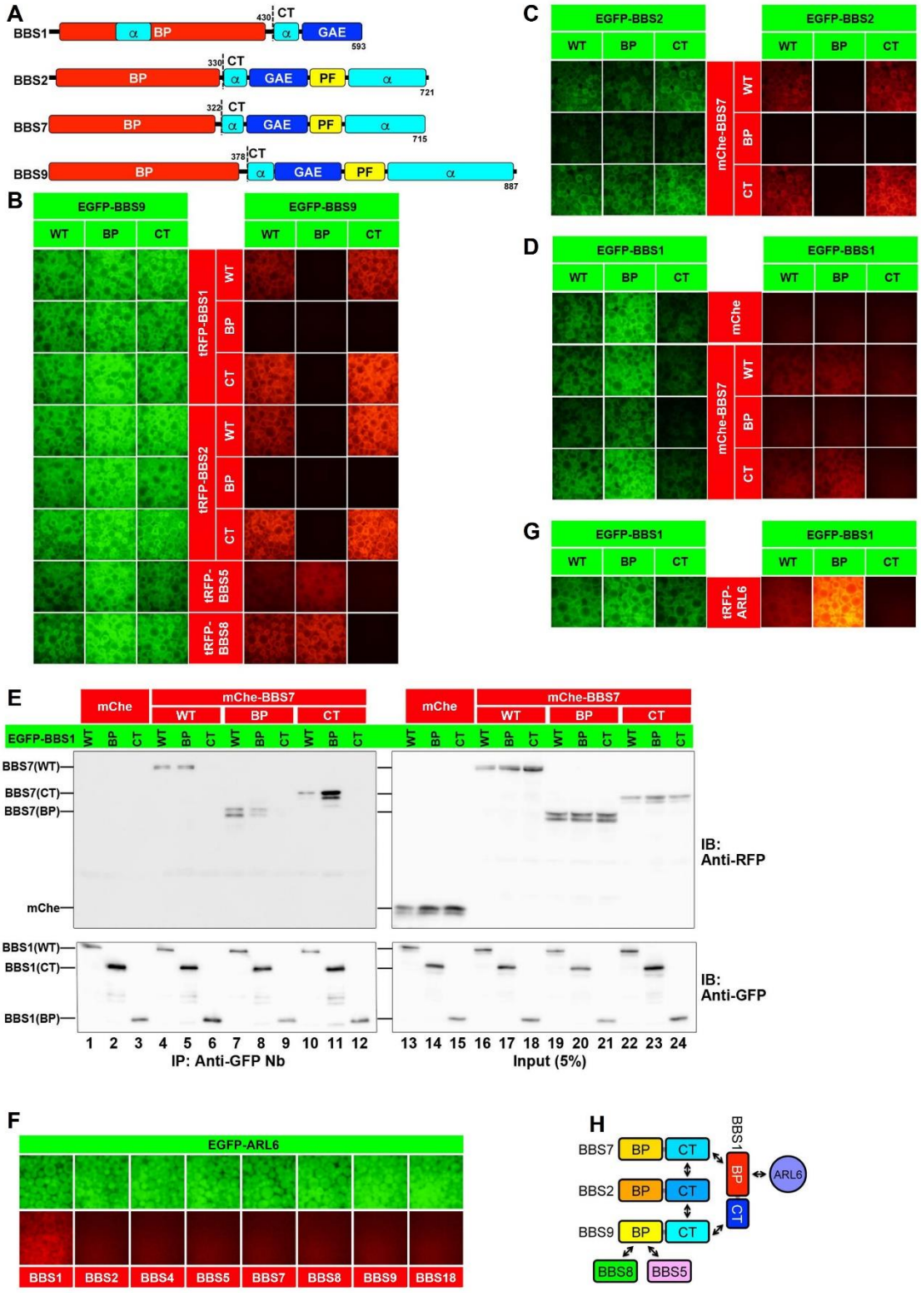
A
BBS1
BBS2
BBS7
BBS9
BP
GAE
PF
CT
B
EGFP-BBS9
WT
BP
CT
tRFP-BBS1
tRFP-BBS2
tRFP-BBS5
tRFP-BBS8
C
EGFP-BBS2
mChe-BBS7
D
EGFP-BBS1
mChe
G
tRFP-ARL6
E
mChe
mChe-BBS7
EGFP-BBS1
BBS7(WT)
BBS7(CT)
BBS7(BP)
mChe
BBS1(WT)
BBS1(CT)
BBS1(BP)
IB: Anti-RFP
IB: Anti-GFP
IP: Anti-GFP Nb
Input (5%)
F
EGFP-ARL6
BBS1
BBS2
BBS4
BBS5
BBS7
BBS8
BBS9
BBS18
H
ARL6

Fig. 1-5. Modes of interaction involving BBSome core subunits and ARL6

(A) Schematic representation of the domain organizations of human BBS1, BBS2, BBS7, and BBS9. The amino acid positions of the boundary between the BP and CT constructs are also indicated. (B) HEK293T cells were cotransfected with expression vectors for a BBS9 construct fused to EGFP and a BBS1, BBS2, BBS5, or BBS8 construct fused to tRFP, as indicated. Lysates prepared from the transfected cells were subjected to the VIP assay. (C) Lysates were prepared from HEK293T cells coexpressing an EGFP-fused BBS2 construct and mChe-fused BBS7 construct, as indicated, and subjected to the VIP assay. (D, E) HEK293T cells were cotransfected with expression vectors for an EGFP-fused BBS1 construct and mChe or an mChe-fused BBS7 construct, as indicated. Lysates were prepared from the transfected cells and processed for the VIP assay (D) or SDS-PAGE followed by immunoblotting analysis with an anti-RFP antibody, which reacts with mChe, or an anti-GFP antibody (E). (F) Lysates prepared from HEK293T cells coexpressing EGFP-ARL6ΔN15(Q73L) and each of the BBSome subunits fused to mChe were subjected to the VIP assay. (G) Lysates prepared from HEK293T cells coexpressing an EGFP-fused BBS1 construct, as indicated, and tRFP-fused ARL6ΔN15(Q73L), were processed for the VIP assay. (H) Schematic representation of the predicted model of interactions involving BBSome subunits and ARL6.

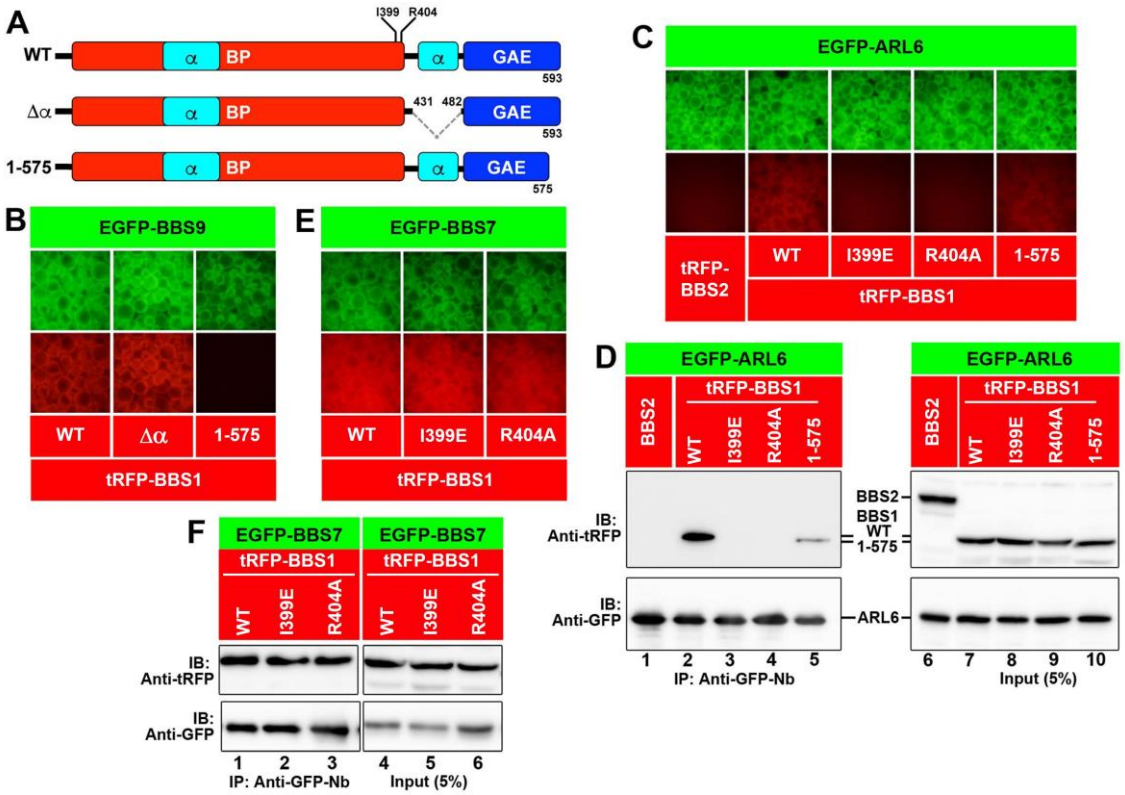

Fig. 1-6. Interaction modes of BBS1 with BBS9, BBS7, and ARL6

(A) Schematic representation of BBS1 constructs used in the experiments. (B) Lysates prepared from HEK293T cells coexpressing the EGFP-BBS9 construct and mChe-fused BBS1 construct, as indicated, were subjected to the VIP assay. (C, D) HEK293T cells were cotransfected with expression vectors for EGFP-fused ARL6ΔN15(Q73L) and a tRFP-fused BBS1 construct, as indicated. Lysates were prepared from the transfected cells and processed for the VIP assay (C) or SDS-PAGE followed by immunoblotting analysis with an anti-tRFP or anti-GFP antibody (D). (E, F) Lysates prepared from HEK293T cells cotransfected with expression vectors for EGFP-BBS7 and a tRFP-fused BBS1 construct as indicated were processed for the VIP assay (E) or SDS-PAGE followed by immunoblotting analysis with an anti-tRFP or anti-GFP antibody (F).

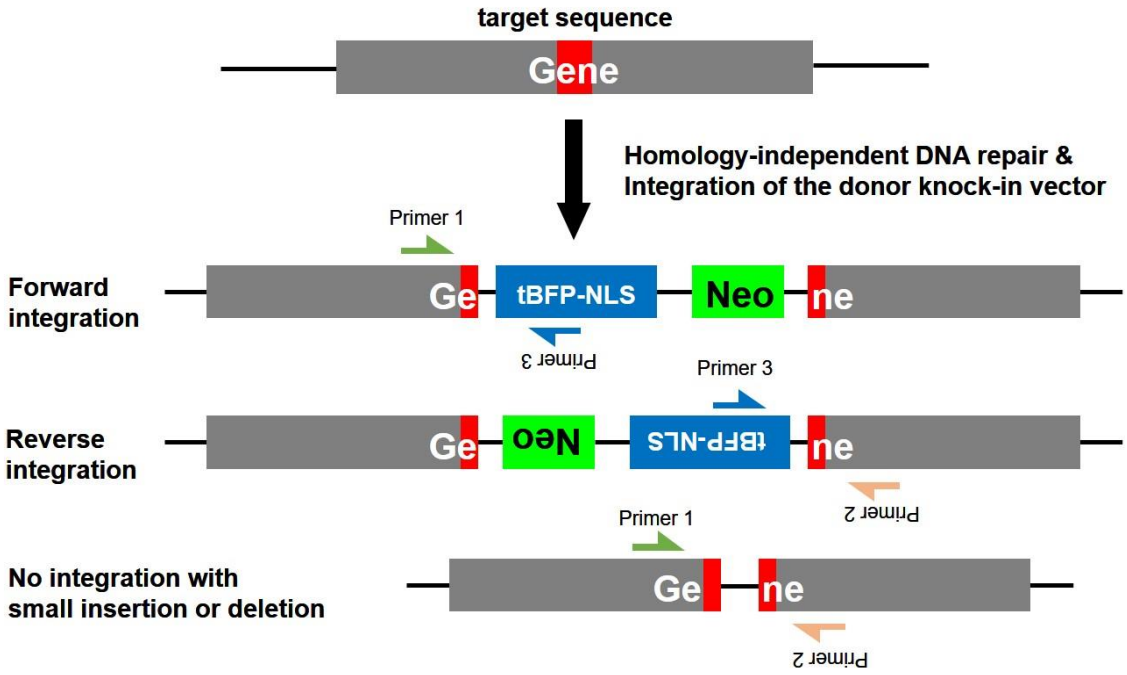

Fig. 1-7. Strategy for the establishment of KO cell lines and confirmation of knock-in donor vector integration or a small insertion or deletion in the genome
Schematic outline of the establishment of KO cell lines. Upon homology-independent DNA repair of the target sequence after Cas9-mediated double-strand beak, two types of integration of the donor knock-in vector containing tBFP-3×NLS (blue) and Neo (green) can occur; forward integration and reverse integration. In other cases, the target gene often undergoes error-prone repair with small insertions or deletions, causing a frameshift. Half-headed arrows indicate primers used for genomic PCR, with the same color representing identical primers. The target sequence is shown in red.

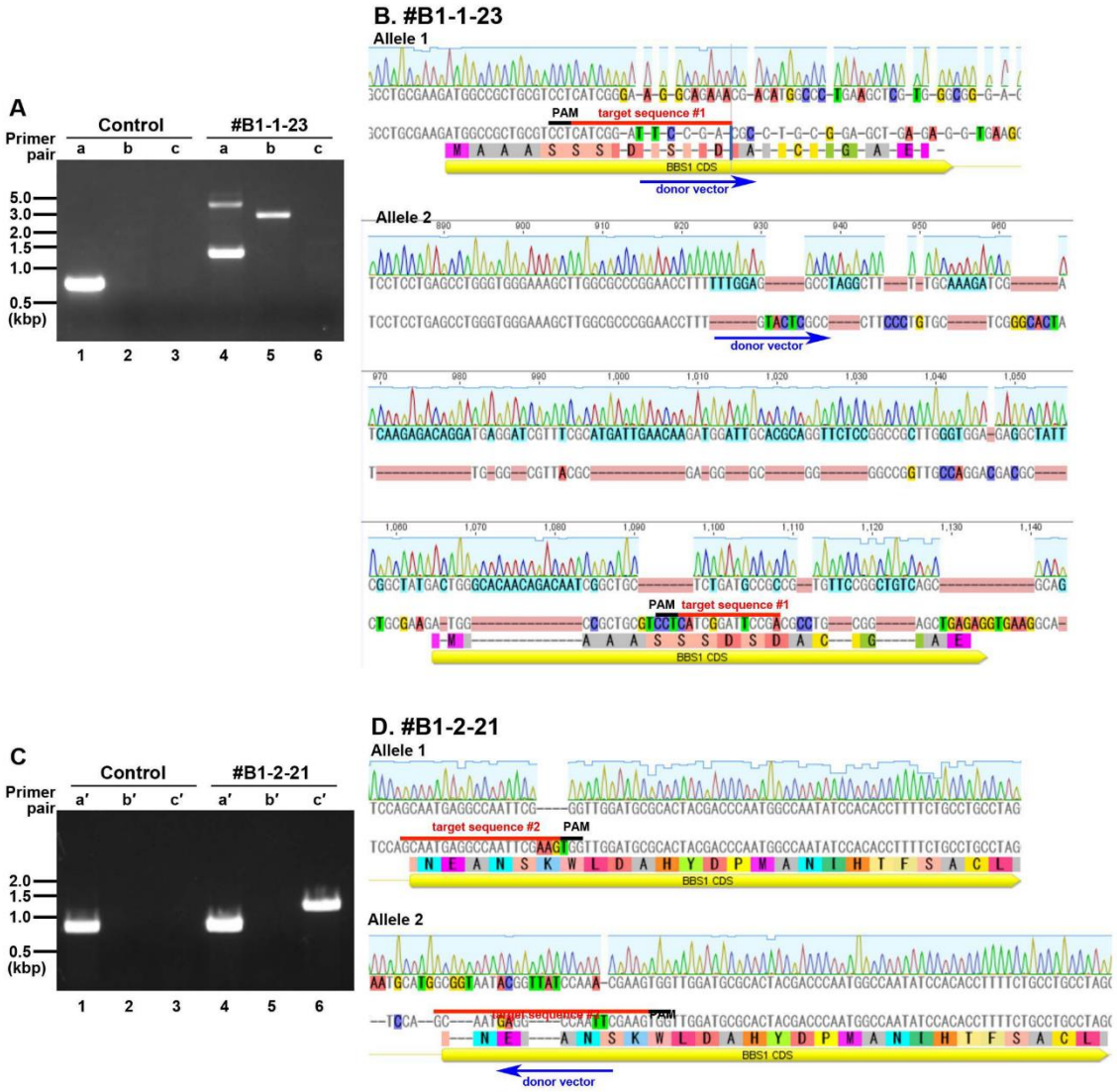

Fig. 1-8. Genomic PCR and sequence analyses of the *BBS1*-KO cell lines

(A and C) Genomic DNA was extracted from control hTERT-RPE1 cells and form the *BBS1*-KO cell lines, #B1-1-23 (A) and #B1-2-21 (C), established using donor knock-in vectors containing target sequences 1 and 2, respectively. The DNA was subjected to PCR using the primer sets as indicated (see Table 3) in an attempt to detect alleles with a small indel or no insertion (a and a′), or with forward (b and b′) or reverse (c and c′) integration of the donor knock-in vector. (B and D) Alignment of allele sequences of the B1-1-23 (B) and B1-2-21 (D) cell lines determined by direct sequencing of the genomic PCR products. Red and black lines indicate the target sequences and PAM sequence, respectively, and blue arrows indicate the direction of donor vector integration.

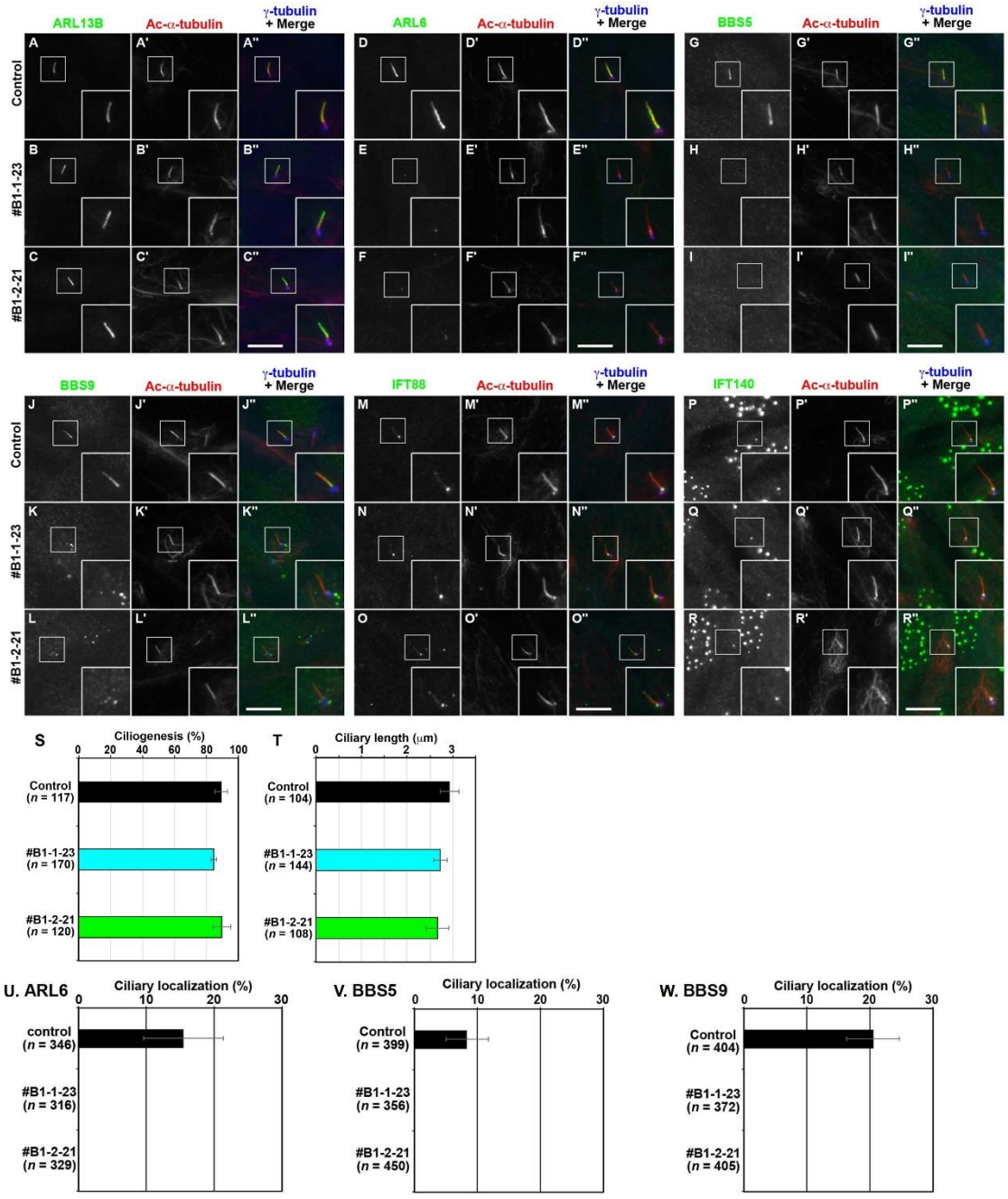
ARL13B
Ac-α-tubulin
γ-tubulin + Merge
ARL6
BBS5
BBS9
IFT88
IFT140
Control
#B1-1-23
#B1-2-21
S
Ciliogenesis (%)
Control (n = 117)
#B1-1-23 (n = 170)
#B1-2-21 (n = 120)
T
Ciliary length (μm)
Control (n = 104)
#B1-1-23 (n = 144)
#B1-2-21 (n = 108)
U. ARL6
Ciliary localization (%)
control (n = 346)
#B1-1-23 (n = 316)
#B1-2-21 (n = 329)
V. BBS5
Control (n = 399)
#B1-1-23 (n = 356)
#B1-2-21 (n = 450)
W. BBS9
Control (n = 404)
#B1-1-23 (n = 372)
#B1-2-21 (n = 405)

Fig. 1-9. The BBSome and ARL6 do not localize within cilia in *BBS1*-KO cells
(A–R) Control RPE1 cells (A, D, G, J, M, and P) or the *BBS1*-KO cell lines #B1-1-23 (B, E, H, K, N, and Q) or #B1-2-21 (C, F, I, L, O, and R) were serum-starved for 24 h and triple immunostained for ARL13B (A–C), ARL6 (D–F), BBS5 (G–I), BBS9 (J–L), IFT88 (M–O), or IFT140 (P–R), and Ac-α-tubulin (A′–R′) and γ-tubulin (A″–R″). Insets show enlarged images of the boxed regions. Scale bars, 10 μm. (S)–(T), percentages of Control cells and *BBS1*-KO cells with cilia (S) and the length of cilia (T) in the data shown in A–C, were measured and expressed as bar graphs. (U)–(W), Control cells and *BBS1*-KO cells with ciliary localization of ARL6 (U), BBS5 (V), and BBS9 (W) were counted, and the percentages are expressed as stacked bar graphs. Values are means ± SD of three independent experiments. In each set of experiments, 34–60 (S), 31–51 (T), 82–152 (U), 109–185 (V), and 95–175 (W) ciliated cells were analyzed and the total numbers of ciliated cells analyzed (*n*) are shown.

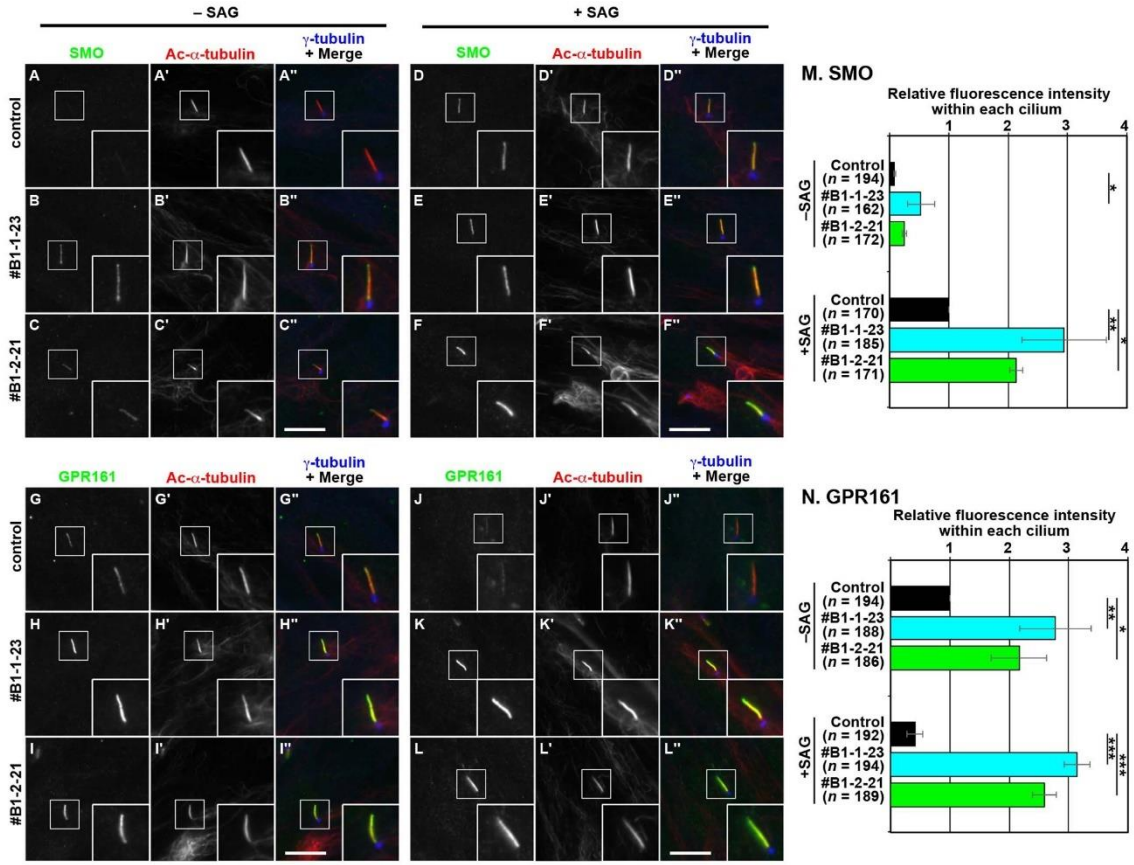

Fig. 1-10. Accumulation of GPR161 within cilia in *BBS1*-KO cells

(A–L) Control RPE1 cells (A, D, G, and J), and the *BBS1*-KO cell lines #B1-1-23 (B, E, H, and K) and#B1-2-21 (C, F, I, and L) were serum-starved for 24 h and further cultured for 24 h in the absence (–SAG) or presence (+SAG) of 200 nM SAG. The cells were triple immunostained for either SMO (A–F) or GPR161 (G–L), Ac-α-tubulin (A′–L′), and γ-tubulin (A″–L″). Scale bars, 10 μm. (M and N) Fluorescence staining intensities of SMO (M) and GPR161 (N) in control and *BBS1*-KO cells were measured, and relative intensities of the cells, with SAG-treated control cells normalized to 1, are expressed as bar graphs. Values are means ± SD of three independent experiments. In each set of experiments, 50–71 (M) and 50–69 (N) ciliated cells were analyzed and the total numbers of ciliated cells analyzed (*n*) are shown. *, $p < 0.05$; **, $p < 0.005$; ***, $p < 0.0001$ (one-way ANOVA followed by Tukey post-hoc analysis).

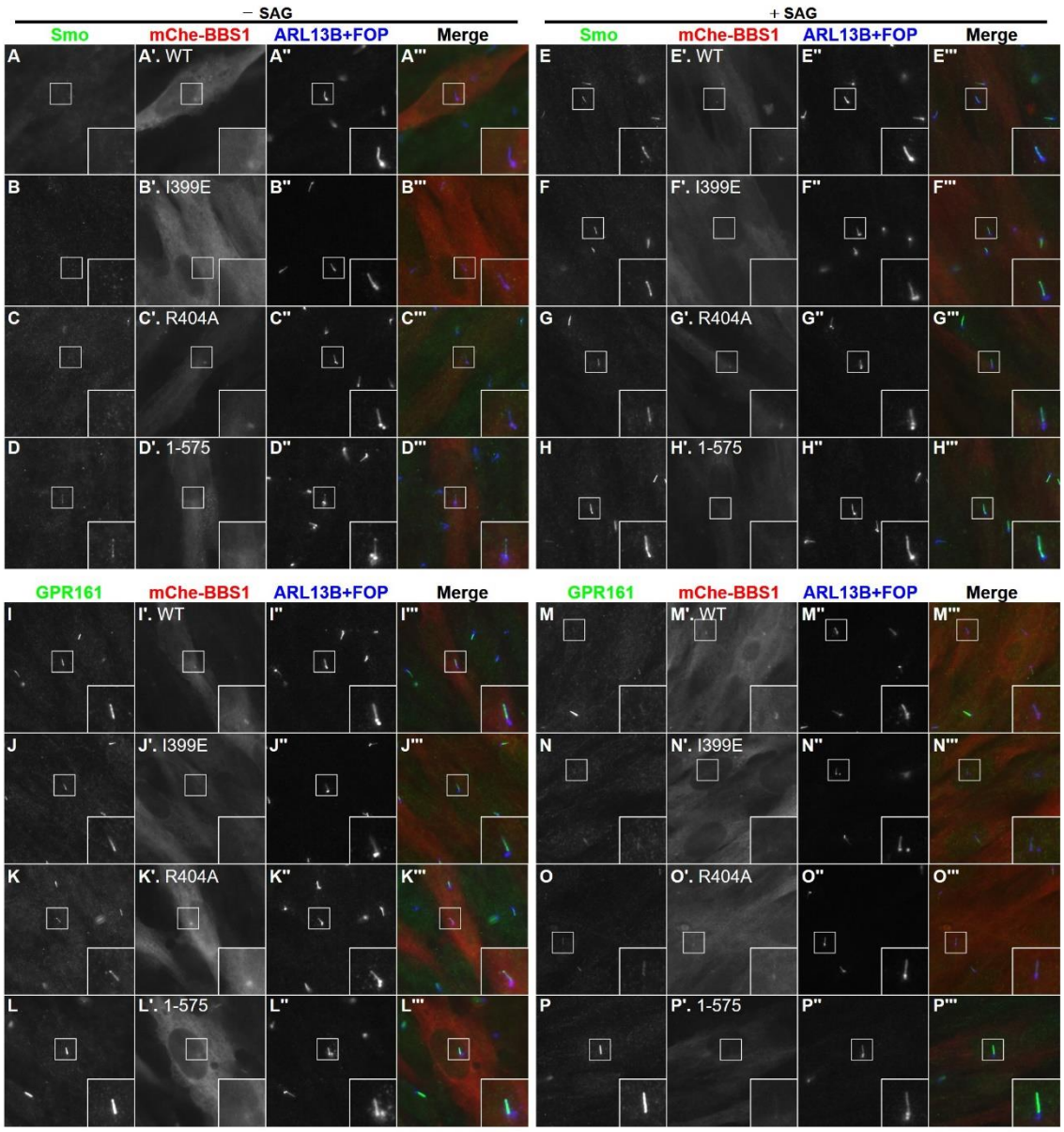
− SAG
+ SAG
Smo
mChe-BBS1
ARL13B+FOP
Merge
A
A'. WT
A''
A'''
B
B'. I399E
B''
B'''
C
C'. R404A
C''
C'''
D
D'. 1-575
D''
D'''
E
E'. WT
E''
E'''
F
F'. I399E
F''
F'''
G
G'. R404A
G''
G'''
H
H'. 1-575
H''
H'''
GPR161
I
I'. WT
I''
I'''
J
J'. I399E
J''
J'''
K
K'. R404A
K''
K'''
L
L'. 1-575
L''
L'''
M
M'. WT
M''
M'''
N
N'. I399E
N''
N'''
O
O'. R404A
O''
O'''
P
P'. 1-575
P''
P'''

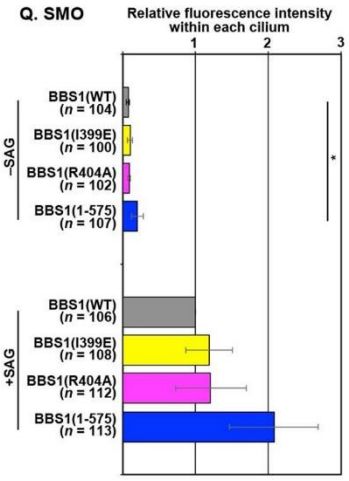
Q. SMO
Relative fluorescence intensity within each cilium
1
2
3
−SAG
BBS1(WT) (n = 104)
BBS1(I399E) (n = 100)
BBS1(R404A) (n = 102)
BBS1(1-575) (n = 107)
+SAG
BBS1(WT) (n = 106)
BBS1(I399E) (n = 108)
BBS1(R404A) (n = 112)
BBS1(1-575) (n = 113)
*

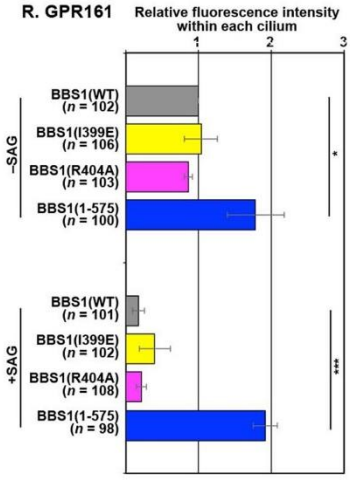
R. GPR161
Relative fluorescence intensity within each cilium
1
2
3
−SAG
BBS1(WT) (n = 102)
BBS1(I399E) (n = 106)
BBS1(R404A) (n = 103)
BBS1(1-575) (n = 100)
+SAG
BBS1(WT) (n = 101)
BBS1(I399E) (n = 102)
BBS1(R404A) (n = 108)
BBS1(1-575) (n = 98)
*
***

Fig. 1-11. Rescue of SMO and GPR161 localization in *BBS1*-KO cells upon the expression of WT and mutant BBS1

The #B1-1-23 cell line stably expressing mChe-fused BBS1(WT) (A, E, I, and M), BBS1(I399E) (B, F, J, and N), BBS1(R404A) (C, G, K, and O), or BBS1(1-575) (D, H, L, and P) were cultured and treated with SAG as described in the legend for Fig. 1-10, and triple immunostained for either SMO (A–H) or GPR161 (I–P), and ARL13B and FOP (A″–P″). (M and N) Relative staining intensities for SMO and GPR161 were estimated and expressed as described in the legend for Fig. 1-10. Values are means ± SD of three independent experiments. In each set of experiments, 31–44 (Q) and 31–45 (R) ciliated cells were analyzed, and the total numbers of ciliated cells analyzed (*n*) are shown. *, $p < 0.05$; ***, $p < 0.0001$ (one-way ANOVA followed by Tukey post-hoc analysis).

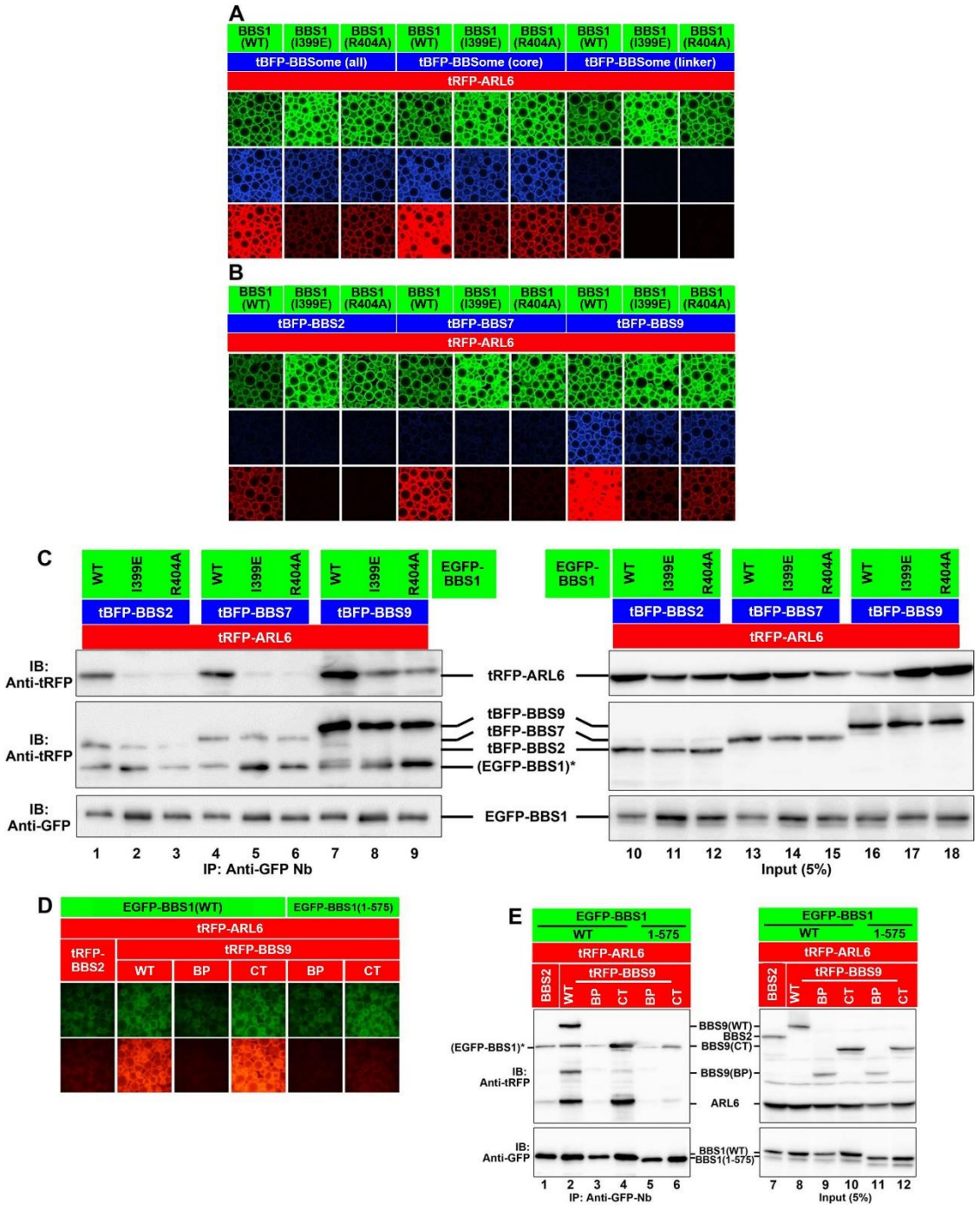
A
BBS1 (WT)
BBS1 (I399E)
BBS1 (R404A)
tBFP-BBSome (all)
tBFP-BBSome (core)
tBFP-BBSome (linker)
tRFP-ARL6
B
tBFP-BBS2
tBFP-BBS7
tBFP-BBS9
C
WT
I399E
R404A
EGFP-BBS1
IB: Anti-tRFP
IB: Anti-GFP
(EGFP-BBS1)*
IP: Anti-GFP Nb
Input (5%)
D
EGFP-BBS1(WT)
EGFP-BBS1(1-575)
tRFP-BBS2
BP
CT
E
1-575
BBS2
(EGFP-BBS1)*
BBS9(WT)
BBS9(CT)
BBS9(BP)
ARL6
BBS1(WT)
BBS1(1-575)

Fig. 1-12. The ARL6–BBS1 interaction is strengthened by BBS9

(A) HEK293T cells were transfected with expression vectors for an EGFP-fused BBS1 construct, as indicated, and tRFP-ARL6ΔN15(Q73L) together with tBFP-fusion vectors for all BBSome subunits (excepting BBS1), all core subunits (excepting BBS1), or all linker subunits. Lysates prepared from the transfected cells were processed for the VIP assay. Beads bearing fluorescent fusion proteins were observed using an A1R-MP confocal laser-scanning microscope. (B and C) HEK293T cells were transfected with expression vectors for an EGFP-fused BBS1 construct as indicated and tRFP-ARL6ΔN15(Q73L) together with tBFP-fused BBS2, BBS7, or BBS9. Lysates prepared from the transfected cells were processed for the VIP assay (B) or immunoblotting analysis (C) with anti-tRFP antibody, which reacts with tRFP and tBFP, and very weakly cross-reacts with EGFP (indicated by an asterisk) and with an anti-GFP antibody. (D and E) Lysates prepared from HEK293T cells cotransfected with expression vectors for an EGFP-fused BBS1 construct as indicated, and tRFP-ARL6ΔN15(Q73L) together with tRFP-fused BBS2 or a BBS9 construct as indicated were processed for the VIP assay (D) or immunoblotting analysis (E) with anti-tRFP antibody and anti-GFP antibody. The anti-tRFP antibody very weakly cross-reacts with EGFP (indicated by an asterisk).

DISCUSSION

The VIP assay, which was developed on the basis of a combination of preexisting methods, has some drawbacks compared with other qualitative assays, and more quantitative methods are required to measure precise affinity, stoichiometry, and kinetics of the interactions. However, this assay has following advantages over conventional qualitative protein–protein interaction assays: (i) visualization of a protein–protein interaction by observing red signals of immunoprecipitated beads with a conventional fluorescence microscope can detect the interaction more quickly by omitting labor-intensive and time-consuming procedures for immunoblotting; (ii) the VIP assay can determine interactions between more than two proteins at one time by using proteins fused to various fluorescent proteins, such as EGFP, tRFP, tBFP, and iRFP (Fig. 1-4); (iii) because the VIP assay is a modified coimmunoprecipitation assay, it can detect protein–protein interactions that take place under intracellular conditions; (iv) all tools for the VIP assay, such as various fluorescent proteins, GFP-Nb, and a conventional fluorescence microscope, are available to most molecular cell biologists; and (v) the VIP assay can easily determine the responsible proteins for complex interaction modes, such as one-to-many or many-to-many interactions (Fig. 1-12, A–C; see also Fig. 2-2 in the next chapter).

Protein trafficking within cilia is mediated by the IFT machinery composed of large protein complexes. The BBSome consists of eight BBS proteins encoded by causative genes of BBS and has been implicated in the trafficking of ciliary membrane proteins, including GPCRs. The membrane recruitment and coat-like assembly of the BBSome to promote cargo trafficking has been proposed to be regulated by the Arf-like small GTPase ARL6/BBS3, through its interaction with the BBS1 subunit. Using the VIP-based method, I here systematically investigated how the BBSome (Figs. 1-3 and 1-4) and the core subcomplex composed of BBS1, BBS2, BBS7, and BBS9 (Fig. 1-5, B–E) assembles and interacts with ARL6 (Fig. 1-5, F and G). The data presented here showed that the CT regions containing the GAE and PF domains, but not the BP domains (except for that of BBS1) of these core subunits mainly participate in the assembly of the core subcomplex (Fig. 1-5H). In other words, the BP domains of the core subunits are free from core subcomplex assembly. Taking into account the fact that the BP domains of the α-COP and δ-COP subunits of the COPI complex are responsible for recognition of cargo molecules (Ma and Goldberg, 2013; Jackson *et al.*, 2012), it is tempting to speculate that the BP domains of the BBSome subunits participate in cargo recognition, although my attempts to find interactions between the BBSome and

candidate cargo molecules have so far been unsuccessful. Klink *et al.* have recently reported that a recombinant BBSome semi-complex, which contained BBS1 and BBS9 but lacked BBS2 and BBS7, bound in vitro to synthetic peptides derived from ciliary GPCRs, SMO and SSTR3 (Klink *et al.*, 2017). Given that, in the genomes of Drosophila species, the BBS2 and BBS7 genes are absent (Shida *et al.*, 2010), BBS1 and/or BBS9 might play pivotal roles in cargo recognition, although it remains possible that other subunits also play some role.

Unexpectedly, my VIP-based analysis, supported by conventional immunoblotting analysis, also demonstrated that although BBS1 directly interacts with ARL6 via its BP domain as shown by a previous crystallographic study (Mourão *et al.*, 2014), the ARL6–BBS1 interaction can be indirectly strengthened by BBS9 (Fig. 1-12, B and C). In view of the facts that BBS1 interacts with BBS9 via its CT region (Fig. 1-5B) and that BBS9 did not show a direct interaction with ARL6 (Fig. 1-5F), how BBS9 supports the ARL6-BBS1 interaction is an interesting issue to address. One possible explanation is that the BBS1 protein on its own adopts a closed conformation, but upon binding of BBS9 to its CT region, the BBS1 protein undergoes a change in conformation so that ARL6 is now accessible to its BP domain. In support of this speculation, the interaction of ARL6 with the BP domain construct of BBS1 appears to be stronger than that with the BBS1(WT) construct (Fig. 1-5G). Another possibility is that BBS9 can somehow stabilize the ARL6–BBS1 dimer. If so, formation of the ARL6–BBS1 dimer, and subsequent BBS9 binding, can trigger the assembly of the whole BBSome complex. In any case, these data suggest that the ARL6–BBS1 interaction is maximally functional in the context of the BBSome complex.

In this chapter, I also established *BBS1*-KO RPE1 cells and showed that the absence of BBS1 impairs retrograde trafficking and/or export of GPR161, and possibly SMO (Fig. 1-10). This phenotype is in line with that reported for *ARL6*-KO cells (Liew *et al.*, 2010; Zhang *et al.*, 2011). The impaired trafficking of these ciliary GPCRs was rescued by the exogenous expression of BBS1(WT), but not by its mutant, BBS1(1–575), defective in BBS9 binding due to the lack of only 18-amino acids from the C-terminus (Fig. 1-11). As BBS1(1–575) retains the ability to interact with BBS7 and ARL6, the data of rescue experiments indicate that the integrity of the whole BBSome complex is crucial for its role in ciliary protein trafficking.

On the other hand, two BBS1 mutants, BBS1(I399E) and BBS1(R404A), which are defective in the binary interaction with ARL6 (Fig. 1-6, C and D) (Mourão *et al.*, 2014), were unexpectedly found to rescue the impaired GPCR trafficking in *BBS1*-KO cells (Fig. 1-11). Given that *ARL6*-KO cells (Liew *et al.*, 2010; Zhang *et al.*,

2011) show apparently the same phenotype as that of *BBS1*-KO cells (Fig. 1-11), it was intriguing that the BBS1 mutants defective in ARL6 binding were able to restore the impaired GPCR trafficking in *BBS1*-KO cells. However, I finally found that the BBS1 mutants demonstrate a substantial, although limited, interaction with ARL6 in the presence of BBS9, as described above. Therefore, how ARL6 is implicated in BBSome function; namely, whether it regulates the assembly of the BBSome or is a stoichiometric component of the BBSome will be an interesting issue to address in the future, although these roles are not mutually exclusive.

Chapter 2: Requirement of IFT-B–BBSome complex interaction in ciliary G protein-coupled receptor export

ABSTRACT

In the previous chapter, I determined the detailed architecture of the BBSome and the interaction between ARL6 with BBS1 aided by BBS9, and demonstrated that the BBSome regulates export of ciliary GPCRs from cilia. Given that the BBSome exhibits the IFT movement along the axoneme, it is likely that the driving force for the export of ciliary GPCRs is provided through an interaction of the BBSome with the IFT machinery. However, little is known about the connection between the IFT machinery and the BBSome. In this chapter, using the VIP assay, I identified the interaction between IFT38 from the IFT-B complex and the BBS1–BBS9 dimer from the BBSome. Furthermore, by analyzing phenotypes of *IFT38*-KO cells exogenously expressing IFT38(WT) or its mutant lacking the ability to interact with the BBS1–BBS9 dimer, I showed that KO cells expressing the IFT38 mutant have restored ciliogenesis; however, similar to *BBS1*-KO cells, they demonstrated persistent localization of GPR161 within cilia, even upon stimulation of Hh signaling. These results indicate that the IFT-B–BBSome interaction is required for the export of ciliary GPCRs across the ciliary gate.

INTRODUCTION

In the previous chapter, using the VIP assay, I revealed the overall architecture of the BBSome and the mode of interaction in the core subcomplex composed of BBS1, BBS2, BSB7, and BBS9 (Fig. 2-1A). Applying this flexible method to the IFT machinery, our group also revealed the overall architectures of the IFT-A and IFT-B complexes. The IFT-A complex can be divided into the core subcomplex composed three subunits (IFT122/140/144), which interacts with TULP3, and the peripheral subcomplex also composed of three subunits (IFT43/121/139) (Fig. 2-1B) (Hirano *et al.*, 2017; Takahara *et al.*, 2018). The IFT-B complex can be divided into the core (B1) subcomplex composed of ten subunits (IFT22/25/27/46/52/56/70/74/81/88) and the peripheral (B2) subcomplex composed of six subunits (IFT20/38/54/57/80/172); the two subcomplexes are connected by composite interactions involving two core subunits, IFT52 and IFT88, and two peripheral subunits, IFT38 and IFT57 (hereafter, the tetrameric unit is referred to as the 'connecting tetramer') (Fig. 2-1C) (Katoh *et al.*, 2016).

In addition to the detail architecture of the BBSome, I also demonstrated in the previous chapter that the BBSome regulates the export of ciliary GPCRs from cilia, by phenotypic analysis of *BBS1*-KO cells. Previous studies showed that the BBSome moves along the axonemal microtubules in association with IFT particles (Lechtreck *et al.*, 2009; Williams *et al.*, 2014), indicating that the BBSome gains the driving force for the export of ciliary GPCRs through its interactions with the IFT machinery.

In this chapter, I addressed the possibility that the IFT machinery regulates BBSome function via a direct interaction. Using the VIP assay, I found that the IFT-B–BBSome interaction involves IFT38 and the BBS1–BBS9 dimer. Furthermore, by analyzing phenotypes of *IFT38*-KO cell lines exogenously expressing an IFT38 deletion construct defective in the interaction with the BBS1–BBS9 dimer, I showed that the IFT-B–BBSome interaction is required for the GPCR export from cilia.

RESULTS

IFT-B–BBSome interaction is mediated by IFT38 and BBS1–BBS9

During the course of our study revealing the architectures of various ciliary protein complexes by using the VIP assay, we have sophisticated the strategy to identify not only binary but also one-to-many and many-to-many protein interactions (Funabashi *et al.*, 2017; Funabashi *et al.*, 2018; Hamada *et al.*, 2018; Hirano *et al.*, 2017; Katoh *et al.*, 2018; Katoh *et al.*, 2016). I then applied this strategy to find a potential interface between the IFT machinery and the BBSome. When lysates were prepared from HEK293T cells coexpressing either all IFT-B subunits or all IFT-A subunits fused to EGFP and all BBSome subunits plus ARL6 fused to tRFP were subjected to the VIP assay, red signals on the precipitated beads were below the detection level (Fig. 2-2A, columns 2 and 6). Furthermore, I could not detect clear red signals when all the BBSome subunits fused to tRFP were coexpressed with all the core or peripheral subunits of the IFT-A or IFT-B complex fused to EGFP. However, when EGFP-fused components of the IFT-B-connecting tetramer, IFT38/52/57/88, were coexpressed with all the BBSome subunits fused to tRFP, weak red signals were detected on the precipitated beads (Fig. 2-2A, column 5). When each subunit of the connecting tetramer fused to EGFP was separately coexpressed with tRFP-fused BBSome subunits, red signals were detected only in the case of EGFP-IFT38 (Fig. 2-2B). These results indicate that IFT38 in the IFT-B complex is involved in the IFT-B–BBSome interaction.

I then addressed which BBSome subunit(s) participate in the IFT-B–BBSome interaction. To this end, I performed the subtractive VIP assay. When an individual subunit of the BBSome or ARL6 fused to tRFP was omitted from the VIP assay, red signals were diminished in the absence of tRFP-tagged BBS1 or BBS9 (Fig. 2-2C), suggesting potential involvement of these two BBSome subunits in the IFT-B–BBSome interaction. I then analyzed whether these two BBSome subunits indeed interact with IFT38. No red signals were detected when mChe-fused BBS1 or BBS9 alone was coexpressed with EGFP-IFT38 (Fig. 2-2D); in this experiment, I used mChe-fused BBS proteins instead of tRFP-fused proteins, because the anti-tRFP antibody cross-reacts with EGFP, whereas the anti-RFP antibody, which can detect mChe, does not cross-react with EGFP. By contrast, robust red signals were detected when both mChe-BBS1 and mChe-BBS9 were coexpressed (Fig. 2-2D). The VIP data were confirmed by conventional immunoblotting analysis (Fig. 2-2E); mChe-fused BBS1 and BBS9, but not BBS1 or BBS9 alone, was coimmunoprecipitated with EGFP-IFT38. On the basis of these data, I conclude that the IFT-B–BBSome interaction is mediated by IFT38 and

the BBS1–BBS9 dimer (see Fig. 2-3A).

CT region of IFT38 is required for its interaction with BBS1–BBS9

I then set out to determine the region of IFT38 that is responsible for its interaction with the BBS1–BBS9 dimer, as our group previously showed that IFT38 acts as a hub subunit in the IFT-B complex (Katoh *et al.*, 2016); it directly interacts with IFT20 and IFT80 in the peripheral subcomplex, and constitutes an interface between the core and peripheral subcomplex by forming the connecting tetramer together with IFT52+IFT57+IFT88 (see Fig. 2-3A).

To this end, I utilized various IFT38 constructs, which were used in our previous study (Katoh *et al.*, 2016). As shown in Fig. 2-3B, row 3, an IFT38 construct (ΔN, residues 120–413) lacking the N-terminal NN-CH domain retained the ability to interact with BBS1+BBS9. By contrast, an IFT38 construct lacking the CT region (ΔC, residues 1–328) did not interact with BBS1+BBS9 (row 2). On the other hand, both the CT construct (residues 329–413) and the CC construct (residues 120–328) on its own did not interact with BBS1+BBS9 (rows 6 and 5, respectively).

The VIP data were confirmed by conventional immunoblotting analysis. As shown in Fig. 2-3C, the IFT38(ΔN) construct coimmunoprecipitated BBS1+BBS9 at a level comparable to IFT38(WT) (compare lane 4 with lane 2). By contrast, the IFT38(ΔC) construct did not coimmunoprecipitate BBS1+BBS9 (lane 3). Furthermore, none of the other IFT38 deletion constructs that were analyzed coimmunoprecipitated BBS1+BBS9 (lanes 5–7). Altogether, the CC and CT regions of IFT38 mainly participate in its interaction with the BBS1–BBS9 dimer.

The interaction mode of the IFT38 constructs with the BBS1–BBS9 dimer can be distinguished from those with the other IFT-B subunits. As reported previously (Katoh *et al.*, 2016), IFT38 directly interacts with IFT20 and IFT80 via its CC and NN-CH regions, respectively (Fig. 2-3D, columns 1 and 2, respectively; also see Fig. 2-3F); the IFT38(ΔC) construct retained the ability to interact with both IFT20 and IFT80 (row 2). On the other hand, IFT38 forms the connecting tetramer together with IFT52+IFT57+IFT88 to make an interface between the peripheral and core subcomplexes (see Fig. 2-3A). As shown in Fig. 2-3D, column 3 (also see Fig. 2-3F), the CC region of IFT38 participates in formation of the connecting tetramer; again, the IFT38(ΔC) construct retained the ability to form the connecting tetramer (row 2). The ability of the IFT38(ΔC) construct to form the connecting tetramer was also confirmed by immunoblotting analysis. As shown in Fig. 2-3E, EGFP-IFT38(ΔC) coimmunoprecipitated mChe-fused IFT52, IFT57, and IFT88, to an extent comparable

to that of EGFP-IFT38(WT) (compare lane 3 with lane 2). By comparing the abilities of these IFT38 constructs to interact with the other IFT-B subunits summarized in Fig. 2-3F, I conclude that the IFT38(ΔC) construct has specifically lost the ability to interact with the BBS1–BBS9 dimer.

I also attempted to identify a BBS1 or BBS9 mutant that specifically loses the ability to interact with IFT38 but retains the ability to interact with other BBSome subunits and ARL6. However, my attempts have been unsuccessful so far, as BBS1 and BBS9 interact with various BBSome subunits and ARL6 (see Fig. 2-3A).

IFT38(WT) and IFT38(ΔC) differentially restore ciliogenesis and BBSome localization in *IFT38*-KO cells

In this chapter, I established *IFT38*-KO lines of hTERT-RPE1 cells, using the CRISPR/Cas9-mediated system, to compare the phenotypes of the *IFT38*-KO cells with those of BBS1 KO cells (Chapter 1). For the following experiments, I selected two independent *IFT38*-KO cell lines, #38-1-15 and #38-1-17, both of which have a one nucleotide deletion (but at distinct nucleotides, c.51delA and c.50delG, respectively) in one IFT38 allele, and a reverse integration of the donor knock-in vector in the other allele (for detailed characterization, see Fig. 2-4, A–C). As previously reported for *Ift38*-KO MEFs (Botilde *et al.*, 2013; Katoh *et al.*, 2016), the *IFT38*-KO RPE1 cell lines demonstrated the no-cilia phenotype (Fig. 2-5, compare B and C with A).

To exclude the potential off-target effects of the CRISPR/Cas9 system, I performed a rescue experiment. When mChe-fused IFT38(WT), but not mChe, was stably expressed in the *IFT38*-KO cell lines #38-1-15 and #38-1-17, ciliogenesis was restored (Fig. 2-5, D and E; also see Fig. 2-5G), confirming that the no-cilia phenotype was specific to disruption of the IFT38 gene. On the other hand, exogenously expressed mChe-IFT38(ΔC) also restored ciliogenesis essentially to the same extent as that of mChe-fused IFT38(WT) (Fig. 2-5F; also see Fig. 2-5G), in good agreement with our previous study showing that exogenously expressed IFT38(ΔC) was able to rescue ciliogenesis defects of *Ift38*-KO MEFs (Katoh *et al.*, 2016). These results indicate that the IFT38 CT region, which is dispensable for assembly of the IFT-B complex (see Fig. 2-3F), is not essential for the biogenesis of cilia. However, I noticed that *IFT38*-KO cells expressing IFT38(ΔC) tended to grow longer cilia than IFT38(WT)-expressing cells (Fig. 2-5, compare E and F). Indeed, the difference in ciliary length between the IFT38(WT)-expressing and IFT38(ΔC)-expressing cells was statistically significant for both #38-1-15 and #38-1-17 cell lines (Fig. 2-5H).

I next analyzed the localization of IFT88 (an IFT-B subunit) and IFT140 (an

IFT-A subunit) in IFT38(WT)-expressing and IFT38(ΔC)-expressing *IFT38*-KO cells. As shown in Fig. 2-6, A and B, IFT88 staining was observed mainly around the base of cilia and faintly along the axoneme, as in control RPE1 cells. IFT140 staining was found predominantly at the ciliary base in both IFT38(WT)-expressing and IFT38(ΔC)-expressing *IFT38*-KO cells (Fig. 2-6, C and D), as in control RPE1 cells. Thus, the C-terminal truncation of IFT38 did not affect the localization of components of the IFT machinery.

I next analyzed the localization of the BBSome in *IFT38*-KO cells expressing mChe-fused IFT38(WT) and IFT38(ΔC). When cells were immunostained for BBS9, this protein was found within the cilia of approximately 40% of IFT38(WT)-expressing and IFT38(ΔC)-expressing *IFT38*-KO cells (Fig. 2-6, E and F; also see Fig. 2-6I). Quantitative analysis demonstrated that the total ciliary staining intensity for BBS9 was not significantly different between IFT38(WT)-expressing and IFT38(ΔC)-expressing *IFT38*-KO cells (Fig. 2-6J), although BBS9 staining intensity per unit length of cilia was considerably lower in IFT38(ΔC)-expressing cells than in IFT38(WT)-expressing cells (Fig. 2-6K), as cilia of IFT38(ΔC)-expressing cells were longer than those of IFT38(WT)-expressing cells (Fig. 2-5H). Essentially the same results were obtained when IFT38(WT)-expressing and IFT38(ΔC)-expressing *IFT38*-KO cells were immunostained for ARL6 (Fig. 2-6, G, H, and L–N). Taken together, it is therefore likely that the lack of interaction of the IFT machinery with the BBSome leads to a reduction in the concentration of the BBSome within cilia.

GPR161 export from cilia is impaired in *IFT38*-KO cells expressing IFT38(ΔC)

As the BBSome has been shown to participate in the export of GPCRs, including GPR161 (Fig. 1-10, G–L), from cilia (Eguether *et al.*, 2014; Liew *et al.*, 2014; Ye *et al.*, 2018), I then analyzed changes in the localization of SMO and GPR161 upon the stimulation of Hh signaling. SMO is excluded from cilia under basal conditions but enters cilia upon treatment of cells with SAG, whereas GPR161 negatively regulates Hh signaling on the ciliary membrane under basal conditions but exits cilia upon SAG treatment, as I showed in Fig. 1-10, A, D, G, and J. In the *IFT38*-KO cell line #38-1-15, which stably expresses mChe-IFT38(WT), SMO was absent from cilia under basal conditions (Fig. 2-7A), whereas it was observed within cilia upon SAG treatment (Fig. 2-7C; also see Fig. 2-7I). In contrast to SMO, GPR161 was found within cilia in the absence of SAG (Fig. 2-7E), whereas it was exported from cilia by SAG treatment (Fig. 2-7G, also see Fig. 2-7J). Essentially the same results were obtained using the other KO cell line, #38-1-17, stably expressing IFT38(WT) (Fig. 2-7, I and J).

I also analyzed the localization of SMO and GPR161 in *IFT38*-KO cells stably expressing mChe-IFT38(ΔC). In the absence of SAG, IFT38(ΔC)-expressing *IFT38*-KO cells tended to have slightly higher levels of SMO within cilia than IFT38(WT)-expressing cells, although the results were not statistically significant (Fig. 2-7, compare B with A; also see Fig. 2-7I). Upon SAG treatment, SMO entered cilia at levels comparable between IFT38(WT)-expressing and IFT38(ΔC)-expressing *IFT38*-KO cells (Fig. 2-7, C and D; also see Fig. 2-7I). On the other hand, in IFT38(ΔC)-expressing *IFT38*-KO cells, the export of GPR161 from cilia upon stimulation with SAG was greatly reduced (Fig. 2-7, compare H with G; also see Fig. 2-7J).

These observations altogether indicate that the export of GPCRs from cilia is impaired in *IFT38*-KO cells expressing IFT38(ΔC). It is noteworthy that the phenotype of IFT38(ΔC)-expressing *IFT38*-KO cells, with respect to the localization of SMO and GRP161 under basal and SAG-stimulated conditions, closely resembled that of *BBS1*-KO RPE1 cells (see Fig. 1-10).

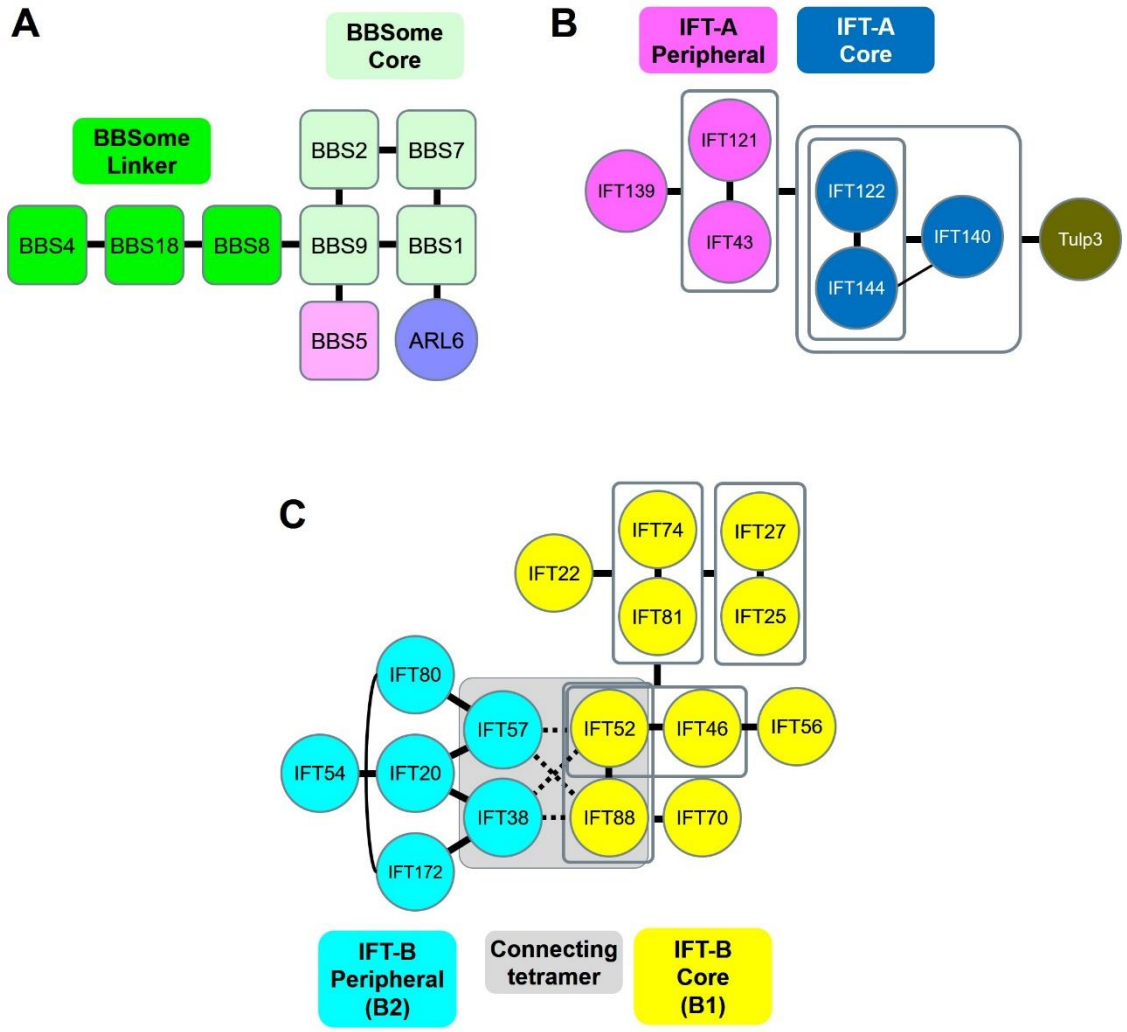

Fig. 2-1 Architectures of the BBSome and the IFT-A and IFT-B complexes

Architectures of the BBSome revealed in Chapter 1 and the IFT-A and IFT-B complexes revealed in our previous studies (Katoh *et al.*, 2016; Hirano *et al.*, 2017). (A) The BBSome can be divided into the core subcomplex composed of BBS1/2/7/9, which interacts with BBS5 via BBS9 and ARL6 via BBS1, and the linker subcomplex composed of BBS4/8/18. (B) The IFT-A complex can be divided into the core subcomplex composed of IFT122/140/144, which interacts with TULP3, and the peripheral subcomplex composed of IFT43/121/139. (C) The IFT-B complex is composed of the core (B1) and peripheral (B2) subcomplexes, which are composed of 10 subunits (IFT22/25/27/46/52/56/70/74/81/88) and six subunits (IFT20/38/54/57/80/172), respectively; these subcomplexes are linked by composite interactions involving the connecting tetramer IFT38/52/57/88.

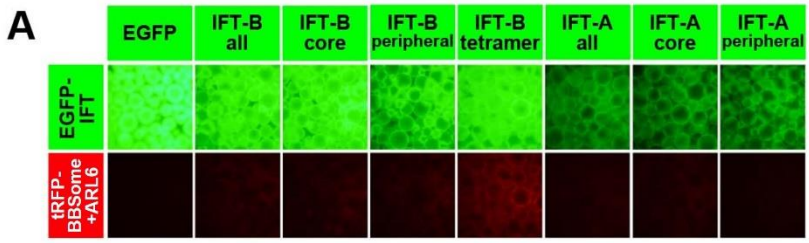
A
EGFP
IFT-B all
IFT-B core
IFT-B peripheral
IFT-B tetramer
IFT-A all
IFT-A core
IFT-A peripheral
EGFP-IFT
tRFP-BBSome +ARL6

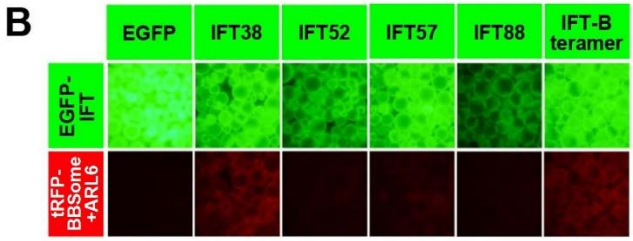
B
EGFP
IFT38
IFT52
IFT57
IFT88
IFT-B teramer
EGFP-IFT
tRFP-BBSome +ARL6

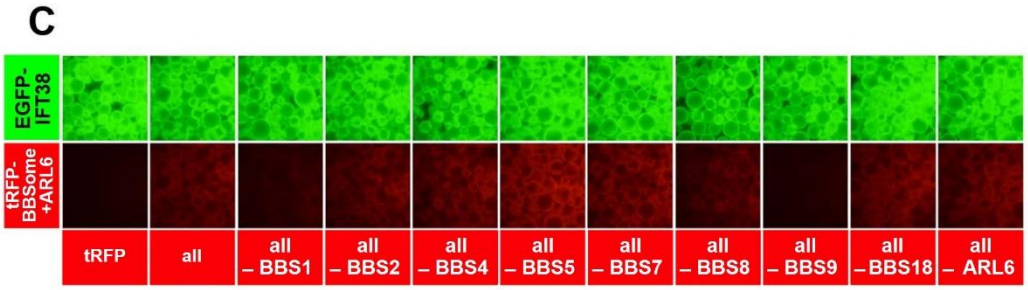
C
EGFP-IFT38
tRFP-BBSome +ARL6
tRFP
all
all – BBS1
all – BBS2
all – BBS4
all – BBS5
all – BBS7
all – BBS8
all – BBS9
all – BBS18
all – ARL6

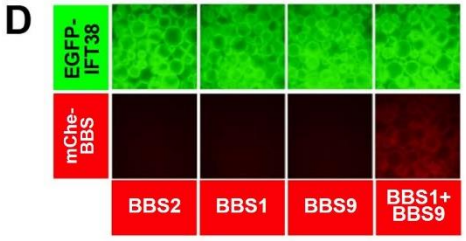
D
EGFP-IFT38
mChe-BBS
BBS2
BBS1
BBS9
BBS1+ BBS9

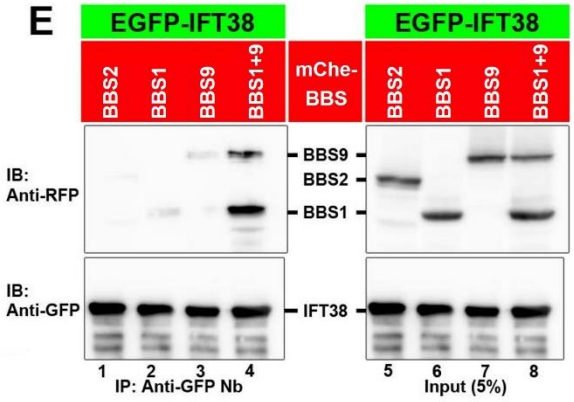
E
EGFP-IFT38
EGFP-IFT38
BBS2
BBS1
BBS9
BBS1+9
mChe-BBS
BBS2
BBS1
BBS9
BBS1+9
IB: Anti-RFP
IB: Anti-GFP
BBS9
BBS2
BBS1
IFT38
1 2 3 4
IP: Anti-GFP Nb
5 6 7 8
Input (5%)

Fig. 2-2. Identification of an interaction between IFT38 and the BBS1–BBS9 dimer
(A) Subunits of the IFT-B-connecting tetramer interact with the BBSome. HEK293T cells were cotransfected with expression vectors for EGFP-fused subunits of the IFT-B or IFT-A complex as indicated, and all the BBSome subunits plus ARL6 fused to tRFP. Twenty-four hours after transfection, lysates were prepared from the transfected cells and immunoprecipitated with GST-tagged anti-GFP Nb prebound to glutathione-Sepharose 4B beads and processed for the VIP assay. (B) Identification of IFT38 as an IFT-B subunit responsible for BBSome interaction. Lysates were prepared from HEK293T cells coexpressing EGFP-fused IFT-B subunits as indicated, and all the BBSome subunits plus ARL6 fused to tRFP, and subjected to the VIP assay. (C) Subtractive VIP assay to identify candidate BBSome subunits interacting with IFT38. Lysates prepared from HEK293T cells coexpressing EGFP-IFT38 and all but one (as indicated) subunits of the BBSome plus ARL6 fused to tRFP were processed for the VIP assay. (D, E) Identification of BBS1–BBS9 as BBSome subunits responsible for the interaction with IFT38. Lysates prepared from HEK293T cells expressing EGFP-IFT38 together with mChe-fused BBS1 (lane 2) or BBS9 (lane 3) or both (lane 4) were processed for the VIP assay (D) or conventional immunoblotting analysis (E) using an anti-RFP antibody (upper panels), that reacts with mChe, or an anti-GFP antibody (lower panels). mChe-BBS2 was used as a negative control (lane 1).

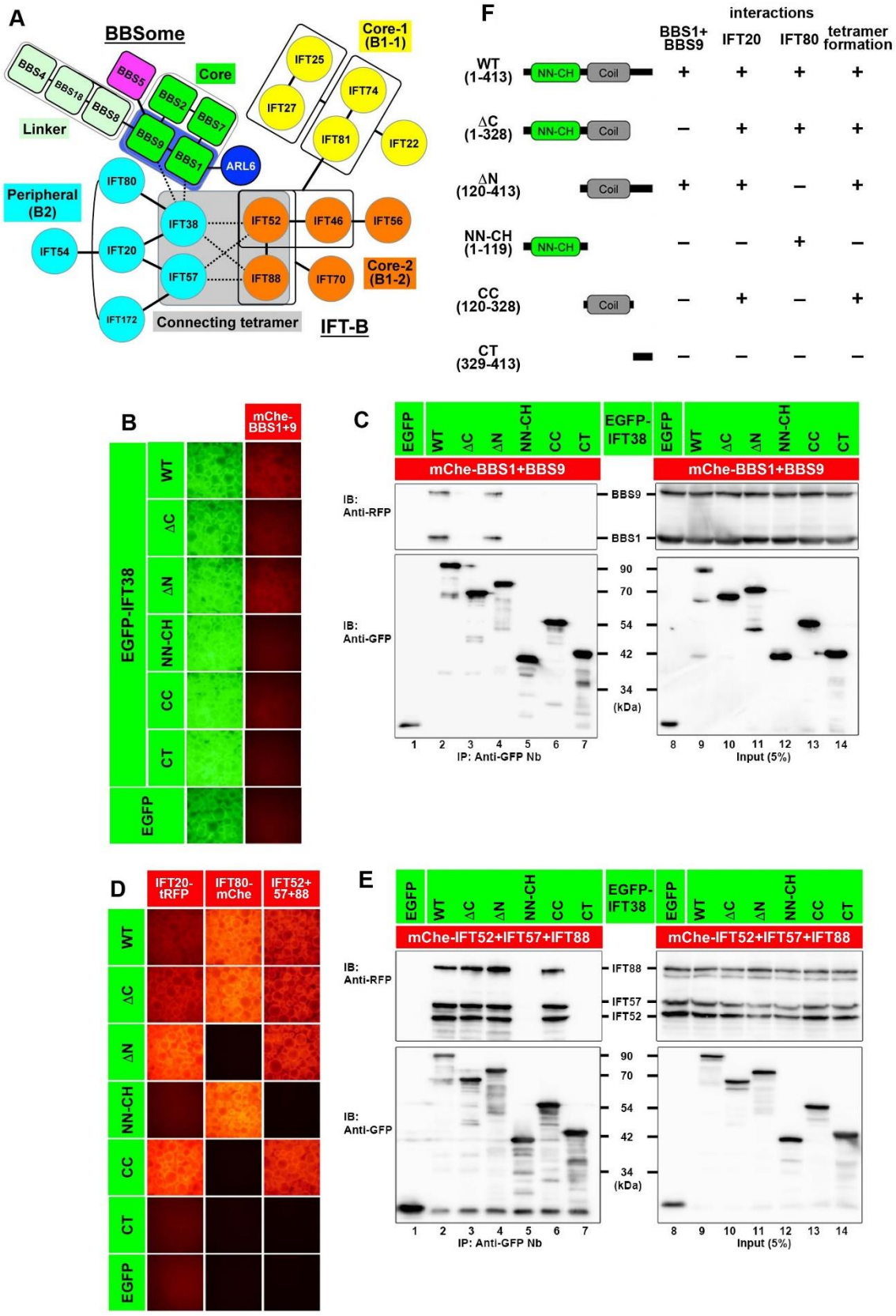
A
BBSome
Core
Linker
Peripheral (B2)
Core-1 (B1-1)
Core-2 (B1-2)
Connecting tetramer
IFT-B
BBS4
BBS18
BBS8
BBS5
BBS2
BBS7
BBS9
BBS1
ARL6
IFT80
IFT38
IFT54
IFT20
IFT57
IFT172
IFT52
IFT46
IFT56
IFT88
IFT70
IFT25
IFT27
IFT74
IFT81
IFT22
F
interactions
BBS1+ BBS9
IFT20
IFT80
tetramer formation
WT (1-413)
ΔC (1-328)
ΔN (120-413)
NN-CH (1-119)
CC (120-328)
CT (329-413)
NN-CH
Coil
B
mChe-BBS1+9
EGFP-IFT38
WT
ΔC
ΔN
NN-CH
CC
CT
EGFP
C
EGFP
EGFP-IFT38
mChe-BBS1+BBS9
IB: Anti-RFP
IB: Anti-GFP
BBS9
BBS1
90
70
54
42
34
(kDa)
IP: Anti-GFP Nb
Input (5%)
D
IFT20-tRFP
IFT80-mChe
IFT52+57+88
E
mChe-IFT52+IFT57+IFT88
IFT88
IFT57
IFT52

Fig. 2-3. Differentiation of the region of the IFT38 protein involved in BBSome binding from those involved in its interactions with other IFT-B subunits

(A) A model for the interaction of the BBSome with the IFT-B complex predicted from the data shown in Fig. 2-2. (B, C) The CT region of IFT38 is essential for its interaction with the BBS1–BBS9 dimer. Lysates prepared from HEK293T cells expressing any of the EGFP-IFT38 constructs schematically shown in Fig. 2-3F (left side) together with mChe-fused BBS1+BBS9 were processed for the VIP assay (B) or immunoblotting analysis (C) using an anti-RFP antibody (upper panels) or an anti-GFP antibody (lower panels). (D) Determination of regions of the IFT38 protein involved in its interactions with IFT20, IFT80, and IFT52+IFT57+IFT88 (the other subunits of the connecting tetramer). Lysates prepared from HEK293T cells expressing any of the EGFP-IFT38 constructs (Fig. 2-3F, left side) together with mChe-fused IFT20 (left column), IFT80 (middle column), or IFT52+IFT57+IFT88 (right column) were processed for the VIP assay. (E) Beads bearing EGFP-fused and mChe-fused IFT proteins used in the right column of Fig. 2-3D were processed for immunoblotting analysis using an anti-RFP antibody (upper panels) or an anti-GFP antibody (lower panels). (F) Summary of the results shown in Fig. 2-3, B–E. (+), robust interaction; (–), no interaction.

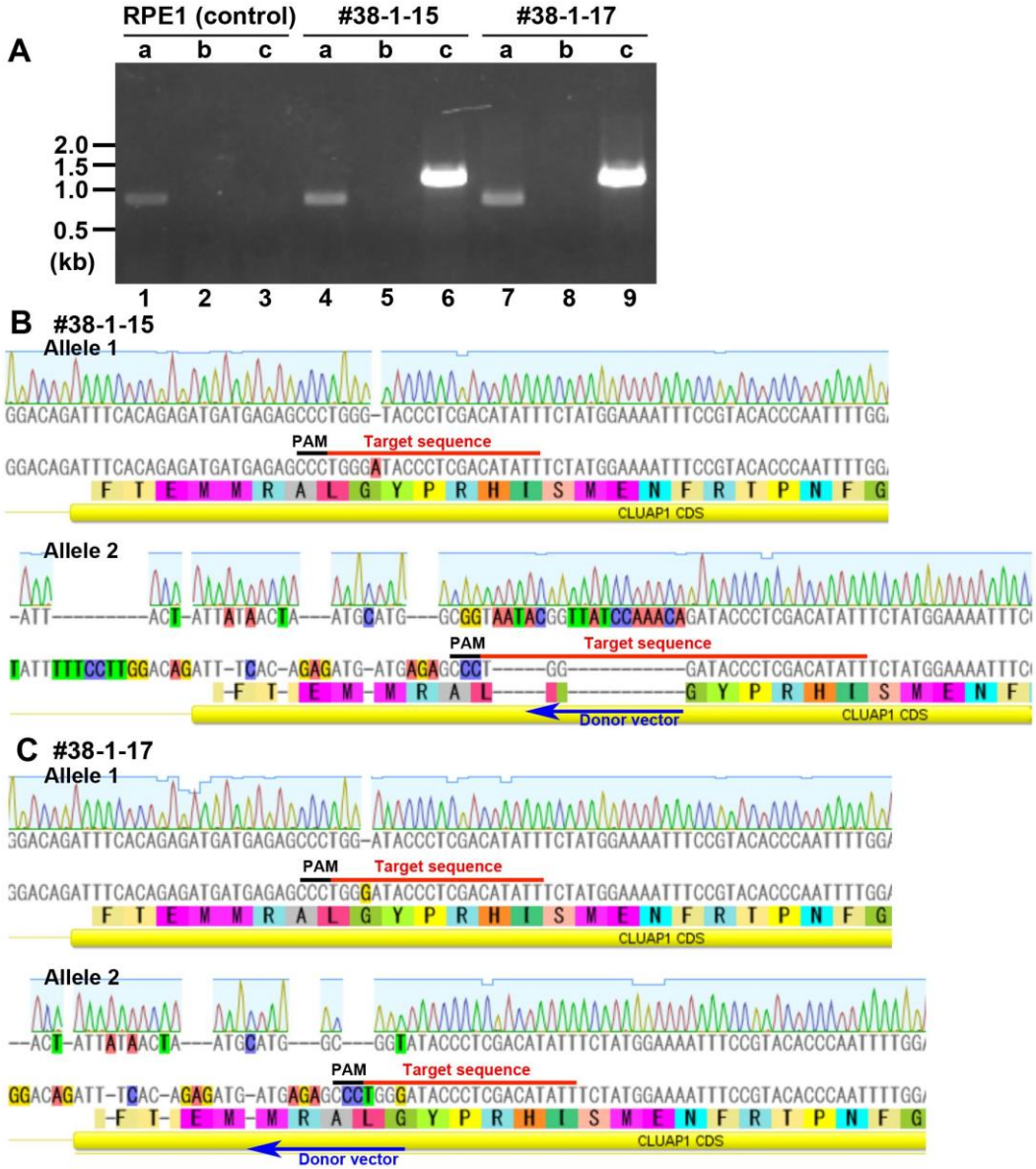

Fig. 2-4. Genomic PCR and sequence analyses of the *IFT38*-KO cell lines

Genomic DNAs extracted from control hTERT-RPE1 cells and from the *IFT38*-KO cell lines #38-1-15 and #38-1-17, which were established using a donor knock-in vector containing the target sequence, were subjected to PCR analysis using the indicated primer sets (see Table 3) to detect alleles with a small indel or no insertion (a), or with forward (b) or reverse (c) integration of the donor knock-in vector. (B and C) Alignments of allele sequences of the #38-1-15 (B) and #38-1-17 (C) cell lines determined by sequencing of the PCR products shown in (A). Red and black lines indicate the target sequence and PAM sequence, respectively, and blue arrows indicate the direction of integration of the donor knock-in vector.

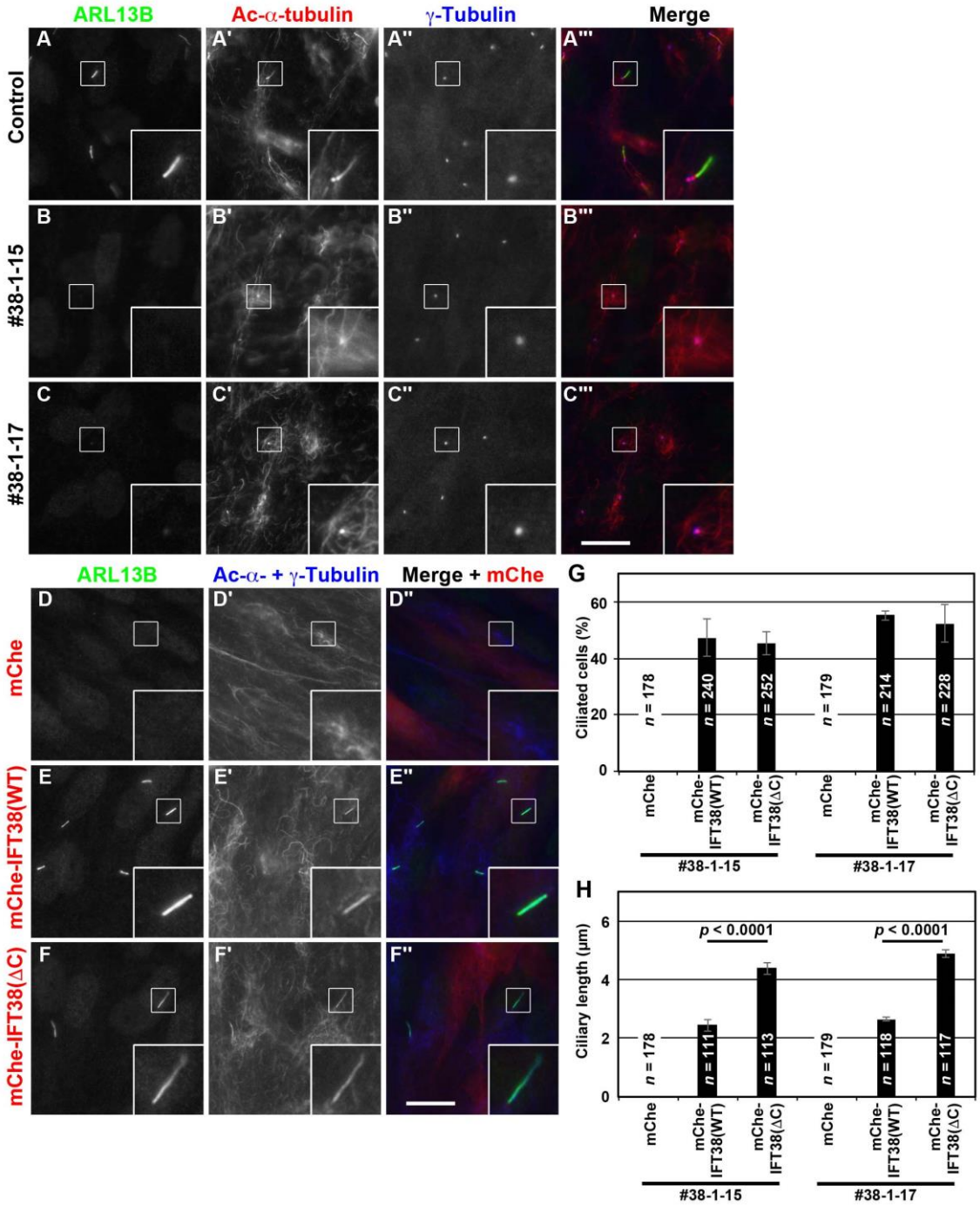
ARL13B
Ac-α-tubulin
γ-Tubulin
Merge
Control
#38-1-15
#38-1-17
A
A'
A''
A'''
B
B'
B''
B'''
C
C'
C''
C'''
ARL13B
Ac-α- + γ-Tubulin
Merge + mChe
mChe
mChe-IFT38(WT)
mChe-IFT38(ΔC)
D
D'
D''
E
E'
E''
F
F'
F''
G
Ciliated cells (%)
60
40
20
0
n = 178
n = 240
n = 252
n = 179
n = 214
n = 228
mChe
mChe-IFT38(WT)
mChe-IFT38(ΔC)
#38-1-15
#38-1-17
H
Ciliary length (μm)
6
4
2
0
p < 0.0001
p < 0.0001
n = 178
n = 111
n = 113
n = 179
n = 118
n = 117

Fig. 2-5. IFT38(WT) and IFT38(ΔC) differentially rescue ciliogenesis defects of *IFT38*-KO cells

(A–C) Control RPE1 cells and the *IFT38*-KO cell lines #38-1-15 and #38-1-17 were serum starved for 24 h and triple immunostained for IFT88 (A–C), Ac-α-tubulin (A′–C′), and γ-tubulin (A″–C″). (D–F) The *IFT38*-KO cell line #38-1-15, which stably expresses mChe (D), mChe-IFT38(WT) (E), or mChe-IFT38(ΔC) (F) were immunostained for ARL13B (D–F) and Ac-α-tubulin+γ-tubulin (D′–F′). Scale bars, 10 μm. (G) Ciliated cells of the *IFT38*-KO cell lines #38-1-15 and #38-1-17, which stably express mChe, mChe-IFT38(WT), or mChe-IFT38(ΔC) were counted, and percentages of ciliated cells are represented as bar graphs. The data are shown as means ± SD of three independent experiments. In each set of experiments, 51–108 cells were analyzed, and the total numbers of cells analyzed (*n*) are shown. (H) The length of cilia in the *IFT38*-KO cell lines #38-1-15 and #38-1-17, which stably express mChe, mChe-IFT38(WT), or mChe-IFT38(ΔC) was measured and expressed as bar graphs. Values are means ± SD of three independent experiments. In each set of experiments, 30–64 cells were analyzed, and the total numbers of cells analyzed (*n*) are shown. *p*-values were determined by the Student *t*-test.

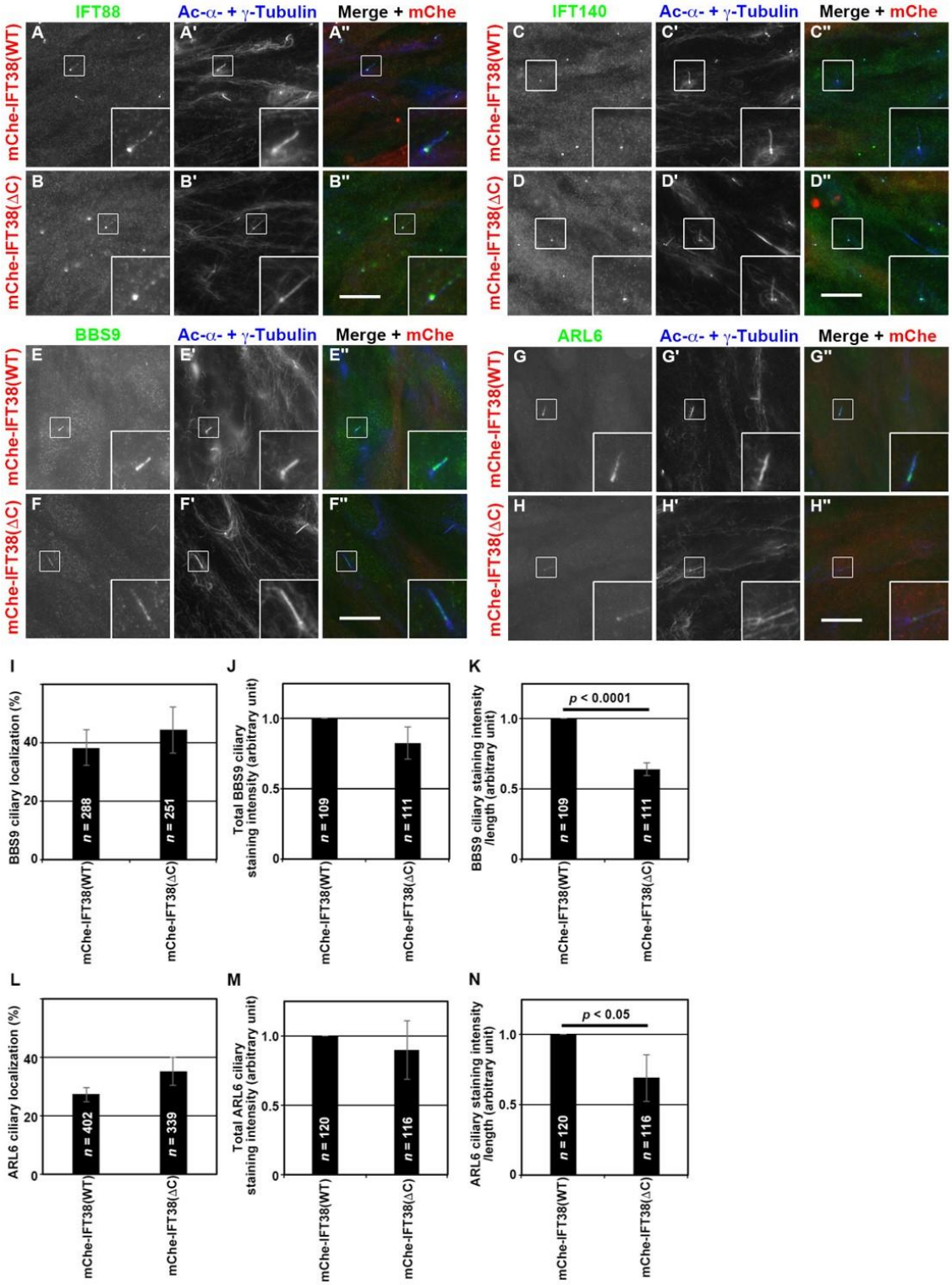
IFT88
Ac-α- + γ-Tubulin
Merge + mChe
IFT140
BBS9
ARL6
mChe-IFT38(WT)
mChe-IFT38(ΔC)
A
A'
A''
B
B'
B''
C
C'
C''
D
D'
D''
E
E'
E''
F
F'
F''
G
G'
G''
H
H'
H''
I
BBS9 ciliary localization (%)
n = 288
n = 251
J
Total BBS9 ciliary staining intensity (arbitrary unit)
n = 109
n = 111
K
p < 0.0001
BBS9 ciliary staining intensity /length (arbitrary unit)
L
ARL6 ciliary localization (%)
n = 402
n = 339
M
Total ARL6 ciliary staining intensity (arbitrary unit)
n = 120
n = 116
N
p < 0.05
ARL6 ciliary staining intensity /length (arbitrary unit)

Fig. 2-6. IFT38(ΔC)-expressing *IFT38*-KO cells are partially compromised with respect to BBSome trafficking into cilia

(A–D) The *IFT38*-KO cell line #38-1-15, which stably expresses mChe-IFT38(WT) or mChe-IFT38(ΔC), was serum starved for 24 h, and immunostained for IFT88 (A, B), IFT140 (C, D), BBS9 (E, F), or ARL6 (G, H), together with Ac-α-tubulin+FOP (A′–H′). Scale bars, 10 μm. (I, L) mChe-IFT38(WT)-expressing or mChe-IFT38(ΔC)-expressing *IFT38*-KO cells with ciliary localization of BBS9 (I) or ARL6 (L) were counted, and the percentages of ciliated cells with BBS9-positive (I) or ARL6-positive cilia (L) are represented as bar graphs. Values are means ± SD of three independent experiments. In each experiment, 68–107 (I) and 107–151 ciliated cells (L) were analyzed, and the total numbers of ciliated cells analyzed (*n*) are shown. (J, K, M, N) Ciliary fluorescence staining intensities of BBS9 and ARL6, and ciliary length in ciliated mChe-IFT38(WT)-expressing or mChe-IFT38(ΔC)-expressing *IFT38*-KO cells were measured, and the total staining intensities of BBS9 (J) and ARL6 (M), and those per unit ciliary length (K, N) are expressed as bar graphs. Values are means ± SD of three independent experiments. In each set of experiments, 31–47 (J, K) and 28–48 cells (M, N) were analyzed, and the total numbers of analyzed cells (*n*) are shown. *p*-values were determined by the Student *t*-test.

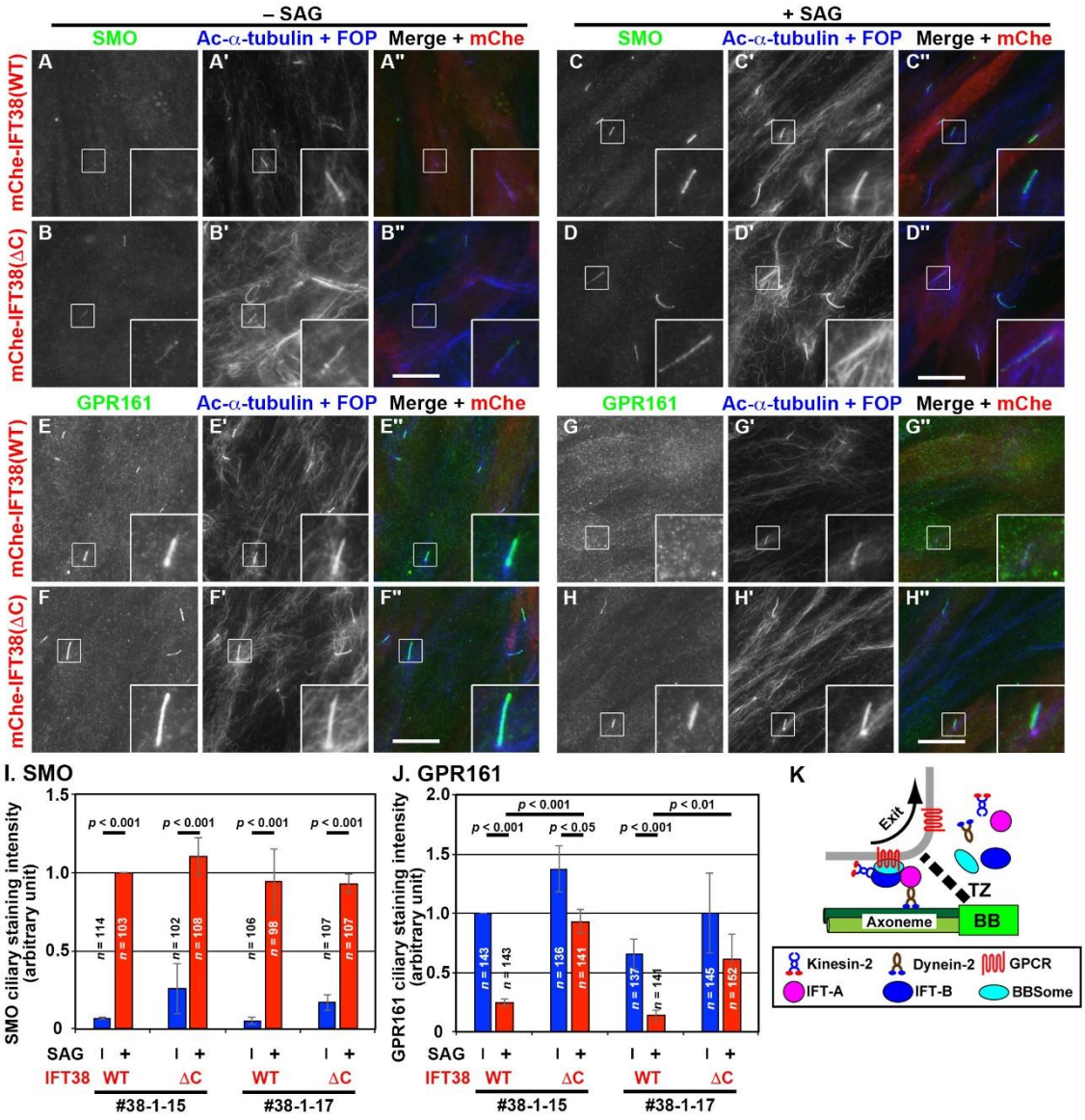
– SAG
+ SAG
SMO
Ac-α-tubulin + FOP
Merge + mChe
mChe-IFT38(WT)
mChe-IFT38(ΔC)
A
A'
A''
B
B'
B''
C
C'
C''
D
D'
D''
GPR161
E
E'
E''
F
F'
F''
G
G'
G''
H
H'
H''
I. SMO
SMO ciliary staining intensity (arbitrary unit)
p < 0.001
n = 114
n = 103
n = 102
n = 108
n = 106
n = 98
n = 107
n = 107
SAG
IFT38
WT
ΔC
#38-1-15
#38-1-17
J. GPR161
GPR161 ciliary staining intensity (arbitrary unit)
p < 0.01
p < 0.05
n = 143
n = 143
n = 136
n = 141
n = 137
n = 141
n = 145
n = 152
K
Exit
TZ
Axoneme
BB
Kinesin-2
Dynein-2
GPCR
IFT-A
IFT-B
BBSome

Fig. 2-7. IFT38(ΔC)-expressing *IFT38*-KO cells show impaired export of GPR161 upon SAG treatment

(A–H) The *IFT38*-KO cell line #38-1-15, which stably expresses mChe-IFT38(WT) or mChe-IFT38(ΔC), was serum-starved for 24 h and further cultured for 24 h in the absence (–SAG) or presence (+SAG) of 200 nM SAG. The cells were immunostained for either SMO (A–D) or GPR161 (E–H) and Ac-α-tubulin+FOP (A′–H′). Scale bars, 10 μm. (I, J) Fluorescence staining intensities of SMO (I) and GPR161 (J) in the *IFT38*-KO cell lines #38-1-15 and #38-1-17, which stably express mChe-IFT38(WT) or mChe-IFT38(ΔC) were measured, and relative intensities of the cells are expressed as bar graphs. Values are means ± SD of three independent experiments. In each set of experiments, 31–41 (I) and 32–46 (J) ciliated cells were analyzed and the total numbers of ciliated cells analyzed (*n*) are shown. *p*-values were determined by one-way ANOVA followed by Tukey post-hoc analysis for comparison among cell lines, and by the Student *t*-test for comparison between cells with and without SAG treatment. (K) A model for the interplay among IFT-A, IFT-B, and BBSome complexes and the dynein-2 motor in the export of GPCRs from cilia. TZ, transition zone; BB, basal body.

DISCUSSION

In this chapter, I determined for the first time to my knowledge, the mode of interaction between the IFT machinery and the BBSome. My analyses utilizing the VIP assay unequivocally showed that IFT38 and the BBS1–BBS9 dimer constitute the IFT-B–BBSome interface, and that the CT region of IFT38 is essential for its interaction with BBS1–BBS9 (Figs. 2-2 and 2-3). These results are compatible with a previous interactome study indicating that IFT38 and other IFT-B subunits interact, directly or indirectly, with BBSome subunits, including BBS1 and BBS9 (Boldt *et al.*, 2016).

In addition to its interaction with the BBSome, our previous studies showed that IFT38 serves as a hub subunit of the IFT-B complex, as follows: (1) by directly interacting with IFT20 and IFT80, IFT38 constitutes the IFT-B peripheral (IFT-B2) subcomplex (Katoh *et al.*, 2016); (2) composite interactions involving IFT38 and IFT57 from the peripheral subcomplex and IFT52 and IFT88 from the core (IFT-B1) subcomplex constitute the interface between the two subcomplexes (Katoh *et al.*, 2016); and (3) the connecting tetramer, IFT38/52/57/88, is a binding site for heterotrimeric kinesin-II (Funabashi *et al.*, 2018). The crucial role of IFT38 in the IFT machinery is corroborated by the fact that *IFT38*-KO cells completely lack cilia (Fig. 2-5; also see (Botilde *et al.*, 2013; Katoh *et al.*, 2016)).

On the other hand, BBS1 and BBS9 constitute the BBSome core subcomplex (Jin *et al.*, 2010; Nachury *et al.*, 2007; see also Figs. 1-3 and 1-4) and interact with ARL6 (see Fig. 1-12). Furthermore, BBS9 interacts with BBS5, which mediates the membrane association of the BBSome (Nachury *et al.*, 2007), and with BBS8 of the BBSome linker subcomplex.

When the IFT38(ΔC) construct, which retains the ability to interact with other IFT-B subunits but lacks the ability to interact with the BBS1–BBS9 dimer (Fig. 2-3), was expressed in *IFT38*-KO RPE1 cells, it restored the ciliogenesis defect of the KO cells, like IFT38(WT), although IFT38(ΔC)-expressing *IFT38*-KO cells grew significantly longer cilia than IFT38(WT)-expressing cells (Fig. 2-5). The most notable defect observed in IFT38(ΔC)-expressing *IFT38*-KO cells was that export of GPR161 from cilia in response to Hh signaling stimulation was severely impaired (Fig. 2-7). This phenotype closely resembles that of *BBS1*-KO RPE1 cells (see Fig. 1-10) and *BBS9*-KO cells (my unpublished results).

At the beginning of this study, I hypothesized three possibilities, although mutually exclusive, regarding the role of the IFT-B–BBSome interaction in ciliary protein trafficking: (1) the IFT-B–BBSome interaction is required for normal

assembly/trafficking of the IFT machinery, as a previous study in *Caenorhabditis elegans* implicated the role of the BBSome in the assembly of IFT particles at the basal body (Wei *et al.*, 2012), although the data shown in Fig. 1-9, M–R, indicated that assembly and trafficking of the IFT machinery appeared normal in *BBS1*-KO RPE1 cells; (2) the IFT-B–BBSome interaction is required for ciliary entry and/or anterograde trafficking of the BBSome, as the BBSome was suggested to move along the axonemal microtubules in association with IFT particles in *Chlamydomonas* flagella and in mammalian olfactory cilia (Lechtreck *et al.*, 2009; Williams *et al.*, 2014); and (3) export of GPCRs from cilia is dependent on the IFT-B–BBSome interaction, in view of my observations using *BBS1*-KO cells in Chapter 1.

The first possibility is unlikely because the localization of an IFT-B (IFT88) and an IFT-A (IFT140) subunit was not different between IFT38(WT)-expressing and IFT38(ΔC)-expressing *IFT38*-KO cells. The second possibility is also unlikely, although not completely excluded, as the total amount of the BBSome within cilia was not significantly different between IFT38(WT)-expressing and IFT38(ΔC)-expressing cells, although the BBSome concentration within cilia appeared slightly lower in IFT38(ΔC)-expressing *IFT38*-KO cells than in IFT38(WT)-expressing cells, due to longer cilia of the former cells. The third possibility is therefore most likely; namely, the BBSome mediates the export of ciliary GPCRs across the TZ and periciliary barrier, which constitutes the ciliary gate, in a manner dependent on its interaction with the IFT machinery.

Retrograde trafficking, and probably export, of ciliary proteins are mediated by the IFT-A complex with the aid of the dynein-2 motor. In this chapter, however, I am unable to confirm a direct interaction of the BBSome with the IFT-A complex, but did observe the IFT-B–BBSome interaction (Fig. 2-2). Given that the BBSome mediates the lateral transport of ciliary GPCR across the ciliary gate (Ye *et al.*, 2018), the most likely mechanism for export of ciliary GPCR is as follows (see Fig. 2-7K): (1) lateral transport across the ciliary gate is powered by the dynein-2 motor, which is associated with the IFT-A complex; and (2) the IFT-B and IFT-A complexes assemble into the IFT machinery. In this context, our group recently found an interaction interface between the IFT-A and IFT-B complexes and showed that ciliary entry of the IFT-A complex requires its interaction with the IFT-B complex (Kobayashi, Katoh, and Nakayama, manuscript in preparation); and (3) the BBSome connects ciliary GPCR to the IFT-B complex.

Involvement of the IFT-B complex in the export of ciliary GPCR was somewhat unexpected, because it has long been believed that the IFT-B and IFT-A

complexes mediate anterograde and retrograde protein trafficking driven by the kinesin-2 and dynein-2 motors, respectively (for example, see (Ishikawa and Marshall, 2011)). Indeed, our group recently identified an interaction interface between the IFT-B complex and the anterograde kinesin-2 motor, and showed that this interaction is essential for ciliogenesis (Funabashi *et al.*, 2018). On the other hand, however, our group and others have shown that, in addition to its role in retrograde trafficking, the IFT-A complex, as well as its adaptor protein TULP3, mediates the import of ciliary GPCR (Badgandi *et al.*, 2017; Hirano *et al.*, 2017). It thus seems likely that, in addition to their roles in intraciliary trafficking, the IFT-A and IFT-B complexes participate in import and export across the ciliary gate of ciliary GPCR via their adaptors, TULP3 and the BBSome, respectively.

As retrograde trafficking and/or export of ciliary GPCRs is impaired in cells derived from *IFT25*-KO and *IFT27*-KO mice, the groups of Nachury and Pazour proposed that IFT25 and IFT27, which form a tight dimer in the IFT-B core subcomplex (see Fig. 2-3A), regulate retrograde trafficking or export of ciliary GPCR mediated by the BBSome (Eguether *et al.*, 2014; Liew *et al.*, 2014). However, my attempts to show a direct interaction of the BBSome with IFT25 and/or IFT27 (Fig. 2-2A) and an indirect interaction involving ARL6 and/or LZTFL1 (my unpublished results), as proposed by the Nachury and Pazour groups, have been unsuccessful to date. In any case, understanding the full picture of the roles of the very large IFT machinery, composed of 22 subunits (16 from IFT-B and 6 from IFT-A), and the BBSome in ciliary protein trafficking will require elucidation of the intricate roles of individual subunits in the context of protein–protein interactions.

CONCLUSIONS

The summary of the results presented in this study is as follows:

Chapter 1

1. The BBSome holocomplex can be divided into two subcomplexes, namely the linker subcomplex composed of BBS4, BBS8 and BBS18, and the core subcomplex composed of BBS1, BBS2, BBS7, and BBS9. BBS9 serves as a hub subunit that connects the linker and core subcomplexes and binds BBS5.
2. The CT regions containing the GAE and PF domains, but not the BP domains (except for that of BBS1) of the BBSome core subunits mainly participate in the assembly of the core subcomplex.
3. BBS9 reinforces interaction of BBS1 with ARL6 via its BP domain, and partially restores the ARL6-binding defect of the BBS1(I399E) and BBS1(R404A) mutants.
4. KO of BBS1 abolishes ciliary localization of the BBSome, but does not affect the normal localization of IFT88 (an IFT-B subunit) or IFT140 (an IFT-A subunit).
5. KO of BBS1 results in a severe defect in the export of GPR161 from cilia upon the activation of Hh signaling, but does not affect ciliary entry of SMO upon the activation of Hh signaling.
6. The defect in GPR161 trafficking observed in *BBS1*-KO cells can be rescued by the exogenous expression of wild-type BBS1 but not by its C-terminally truncated mutant defective in BBS9 binding.

These results show that the integrity of the BBSome architecture revealed by the VIP assay is essential for its function, and indicate that the BBSome regulates the export of ciliary GPCRs from cilia.

Chapter 2

1. The BBSome interacts with the IFT-B complex via the BBS1–BBS9 dimer and IFT38. The coiled-coil domain and the following region of IFT38 are necessary and sufficient for this interaction, and IFT38(ΔC), which lacks the region following the coiled-coil domain, fails to interact with the BBS1–BBS9 dimer.
2. *IFT38*-KO cells exhibit the no-cilia phenotype. The exogenous expression of IFT38(ΔC) as well as IFT38(WT) can rescue the ciliogenesis defect, although the cilia of IFT38(ΔC)-expressing *IFT38*-KO cells are longer than those of IFT38(WT)-expressing *IFT38*-KO cells.

3. IFT38(ΔC)-expressing *IFT38*-KO cells exhibit the normal localization of IFT88 and IFT140.
4. Although IFT38(ΔC)-expressing *IFT38*-KO cells exhibit the normal localization of the BBSome, GPR161 remains within cilia even upon the activation of Hh signaling, while SMO normally enters cilia.

These data indicate that the interaction between the IFT-B and the BBSome via IFT38 and the BBS1–BBS9 dimer is required for the BBSome-mediated export of ciliary GPCRs.

Together, the results presented in this study show that the IFT-B complex is necessary for the export of ciliary GPCRs mediated by the BBSome via the interaction of IFT38 and the BBS1–BBS9 dimer, whereas the BBSome is not required for the function of the IFT machinery.

The present study will provide not only new insight into understanding the molecular basis of ciliary GPCR trafficking by the collaboration between the BBSome and the IFT machinery, but also a typical example of how to elucidate the functional relationship between large protein complexes on the basis of interactions by using the VIP assay.

MATERIALS AND METHODS

Plasmids, antibodies, and reagents

The whole coding sequences of the BBSome subunits were amplified by PCR from human brain, kidney, or liver cDNA library. Expression vectors for the BBSome and the IFT proteins, and their deletion/point-mutated constructs used in this study are listed in Table 1. Plasmids for production of the replication-defective, self-inactivating lentiviral vector pRRLsinPPT-mCherry and packaging plasmids (pRSV-REV, pMD2.g, and pMDLg/pRRE) were kindly provided by Peter McPherson (McGill University, Montreal, Canada; Thomas *et al.*, 2009). Antibodies used in this study are listed in Table 2. SAG and Polyethylenimine Max were purchased from Enzo Life Sciences and Polysciences, respectively.

Preparation of GST–anti-GFP Nb beads

A DNA fragment encoding anti-GFP Nb, synthesized based on the sequence used by Kubala *et al.* (Kubala *et al.*, 2010), was subcloned into pGEX-6P-1 (GE Healthcare). Our group have deposited the plasmid encoding GST–anti-GFP Nb to Addgene (ID #61838). E. coli BL21(DE3) cells transformed with the GST-fused anti-GFP Nb vector were treated with 0.1 mM IPTG for 4 h at 30°C to induce protein expression, lysed, and used to purify the recombinant protein with glutathione–Sepharose 4B beads (GE Healthcare). The yield of purified GST–anti-GFP Nb was ~5 mg/L of bacterial culture. The protein concentration was adjusted to ~200 μg/mL for immunoprecipitation assays.

VIP assay and immunoblotting analysis

HEK293T cells cultured in DMEM with high glucose (Nacalai Tesque) supplemented with 5% fetal bovine serum (FBS) were plated in 6-well plates. Approximately 1.6×10^6 cells were transfected with EGFP (2 μg) and tRFP/mChe (2 μg) fusion constructs using Polyethylenimine Max (20 μg), and then cultured for 24 h. Before the assay, expression of fluorescent fusion proteins was confirmed under a fluorescence microscope. The cells were lysed in 250 μL of lysis buffer (in chapter 1, 20 mM HEPES-KOH [pH 7.4], 150 mM NaCl, 0.1% Triton X-100 and 10% glycerol; in chapter 2, 10 mM HEPES, pH 7.4, 5 mM $MgSO_4$, 1 mM DTT, 0.5 mM EDTA, 25 mM KCl, and 0.5% NP-40) containing protease inhibitor cocktail (Nacalai Tesque). After 15 min on ice, the cell lysates were centrifuged at 16,100 × g for 15 min at 4°C in a microcentrifuge. The supernatants (200 μL) were incubated with 5 μL of GST–anti-GFP

Nb pre-bound to glutathione–Sepharose 4B beads in 0.2 mL 8-Tube Strips (Greiner) for 1 h at 4 °C. The tube strips were centrifuged at 2,000 × g for 30 sec at room temperature. The precipitated beads were washed three times with 180 μL of lysis buffer, and then transferred into a 96-well plate for observation. Fluorescence on the beads was observed using an all-in-one–type fluorescence microscope (Biozero BZ-8000, Keyence) using a 20×/0.75 objective lens under fixed conditions (for green fluorescence, sensitivity ISO 400, exposure 1/30 sec; and for red fluorescence, sensitivity ISO 800, exposure 1/10 sec). Image acquisition was performed under fixed conditions. The quantitation of fluorescence intensity was performed using the ImageJ software (National Institutes of Health). Fluorescence was also measured with a microplate reader (EnVision, PerkinElmer) equipped with filter sets appropriate for detecting fluorescence. After fluorescence measurement, for immunoblotting, the materials bound to the beads were separated by SDS-PAGE and electroblotted onto an Immobilon-P transfer membrane (Millipore). The membrane was blocked in 5% skim milk and incubated sequentially with primary and horseradish peroxidase–conjugated secondary antibodies. Detection was carried out using a Chemi-Lumi One L kit (Nacalai Tesque).

For expression of combinations of EGFP, tRFP/mChe, tBFP, and iRFP fusion constructs, approximately 3.2 × 10^6 HEK293T cells grown on 6-cm dishes were transfected with the expression vectors (12 μg) using Polyethylenimine Max (60 μg), and then cultured for 24 h. Immunoprecipitation was performed as described above. Fluorescence on the beads was measured with a confocal laser-scanning microscope (A1R-MP, Nikon) equipped with four lasers (405, 488, 561, and 638 nm wavelength) and using 20×/0.75 objective lens.

For expression of combinations of up to eight of EGFP and tRFP/mChe fusion constructs, approximately 1.6 × 10^6 cells grown in 6-well plates were transfected with the expression vectors (8 μg) using Polyethylenimine Max (40 μg), and then cultured for 24 h. Immunoprecipitation was performed as described above.

Immunofluorescence analysis

hTERT-RPE1 cells were cultured in DMEM/F-12 (Nacalai Tesque) supplemented with 10% FBS and 0.348% sodium bicarbonate. To induce ciliogenesis, cells were grown on coverslips up to 100% confluence, and starved for 24 h in Opti-MEM containing 0.2% bovine serum albumin. For immunofluorescence analysis, cells were fixed and permeabilized with 100% methanol for 5 min at –20 °C, and washed three times with phosphate-buffered saline. The fixed/permeabilized cells were blocked with 10% FBS, stained with antibodies diluted in 5% FBS, and observed using

an Axiovert 200M microscope (Carl Zeiss). Statistical analyses were performed using JMP Pro 13 software (SAS Institute).

Establishment of KO cell lines using the CRISPR/Cas9 system

The strategy for KO of the *BBS1* or *IFT38* gene in hTERT-RPE1 cells (American Type Culture Collection CRL-4000) using the CRISPR/Cas9 system using homology-independent DNA repair (version 2 method) was previously described in detail (Katoh *et al.*, 2017). The single guide RNA (sgRNA) sequence targeting the human *BBS1* or *IFT38* gene (see Table 3) was designed using CRISPR design (Hsu *et al.*, 2013). Double-stranded oligonucleotides for these sequences were inserted into the knock-in donor vector pDonor-tBFP-NLS-Neo (Addgene ID 80766) and the all-in-one sgRNA expression vector, pSpCas9(BB)-2A-Puro (PX459; Addgene ID 48139). hTERT-RPE1 cells were grown on a 12-well plate to approximately 3.0×10^5 cells, and transfected with 1 μg of the sgRNA vector and 0.25 μg of the donor knock-in vector using X-tremeGENE9 DNA Transfection Reagent (Roche Applied Science). After selection in the presence of G418 (600 μg/mL), cells with nuclear tBFP signals were isolated. To confirm KO of the target gene, genomic DNA was extracted from the isolated cells and subjected to PCR using KOD FX Neo DNA polymerase (Toyobo). Three sets of primers (Table 3) were used for PCR to distinguish the following three states of integration of the donor vector: forward integration, reverse integration, and no integration with a small indel (see Fig. 1-7). Direct sequencing of the PCR products ensured the KO of both alleles of the *BBS1* or *IFT38* gene, with integration of the donor vector and/or small deletion/insertion causing a frameshift.

Preparation of cells stably expressing mChe-tagged BBS1 and IFT38 constructs

Lentiviral vectors were prepared as described previously (Takahashi *et al.*, 2012). Briefly, pRRLsinPPT-mChe-BBS1(WT) or its mutant, or pRRLsinPPT-mChe-IFT38(WT) or its ΔC mutant was transfected into HEK293T cells using Polyethylenimine Max along with the packaging plasmids (pRSV-REV, pMD2.g, and pMDL/pRRE). Culture medium was replaced 8 h after transfection, and collected at 24, 36, and 48 h after transfection. The culture medium containing viral particles was passed through a 0.45-μm filter and centrifuged at 32,000 × g at 4 °C for 4 h. Precipitated lentiviral particles were resuspended in Opti-MEM (Invitrogen) and stored at −80 °C until use. *BBS1*-KO cells that express mChe-BBS1(WT) or its mutant, or *IFT38*-KO cells that express mCh-IFT38(WT) or its ΔC mutant were prepared by adding a lentiviral suspension to the culture medium.

Table 1. Plasmid vectors used in this study

No.	Vector	Insert	Reference
1	pcDNA3-EGFP-C	Human BBS1	This study
2	pEGFP-C1	Human BBS2	This study
3	pEGFP-C1	Human BBS4	This study
4	pEGFP-C1	Human BBS5	This study
5	pEGFP-C1	Human BBS7	This study
6	pEGFP-C1	Human BBS8	This study
7	pEGFP-C1	Human BBS9	This study
8	pEGFP-C1	Human BBS18	This study
9	pcDNA3-EGFP-C	Human ARL6 (Q73L, ΔN: 17-186)	This study
10	pTagRFP-T-C	Human BBS1	This study
11	pTagRFP-T-C	Human BBS2	This study
12	pTagRFP-T-C	Human BBS4	This study
13	pTagRFP-T-C	Human BBS5	This study
14	pTagRFP-T-C	Human BBS7	This study
15	pTagRFP-T-C	Human BBS8	This study
16	pTagRFP-T-C	Human BBS9	This study
17	pTagRFP-T-C	Human BBS18	This study
18	pTagRFP-T-C	Human ARL6 (Q73L, ΔN: 17-186)	This study
19	pTagBFP2-C	Human BBS1	This study
20	pTagBFP2-C	Human BBS7	This study
21	pTagBFP2-C	Human BBS8	This study
22	pTagBFP2-C	Human BBS18	This study
23	pcDNA3-iRFP-C	Human BBS8	This study
24	pcDNA3-iRFP-C	Human BBS9	This study
25	pcDNA3-EGFP-C	Human BBS1(BP, 1-430)	This study
26	pcDNA3-EGFP-C	Human BBS1(CT, 431-593)	This study
27	pEGFP-C1	Human BBS1(I399E)	This study
28	pEGFP-C1	Human BBS1(R404A)	This study
29	pEGFP-C1	Human BBS1(da, 1-430, 483-593)	This study
30	pEGFP-C1	Human BBS1(1-575)	This study
31	pTagRFP-T-C	Human BBS1(BP, 1-430)	This study
32	pTagRFP-T-C	Human BBS1(CT, 431-593)	This study

33	pTagRFP-T-C	Human BBS1(I399E)	This study
34	pTagRFP-T-C	Human BBS1(R404A)	This study
35	pTagRFP-T-C	Human BBS1(da, 1-430, 483-593)	This study
36	pTagRFP-T-C	Human BBS1(1-575)	This study
37	pRRLsinPPT-mCherry-C	Human BBS1	This study
38	pRRLsinPPT-mCherry-C	Human BBS1(I399E)	This study
39	pRRLsinPPT-mCherry-C	Human BBS1(R404A)	This study
40	pRRLsinPPT-mCherry-C	Human BBS1(1-575)	This study
41	pRRLsinPPT-mCherry-C	Human BBS1	This study
42	pRRLsinPPT-mCherry-C	Human BBS1(I399E)	This study
43	pRRLsinPPT-mCherry-C	Human BBS1(R404A)	This study
44	pRRLsinPPT-mCherry-C	Human BBS1(1-575)	This study
45	pEGFP-C1	Human BBS2(BP, 1-330)	This study
46	pEGFP-C1	Human BBS2(CT, 331-721)	This study
47	pTagRFP-T-C	Human BBS2(BP, 1-330)	This study
48	pTagRFP-T-C	Human BBS2(CT, 331-721)	This study
49	pTagBFP2-C	Human BBS2	This study
50	pTagBFP2-C	Human BBS4	This study
51	pTagBFP2-C	Human BBS5	This study
52	pmCherry-C1	Human BBS7	This study
53	pmCherry-C1	Human BBS7(BP, 1-322)	This study
54	pmCherry-C1	Human BBS7(CT, 323-715)	This study
55	pEGFP-C1	Human BBS9(BP, 1-378)	This study
56	pEGFP-C1	Human BBS9(CT, 379-887)	This study
57	pTagRFP-T-C	Human BBS9(BP, 1-378)	This study
58	pTagRFP-T-C	Human BBS9(CT, 379-887)	This study
59	pEGFP-C1	Mouse IFT38	Katoh *et al.* (2016)
60	pEGFP-C1	Mouse IFT38(ΔC: 1-328)	Katoh *et al.* (2016)
61	pEGFP-C1	Mouse IFT38(ΔN: 120-413)	Katoh *et al.* (2016)
62	pEGFP-C1	Mouse IFT38(NN-CH: 1-119)	Katoh *et al.* (2016)
63	pEGFP-C1	Mouse IFT38(CC: 120-328)	Katoh *et al.* (2016)
64	pEGFP-C1	Mouse IFT38(CT: 329-413)	Katoh *et al.* (2016)
65	pCAG-mCherry-C	Human BBS1	This study
66	pCAG-mCherry-C	Human BBS2	This study
67	pCAG-mCherry-C	Human BBS9	This study

68	pEGFP-N1	Human IFT20	Katoh *et al.* (2016)
69	pEGFP-C1	Human IFT22	Katoh *et al.* (2016)
70	pEGFP-C1	Human IFT25	Katoh *et al.* (2016)
71	pEGFP-C1	Human IFT27	Katoh *et al.* (2016)
72	pCAG-EGFP-C	Human IFT46	Katoh *et al.* (2016)
73	pCAG-EGFP-C	Human IFT52	Katoh *et al.* (2016)
74	pEGFP-C1	Human IFT54	Katoh *et al.* (2016)
75	pCAG-EGFP-C	Human IFT56	Katoh *et al.* (2016)
76	pEGFP-C1	Human IFT57	Katoh *et al.* (2016)
77	pCAG-EGFP-C	Human IFT70B	Katoh *et al.* (2016)
78	pCAG-EGFP-C	Human IFT74	Katoh *et al.* (2016)
79	pCAG-EGFP-C	Human IFT80	Katoh *et al.* (2016)
80	pCAG-EGFP-C	Human IFT81	Katoh *et al.* (2016)
81	pCAG-EGFP-C	Human IFT88	Katoh *et al.* (2016)
82	pCAG-EGFP-C	Human IFT172	Katoh *et al.* (2016)
83	pEGFP-C1	IFT43	Hirano *et al.* (2017)
84	pCAG2-EGFP-C	IFT121	Hirano *et al.* (2017)
85	pCAG2-EGFP-C	IFT122	Hirano *et al.* (2017)
86	pCAG2-EGFP-C	IFT139	Hirano *et al.* (2017)
87	pCAG2-EGFP-C	IFT140	Hirano *et al.* (2017)
88	pCAG2-EGFP-C	IFT144	Hirano *et al.* (2017)
89	pEGFP-C1	TULP3	Hirano *et al.* (2017)
90	pTagRFP-T-N	Human IFT20	Katoh *et al.* (2016)
91	pCAG-mCherry-N	Human IFT80	Katoh *et al.* (2016)
92	pCAG-mCherry-C	Human IFT54	Katoh *et al.* (2016)
93	pCAG2-mCherry-C	Human IFT57	This study
94	pCAG-mCherry-C	Human IFT88	Katoh *et al.* (2016)
95	pRRLsinPPT-mCherry-C	Mouse IFT38	This study
96	pRRLsinPPT-mCherry-C	Mouse IFT38(ΔC: 1-328)	This study

Table 2. Antibodies used in this study

Anrtibodies	Manufactures	Clones or catalog numbers	Dilution (purpose)
Monoclonal mouse anti-Ac-a-Tubulin	Sigma-Aldrich	6-11B-1	1:1,000 (immunofluorescense)
Monoclonal mouse anti-g-Tubulin	Sigma-Aldrich	GTU-88	1:1,000 (immunofluorescense)
Polyclonal rabbit anti-ARL13B	Proteintech	17711-1-AP	1:1,000 (immunofluorescense)
Polyclonal rabbit anti-IFT88	Proteintech	13967-1-AP	1:1,000 (immunofluorescense)
Polyclonal rabbit anti-IFT140	Proteintech	17460-1-AP	1:500 (immunofluorescense)
Polyclonal rabbit anti-BBS5	Proteintech	14569-1-AP	1:500 (immunofluorescence)
Polyclonal rabbit anti-BBS9	Atlas antibodies	HPA021289	1:1,000 (immunofluorescense)
Polyclonal rabbit anti-ARL6	Proteintech	12676-1-AP	1:500 (immunofluorescense)
Polyclonal rabbit anti-SMO	Abcam	ab38686	1:500 (immunofluorescense)
Polyclonal rabbit anti-GPR161	Proteintech	13398-1-AP	1:200 (immunofluorescense)
Monoclonal mouse anti-FGFR1OP	abnova	2B1	1:10,000 (immunofluorescencse)
Monoclonal mouse anti-RFP	MBL Life Science	3G5	1:1,000 (immunofluorescense)
Polyclonal rabbit anti-RFP	MBL Life Science	PM005	1:1,000 (immunoblotting)
Polyclonal rabbit anti-TagRFP	Evrogen	AB233	1:1,000 (immunoblotting)
Monoclonal mouse anti-GFP	BD Biosciences	JL-8	1:1,000 (immunoblotting)
AlexaFluor-conjugated secondary	Molecular Probes	A11034, A21240, A21131 A21147	1:500 (immunofluorescence)
AlexaFluor-conjugated secondary	Molecular Probes	A21429, A21242	1:1,000 (immunofluorescence)
DyLight 649-conjugated secondary	Jackson ImmunoResearch	115-495-209	1:500 (immunofluorescense)
Peroxidase-conjugated secondary	Jackson ImmunoResearch	115-035-166, 111-035-144	1:3,000 (immunoblotting)

Table 3. Oligo DNAs used in this study

No.	Names	Sequences
1	pTagBFP-N-RV2	5'-CGTAGAGGAAGCTAGTAGCCAGG-3'
2	BBS1-genome#1-FW	5'-GACAGGAGGAGTTCTTTTTGCTGC-3'
3	BBS1-genome#1-RV	5'-AACCACTTCGAATTGGCCTCATTG-3'
4	BBS1-gRNA#1-S	5'-CACCGCAGGCGTCGGAATCCGATG-3'
5	BBS1-gRNA#1-AS	5'-AAACCATCGGATTCCGACGCCTGC-3'
6	BBS1-genome#2-FW	5'-CTCGGGCACTATTGGGCGTTAC-3'
7	BBS1-genome#2-RV	5'-AGGCTTTGTCTTAGTAGAATCCCCA-3'
8	BBS1-gRNA#2-S	5'-CACCGCAATGAGGCCAATTCGAAG-3'
9	BBS1-gRNA#2-AS	5'-AAACCTTCGAATTGGCCTCATTGC-3'
10	IFT38-Genome-#1-S	5'-TGAATGTCATCCTACGGATTCCCC-3'
11	IFT38-Genome-#1-AS	5'-AACTATGAGTGTGTACCACCCAGG-3'
12	IFT38-gRNA#1-S	5'-AATATGTCGAGGGTATCCCA-3'
13	IFT38-gRNA#1-AS	5'-TGGGATACCCTCGACATATT-3'
14	IFT38-Genome-#2-S	5'-CTAATCGGCCCTAGCACTGATCTC-3'
15	IFT38-Genome-#2-AS	5'-CCACAGAAACCCAGCAATGGAATG-3'
16	IFT38-gRNA#2-S	5'-TCAGGCGGGATGTCAGTCTG-3'
17	IFT38-gRNA#2-AS	5'-CAGACTGACATCCCGCCTGA-3'

ACKNOWLEDGEMENTS

I would like to express the deepest appreciation to Professor Kazuhisa Nakayama, Graduate School of Pharmaceutical Sciences, Kyoto University, and Assistant Professor Yohei Katoh, Graduate School of Pharmaceutical Sciences, Kyoto University, for their superior guidance and suggestions through the course of this work.

I am deeply grateful to Mr. David Hartanto, Ms. Rie Miyano, and Mr. Takuya Kobayashi for technical supports and helpful discussions.

I would like to express my gratitude to Dr. Hye-Won Shin, Dr. Hiroyuki Takatsu, Dr. Senye Takahashi, Dr. Yuki Imoto, Dr. Tomoki Naito, Dr. Teruki Funabashi, Mr. Shohei Hirose, Mr. Yohei Hagiya, Ms. Minako Kobayashi, Ms. Rie Miyano, Ms. Chikako Yagi, Mr. Gaku Tanaka, Mr. Yoshiki Tanaka, Mr. Takashi Matsumoto, Mr. Masaya Terada, Mr. Tomoaki Hirano, Mr. Yuya Nishijima, Ms. Mariko Takahara, Mr. Naoto Takada, Mr. Yuki Hamada, Mr. Ryota Takei, Ms. Saki Michisaka, Ms. Luxiaoxue Liang, Mr. Takuya Tone, Mr. Yuta Tsurumi, Ms. Maho Sugawa, Ms. Misato Okazaki, Mr. Kentaro Nakamura, Mr. Tatsuro Noguchi, and Ms. Sayaka Fujisawa for their technical advice and helpful discussions.

My heartfelt appreciation also goes to the former and present members of the Department of Physiological Chemistry, Graduate School of Pharmaceutical Sciences, Kyoto University, for their continuous encouragements, helpful discussions, and technical supports.

I was supported by Grant-in-Aid for JSPS research fellow.

Finally, I would like to thank my family, Tsuguo, Masako, Rika, and Yusuke, for their persistent understanding, continuous encouragements, and support for many things.

REFERENCES

Badgandi, H. B., Hwang, S., Shimada, I. S., Loriot, E. and Mukhopadhyay, S. (2017). Tubby family proteins are adaptors for ciliary trafficking of integral membrane proteins. J. Cell Biol. 216, 743-760.

Botilde, Y., Yoshiba, S., Shinohara, K., Hasegawa, T., Nishimura, H., Shiratori, H. and Hamada, H. (2013). Cluap1 localizes preferentially to the base and tip of cilia and is required for ciliogenesis in mouse embryo. Dev. Biol. 381, 203-212.

Braun, D. A. and Hildebrandt, F. (2017). Ciliopathies. Cold Spring Harb. Perspect. Biol. 9, a028191

Briscoe, J. and Thérond, P. P. (2013). The mechanisms of Hedgehog signalling and its roles in development and disease. Nat. Rev. Mol. Cell Biol. 14, 416-429.

Eguether, T., San Agustin, J.T., Keady, B.T., Jonassen, J.A., Liang, Y., Francis, R., Tobita, K., Johnson, C.A., Abdelhamed, Z.A., Lo, C.W., and Pazour, G.J. (2014). IFT27 links the BBSome to IFT for maintenance of the ciliary signaling compartment. Dev. Cell 21, 279-290.

Funabashi, T., Katoh, Y., Michisaka, S., Terada, M., Sugawa, M. and Nakayama, K. (2017). Ciliary entry of KIF17 is dependent on its binding to the IFT-B complex via IFT46-IFT56 as well as on its nuclear localization signal. Mol. Biol. Cell 28, 624-633.

Funabashi, T., Katoh, Y., Okazaki, M., Sugawa, M. and Nakayama, K. (2018). Interaction of heterotrimeric kinesin-II with IFT-B-connecting tetramer is crucial for ciliogenesis. J. Cell Biol. 217, 2867-2876.

Hamada, Y., Tsurumi, Y., Nozaki, S., Katoh, Y. and Nakayama, K. (2018). Interaction of WDR60 intermediate chain with TCTEX1D2 light chain of the dynein-2 complex is crucial for ciliary protein trafficking. Mol. Biol. Cell 29, 1628-1639.

Hirano, T., Katoh, Y., and Nakayama, K. (2017). Intraflagellar transport-A complex mediates ciliary entry as well as retrograde trafficking of ciliary G protein-coupled receptors. Mol. Biol. Cell. 28, 429-439.

Hsu, P. D., Scott, D. A., Weinstein, J. A., Ran, F. A., Konermann, S., Agarwala, V., Li, Y., Fine, E. J., Wu, X., Shalem, O., Cradick, T.J., Marraffini, L.A., Bao, G., and Zhang, F. (2013). DNA targeting specificity of RNA-guided Cas9 nucleases. Nat. Biotechnol. 31, 827-832.

Ishikawa, H., and Marshall, W.F. (2011). Ciliogenesis: building the cell's antenna. Nat. Rev. Mol. Cell Biol. 12, 222-234.

Jackson, L.P., Lewis, M., Kent, H.M., Edeling, M.A., Evans, P.R., Duden, R., Owen, D.J. (2012). Molecular basis for recognition of dilysine trafficking motifs by COPI. Dev Cell 23, 1255-1262.

Jin, H., White, S. R., Shida, T., Schulz, S., Aguilar, M., Gygi, S. P., Bazan, J. F., and Nachury, M. V. (2010). The conserved Bardet-Biedl syndrome proteins assemble a coat that traffics membrane proteins to cilia. Cell 141, 1208-1219.

Katoh, Y., Michisaka, S., Nozaki, S., Funabashi, T., Hirano, T., Takei, R. and Nakayama, K. (2017). Practical method for targeted disruption of cilia-related genes by using CRISPR/Cas9-mediated homology-independent knock-in system. Mol. Biol. Cell 28, 898-906.

Katoh, Y., Nakamura, K. and Nakayama, K. (2018). Visible immunoprecipitation (VIP) assay: a simple and versatile method for visual detection of protein-protein interactions. Bio-protocol 8, e2687.

Katoh, Y., Terada, M., Nishijima, Y., Takei, R., Nozaki, S., Hamada, H. and Nakayama, K. (2016). Overall architecture of the intraflagellar transport (IFT)-B complex containing Cluap1/IFT38 as an essential component of the IFT-B peripheral subcomplex. J. Biol. Chem. 291, 10962-10975.

Klink, B.U., Zent, E., Juneja, P., Kuhlee, A., Raunser, S., and Wittinghofer, A. (2017). A recombinant BBSome core complex and how it interacts with ciliary cargo. eLife 6, e27434.

Knockenhauer, K.E. and Schwartz, T.U. (2015). Structural characterization of Bardet-Biedl syndrome 9 protein (BBS9). J. Biol. Chem. 290, 19569-19583.

Kubala, M. H., Kovtun, O., Alexandrov, K. and Collins, B. M. (2010). Structural and thermodynamic analysis of the GFP:GFP-nanobody complex. Protein Sci. 19, 2389-2401.

Lechtreck, K.-F., Johnson, E. C., Sakai, T., Cochran, D., Ballif, B. A., Rush, J., Pazour, G. J., Ikebe, M. and Witman, G. B. (2009). The Chlamydomonas reinhardtii BBSome is an IFT cargo required for export of specific signaling proteins from flagella. J. Cell Biol. 187, 1117-1132.

Liew, G. M., Ye, F., Nager, A. R., Murphy, J. P., Lee, J. S. H., Aguiar, M., Breslow, D. K., Gygi, S. P., and Nachury, M. V. (2014). The intraflagellar transport protein IFT27 promotes BBSome exit from cilia through the GTPase ARL6/BBS3. Dev. Cell 31, 265-278.

Loktev, A. V., Zhang, Q., Beck, J. S., Searby, C. C., Scheetz, T. E., Bazan, J. F., Slusarski, D. C., Sheffield, V. C., Jackson, P. K. and Nachury, M. V. (2008). A BBSome subunit links ciliogenesis, microtubule stability, and acetylation. Dev.

Cell 15, 854-865.

Ma W. and Goldberg J. (2013). Rules for the recognition of dilysine retrieval motifs by coatomer. EMBO J. 32, 926-937

Madhivanan, K. and Aguilar, R. C. (2014). Ciliopathies: the trafficking connection. Traffic 15, 1031-1056.

Mourão, A., Nager AR, Nachury, M.V., Lorentzen, E. (2014). Structural basis for membrane targeting of the BBSome by ARL6. Nat. Struct. Mol. Biol. 21, 1035-1041.

Mukhopadhyay, S. and Rohatgi, R. (2014). G-protein-coupled receptors, Hedgehog signaling and primary cilia. Sem. Cell Dev. Biol. 33, 63-72.

Nachury, M. V., Loktev, A. V., Zhang, Q., Westlake, C. J., Peränen, J., Merdes, A., Slusarski, D. C., Scheller, R. H., Bazan, J. F., Sheffield, V. C., and Jacson, P. K. (2007). A core complex of BBS proteins cooperates with the GTPase Rab8 to promote ciliary membrane biogenesis. Cell 129, 1201-1213.

Nakayama, K. and Wakatsuki, S. (2003). The structure and function of GGAs, the traffic controllers at the TGN sorting crossroads. Cell. Struct. Funct. 28, 431-442

Nakayama, K., and Katoh, Y. (2018). Ciliary protein trafficking mediated by IFT and BBSome complexes with the aid of kinesin-2 and dynein-2 motors. J. Biochem. 163, 155-164

Rosenbaum, J.L., and Witman, G.B. (2002). Intraflagellar transport. Nat. Rev. Mol. Cell Biol. 3, 813-825

Saerens, D., Pellis, M., Loris, R., Pardon, E., Dumoulin, M., Matagne, A., Wyns, L., Muyldermans, S. and Conrath, K. (2005). Identification of universal VHH framework to graft non-canonical antigen-binding loops of camel single-domain antibodies. J. Mol. Biol. 352, 597-607.

Seo, S., Baye, L. M., Schulz, N. P., Beck, J. S., Zhang, Q., Slusarski, D. C. and Sheffield, V. C. (2010). BBS6, BBS10, and BBS12 form a complex with CCT/TRiC family chaperonins and mediate BBSome assembly. Proc. Natl. Acad. Sci. USA 107, 1488-1493.

Seo, S., Zhang, Q., Bugge, K., Breslow, D.K., Searby, C.C., Nachury, M.V., and Sheffield, V.C. (2011). A novel protein LZTFL1 regulates ciliary trafficking of the BBSome and Smoothened. PLoS Genet. 7, e1002358

Shida, T., Cueva, J.G., Xu, Z., Goodman, M.B., and Nachury, M.V. (2010). The major α-tubulin K40 acetyltransferase αTAT1 promotes rapid ciliogenesis and efficient mechanosensation. Proc. Natl. Acad. Sci. USA 107, 21517-21522.

Sung, C.-H. and Leroux, M. R. (2013). The roles of evolutionarily conserved functional modules in cilia-related trafficking. Nat. Cell Biol. 15, 1387-1397.

Takahara, M., Katoh, Y., Nakamura, K., Hirano, T., Sugawa, M., Tsurumi, Y. and Nakayama, K. (2018). Ciliopathy-associated mutations of IFT122 impair ciliary protein trafficking but not ciliogenesis. Hum. Mol. Genet. 27, 516-528.

Takahashi, S., Kubo, K., Waguri, S., Yabashi, A., Shin, H.-W., Katoh, Y. and Nakayama, K. (2012). Rab11 regulates exocytosis of recycling vesicles at the plasma membrane. J. Cell Sci. 125, 4049-4057.

Taschner, M., and Lorentzen, E. (2016) The intraflagellar transport machinery. Cold Spring Harb. Perspect. Biol. 8, a028092.

Thomas, S., Ritter, B., Verbich, D., Sanson, C., Bourbonnière, L., McKinney, R. A. and McPherson, P. S. (2009). Intersectin regulates dendritic spine development and somatodendritic endocytosis but not synaptic vesicle recycling in hippocampal neurons. J. Biol. Chem. 284, 12410-12419.

Verhey, K.J., and Yang, W. (2016). Permeability barriers for generating a unique ciliary protein and lipid composition. Curr. Opin. Cell Biol. 41, 109-116.

Wei, Q., Ling, K. and Hu, J. (2015). The essential roles of transition fibers in the context of cilia. Curr. Opin. Cell Biol. 35, 98-105.

Wei, Q., Zhang, Y., Li, Y., Zhang, Q., Ling, K. and Hu, J. (2012). The BBSome controls IFT assembly and turnaround in cilia. Nat. Cell Biol. 14, 950-957.

Williams, C.L., McIntyre, J.C., Norris, S.R., Jenkins, P.M., Zhang, L., Pei, Q., Verhey, K., and Martens, J.R. (2014). Direct evidence for BBSome-associated intraflagellar transport reveals distinct properties of native mammalian cilia. Nat. Commun. 5, 5813.

Woodsmith, J., Apelt, L., Casado-Medrano, V., Özkan, Z., Timmermann, B., and Stelzl, U. (2017). Protein interaction perturbation profiling at amino-acid resolution. Nat. Methods. 14, 1213.

Ye, F., Nager, A. R. and Nachury, M. V. (2018). BBSome trains remove activated GPCRs from cilia by enabling passage through the transition zone. J. Cell Biol. 217, 1847-1868.

Zhang, Q., Nishimura, D., Seo, S., Vogel, T., Morgan, D. A., Searby, C., Bugge, K., Stone, E. M., Rahmouni, K., and Sheffield, V. C. (2011). Bardet-Biedl syndrome 3 (Bbs3) knockout mouse model reveals common BBS-associated phenotypes and Bbs3 unique phenotypes. Proc. Natl. Acad. Sci. USA 108, 20678-20683